Optical Characterization of Thermal Transport from the Nanoscale to the Macroscale

by

Aaron Jerome Schmidt

Submitted to the Department of Mechanical Engineering
in partial fulfillment of the requirements for the degree of

Doctor of Philosophy in Mechanical Engineering

at the

MASSACHUSETTS INSTITUTE OF TECHNOLOGY
[June 2008]
May 2008

Author .....
Department of Mechanical Engineering
May 21, 2008

Certified by .....
Gang Chen
Warren and Towneley Rohsenow Professor
Thesis Supervisor

Accepted by .....
Lallit Anand
Chairman, Department Committee on Graduate Students

Optical Characterization of Thermal Transport from the Nanoscale to the Macroscale

by

Aaron Jerome Schmidt

Submitted to the Department of Mechanical Engineeringon May 21, 2008,
in partial fulfillment of the requirements for the degree of
Doctor of Philosophy in Mechanical Engineering

Abstract

The thermal properties of thin films and material interfaces play an important role in many technologies such as microelectronics and solid-state energy conversion. This thesis examines the characterization of thermal transport over length scales from nanometers upward in solids and liquids using pump-probe optical techniques. The design and implementation of a system that is uniquely suited to thermal measurements is described in detail, and the theory for interpreting the measurement results is developed using a linear systems approach, accounting for pulse accumulation effects and anisotropic thermal properties.

Cross-plane thin film and bulk thermal conductivity measurements spanning more than two orders of magnitude are presented, along with a discussion on the importance of sample preparation on thermal boundary conductance and thermal conductivity measurements. An approach for measurement of in-plane thermal properties of anisotropic thin films is presented, and as a demonstration the method is used to extract both the cross-plane and in-plane thermal conductivity of highly ordered pyrolytic graphite. In addition, the measurement techniques are extended to liquids, providing a way to measure liquid volumes less than 500 nm thick as well as solid-liquid thermal interface conductances.

Finally, optical techniques for the study of nanofluids are discussed. Transmission pump-probe measurements on gold nanorods in suspension are presented. The heat transfer dynamics of the rods are measured, and the critical role played by surfactants in the thermal transport between the rod and the surrounding fluid is studied systematically. An optical transient grating technique is used to explore the bulk thermal and viscous properties of nanofluids. Thermal conductivity measurements show that the observed thermal conductivity enhancement of nanofluids is repeatable and is not a function of the measurement technique, while acoustic attenuation measurements indicate that the nanoparticles do not form clusters in solution.

Thesis Supervisor: Gang Chen
Title: Warren and Towneley Rohsenow Professor

Acknowledgments

Many thanks are in order. First on the list is my advisor and mentor, Prof. Gang Chen. His knowledge and drive are inspirational, as is his dedication to his students. Gang displayed patience and understanding during my first three years of Ph.D. research, a time in which I struggled with experimental challenges and produced no significant results. He also pushed me to achieve more than I realized I was capable of, and I am a better person and researcher for it. I am also grateful to the other members of my thesis committee, Prof. John H. Lienhard V and Prof. Keith A. Nelson, for their encouragement and guidance, and to the many inspirational teachers I have had at MIT over the past ten years, especially Prof. Neville Hogan, Prof. John Brisson and Prof. Bora Mikić.

It has been a privilege to work with everyone in the Nanoengineering Group, whose members past and present have been a source of lasting friendships and scientific inspiration. I owe special thanks to Ronggui Yang, Arvind Narayanaswamy, and especially Chris Dames, now all professors pursuing their own research, for mentoring me as a new graduate student, and to Xiaoyuan Chen, who gave me a crash-course in optics and helped me set up early versions of our system. I feel a strong connection with Lu Hu and Tom Harris, who joined the group with me and have been great friends through the years, and with Shin Nakamura, for welcoming me into his family and opening my eyes to a new culture. Finally, I would like to thank Matteo Chiesa. His infectious enthusiasm has made working with him a true pleasure, and his presence has had a positive influence on our entire group.

I have benefitted enormously from collaboration with colleagues in several other research groups. I owe a great debt to Prof. David Cahill and Xuan Zheng at the University of Illinois at Urbana-Champaign for sharing with me key details on how to build a pump-probe system; without their patient help, much of the work in this thesis would not have been possible. It has been a pleasure and a great learning experience to work in the laboratory of Prof. Keith A. Nelson with Darius Torchinsky, Jeremy Johnson and Christoph Klieber, and to study gold nanorods with Josh Alper of the

Hamad-Schifferli Group. I would also like to thank Prof. Sarit Das, who has been generous with his time and instrumental in shaping the final chapter of this thesis.

I am grateful to the National Science Foundation, the Department of Defense, and the MIT-Ford Alliance for their generous financial support.

Finally, I am grateful to Sheena, for helping me grow as a person, and to my parents, who belong in a category by themselves for their unconditional love and support in everything I've done.

Contents

List of Figures

List of Tables

Chapter 1

Introduction and Background

As science has advanced, the boundaries of our experiments and our applied technologies have expanded to encompass increasingly extreme situations. Measurement of physical properties in these situations is challenging and often requires new or improved experimental techniques. Nowhere has this been more true than in the loosely defined field of nanotechnology, where the properties of systems with a characteristic size on the order of nanometers are studied and exploited. As the dimensions of a system shrink, the surface-to-volume ratio increases in inverse proportion with the characteristic length scale, and the role of material interfaces becomes increasingly important. The mechanical, electrical and thermal characteristics of the system may all deviate from their bulk counterparts [1], requiring new models to describe their behavior. Evaluating and using these models requires measurement of physical properties at the nanoscale, and in many cases properties as we understand them in bulk may not even be properly defined.

Nanoscale thermal properties in particular play an important role in a number of important technologies [1, 2]. An obvious example is the field of microelectronics. Commercial integrated circuits are currently available with transistors that have a lateral feature dimension of around 45 nm and contain material films less than 2 nm, or only a few atomic layers, thick. At the same time, operating frequencies have been pushed to tens of gigahertz, leading to energy carrier transit times of much less than 1 ns. Chip performance is often limited by localized heat generation, which results in

temperatures that prevent the reliable operation of the integrated circuits [3]. Heat generation similarly limits the performance of semiconductor lasers [4]. Understanding and improving integrated circuits requires a detailed understanding of the energy transport process at the device level [5]. Under these extreme conditions, macroscopic heat transfer laws may not apply, and the measurement of temperature, thermal conductivity, and the thermal conductance between material layers is a challenging issue.

Another example is thermoelectric energy conversion – the direct conversion of thermal energy into electrical energy and vice versa. The basis for thermoelectric phenomena is the fact that electrons carry heat as well as charge. Therefore, electron movement can be driven not only by an electrical potential, but also by a thermal potential. The performance of a thermoelectric device is governed by the figure of merit $ZT = S^2\sigma T/k$, where S, σ, T, and k are, respectively, the Seebeck coefficient, electrical conductivity, temperature, and thermal conductivity [6]. Performance is improved when thermal conductivity is reduced while the other terms in the figure of merit are maintained. Nano-structured materials can have a much lower thermal conductivity than predicted by diffusion heat conduction theory, primarily due to a reduction in lattice thermal conductivity caused by material interfaces [7]. As a result, nano-structured materials have exhibited improved thermoelectric performance [8, 9]. Detailed understanding of heat conduction at this scale, especially across material interfaces, is essential to continued progress in the field.

These are just two examples where detailed knowledge of thermal transport is vital. Others include the interaction between hot electrons and a crystal lattice [10], the behavior of nanoparticles suspended in a fluid [11], and the properties of nanostructures such as membranes, tubes and wires [12]. This thesis is concerned with the measurement of thermal properties, including the thermal properties of thin films, material interfaces, liquids, and nanoparticles, using pulsed lasers.

1.1 Optical Techniques for Thermal Measurement

As laser technology has advanced, laser pulses that can be achieved in the laboratory have shortened from nanoseconds to ultrashort pulses lasting tens of femtoseconds (10^{-15} s). New measurement techniques have been quickly designed around each advance in laser technology, allowing scientist to probe physical processes over ever shorter time and length scales. Short pulses allow for the interrogation of physical systems with fine temporal resolution, and this translates into correspondingly fine spatial resolution. For example, if we use a laser pulse 200 fs long to excite a system and a similar pulse to probe its state 10 ps later, the energy carriers only have time to travel a few nanometers; consequently we are only measuring the properties of those few nanometers.

The most common way such measurements are done is known as the pump-probe technique, a two step measurement. In the first step, a pulse of light (the "pump" pulse) impinges on a sample, depositing energy over a short period of time. The deposited energy causes a change in the sample which can be correlated with a change in its optical properties (reflectivity, absorptivity or transmissivity). In the second step, the "probe" pulse (or a continuous beam) arrives and probes the state of the sample. A difference in optical path lengths between the two pulses results in a variable time delay that can be used to study the evolution of a physical process. When reflectance is measured, the method is often called transient thermoreflectance (TTR), while if absorption is measured, the term transient absorption (TA) is used. Translation stages with micron-scale resolution are commonly available, which translates to time delays of tens of femtoseconds or less. Thus, laser pulse duration is the factor that limits the temporal resolution of the pump-probe method. The basic technique is illustrated in Fig. 1-1.

The high temporal resolution of the pump-probe technique makes it uniquely suited to the study of a wide range of transport processes occurring on time scales from femtoseconds to nanoseconds and longer. Paddock and Eesley were the first to apply the technique to thermal transport [13, 14]. Their work was subsequently

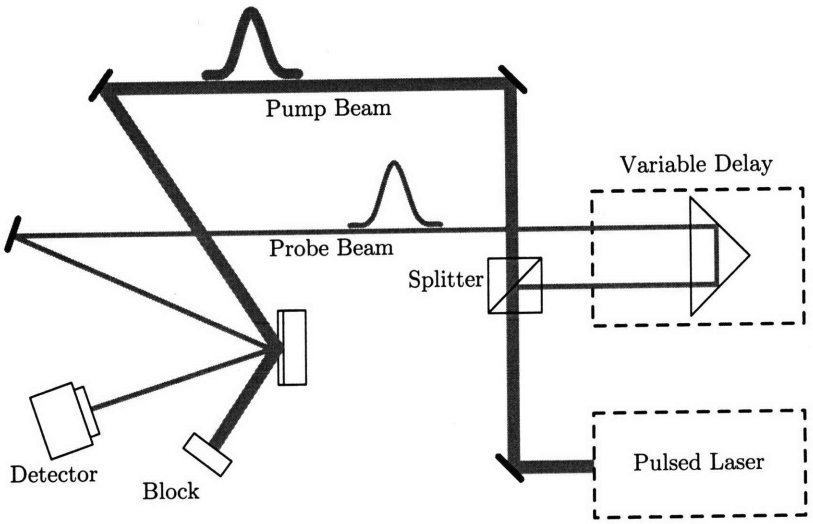

Figure 1-1: Basic principle of the pump-probe technique.

extended by Maris and coworkers [15–17] and later Norris and coworkers [18] and Cahill and coworkers [19–23]. In addition to thermal transport, variations of the pump-probe technique have been applied to the study of electron-phonon coupling in metals [10, 18, 24], electron diffusion [25], and coherent acoustic waves in solids and liquids [26–28].

In this thesis, we are primarily concerned with the measurement of thermal properties in the diffusion regime. In the next section, we provide a brief overview of the mechanisms of heat transport in a solid following excitation by an intense, ultrashort pulse of light, eventually leading to a description of the conditions which must be met for the diffusion picture of transport, which is the main approach used in all subsequent chapters, to be valid.

1.2 Transport Following Pulsed Laser Heating

1.2.1 Optical Absorption and Carrier Non-equilibrium

The majority of this thesis deals with samples which have been coated with a thin layer of metal, typically 70–100 nm thick. As we will see later, the metal layer serves two purposes: it converts the photons in the laser pulse into thermal energy over a small

distance, and it acts as temperature transducer due to the temperature dependence of its reflectivity. For these reasons, we focus here on the energy absorption and redistribution in thin metal films.

The response of a metal to an intense, ultrashort pulse of light is a complex event involving physics that span transport regimes from femtoseconds to microseconds and longer. At longer times, the classical diffusion model developed by Joseph Fourier [29] captures the transport behavior, but at shorter times a more detailed picture of the individual heat carriers is needed.

An illustration of the absorption process is shown in Fig. 1-2. Photons are absorbed over the duration of the laser pulse by a subset of free electrons in the metal. Although the details vary depending on the electronic structure of the particular metal, generally two processes occur simultaneously: ballistic electron transport through the film, and electron-electron collisions between the excited electrons and those near the Fermi level [30–32]. Assuming electron velocities close to the Fermi velocity ($\sim 10^6$ m/s [32]), ballistic electrons will traverse a 100 nm thick film in 100 fs. Electron mean free paths in common metals are on the order of 50–100 nm [33], so the hot electrons will be uniformly distributed through a thin metal film within 100–200 fs, and within 500 fs the electron population can be described by a well-defined electron temperature [30–32].

Due to the relatively small electronic heat capacity, the electron temperature can be 2–3 orders of magnitude higher than that of the lattice, possibly reaching several thousand degrees Kelvin above the equilibrium melting point. The hot electrons interact with the cold lattice through scattering events. From a quantum mechanics perspective, the lattice vibrations can be viewed as particles, discrete packets of vibrational energy known as phonons which obey boson statistics [33]. Transport can be modeled by two coupled diffusion equations, one describing the heat conduction of electrons and the other that of the lattice, a model first proposed by Anisimov [34]. The electrons and phonons are described by two separate temperatures, T_e and T_p, and energy transfer between the two systems is assumed proportional to an electron-phonon coupling constant, G. Although the Boltzmann transport equation

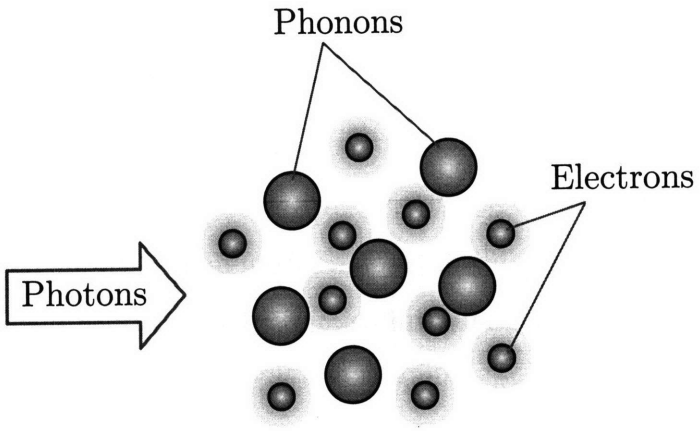

Figure 1-2: Absorption of photons in a metal. A subset of the electron population is excited by the incoming photons. The electrons thermalize over a few hundred femtoseconds, and then transfer their energy to the lattice over times on the order of ten picoseconds.

would provide a more sophisticated model for electron cooling and electron-phonon coupling, at room temperatures comparison with experimental data show that the two-temperature model is a good approximation for transport in the metal as soon as an electron temperature exists [24, 30, 31].

The electron-phonon coupling factor depends of the properties of the metal as well as the method of deposition [35]. To take two examples, for gold, typical values are on the order of 5×10^{16} W/m^{3}K, while for aluminum $G \sim 20 \times 10^{16}$ W/m^{3}K [35]. Although the electron-phonon collision time can be as short as the electron-electron collision time, the energy transfer from the electrons to the lattice will last much longer than the thermalization time of electrons due to the large momentum difference between electrons and phonons. In a 100 nm thick metal film, the hot electrons are thermalized and evenly distributed with 500 fs, and after this time we can estimate the electron-phonon thermalization time using two coupled first order equations:

$$\begin{aligned} C_e \frac{dT_e}{dt} &= -G(T_e - T_p) \\ C_p \frac{dT_p}{dt} &= G(T_e - T_p) \end{aligned} \tag{1.1}$$

Here C_e and C_p are the electron and phonon volumetric heat capacities, respectively,

T_e and T_p are the electron and phonon temperatures, respectively, and G is the electron-phonon coupling factor. The time constant τ for equilibrium is given by

$$\tau^{-1} = G(C_e^{-1} + C_p^{-1}) \tag{1.2}$$

This model is in fact a very poor approximation, since although the phonon heat capacity and electron-phonon coupling factor are approximately independent of temperature above 300 K, the electronic heat capacity varies linearly with the electron temperature [33]. Nonetheless, it allows us to roughly bound the equilibration time. The electron heat capacity will vary from the order of 1×10^4 J/m^{3}K at room temperature to 2–3 orders of magnitude higher immediately following pulsed heating [30], while for most metals $C_p \sim 2 \times 10^6$ J/m^{3}K. This gives a time constant anywhere between 1–100 ps. In reality, equilibrium between the two populations is typically established over a few to a few tens of picoseconds, a picture well verified by experiments [10, 36, 37].

An alternative, more simplistic way of estimating the time for the optical energy to become evenly distributed throughout the metal layer is to calculate the time constant for diffusion heat transfer in an insulated film [17]:

$$\tau \approx \frac{d^2}{\pi^2 \alpha} \tag{1.3}$$

where d is the film thickness and α is the thermal diffusivity. Taking a 100 nm film of aluminum as an example, τ ~10–30 ps. The range of times comes from the fact that the thermal diffusivity of the thin film may be significantly lower than that of bulk Al [17].

The temperature of the metal film is related to the intensity of the reflected probe beam through the thermoreflectance coefficient, $(\Delta R/R)\mathrm{K}^{-1}$. This quantity, which is dependent on the electronic band structure of the metal and the photon wavelength, is typically on the order of 10^{-4}–10^{-5} K^{-1} for common metals such as Al, Au, Cu and Ni [38, 39]. The majority of our measurements are made using an Al film, which has one of the strongest thermoreflectance coefficients with a peak around 800 nm,

matching the wavelength of our probe beam. Figure 1-3, taken from [39], shows the thermoreflectance spectrum for Al. It is assumed that the thermoreflectance coefficient is constant for small changes in temperature, an assumption we verify in Section 3.8.

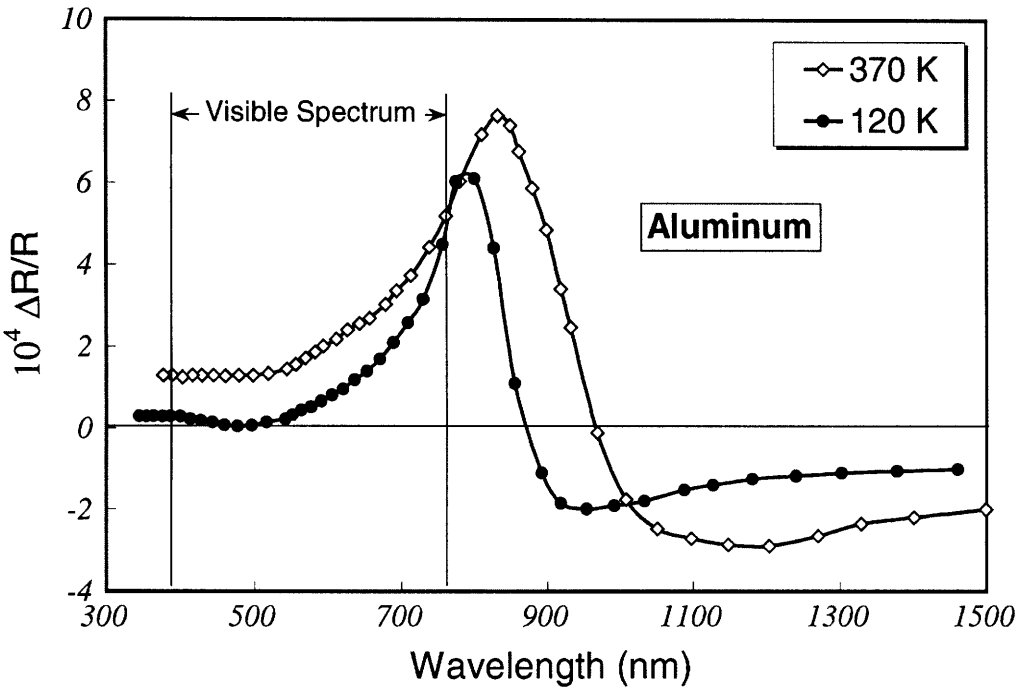

Figure 1-3: The thermoreflectance spectrum for Al, taken from [39].

1.2.2 Thermal Interface Conductance and Transport in the Substrate

The absorbed energy is transferred from the metal to the underlying substrate through phonon-phonon interactions, and, for an electrically conductive substrates, also electron-electron interactions. Both cases have been studied extensively and the topic is well covered in reviews [40, 41]. When the spectral nature of the heat carriers is ignored, thermal transport across the interface is modeled with a thermal interface conductance, G, and the heat flux across the interface is given by $q = G\Delta T$, where ΔT is

the temperature difference across the interface[1].

The interface conductance is usually calculated assuming either an acoustic mismatch model (AMM) [42], the acoustic analog of the Fresnel equations for electromagnetic waves, or a diffuse mismatch model (DMM) [40], which assumes purely diffuse phonon scattering at the interface. At low temperatures, when phonon wavelengths are long, a specular boundary condition is appropriate and the acoustic mismatch model agrees well with experimental results. At room temperature, the average phonon wavelength is ~10–20 Å in most materials, and an interface roughness of just a few atomic layers is sufficient to invalidate the specular boundary condition [43].

Although much research has been done, there is no generally accepted way to calculate thermal boundary resistance in this regime. Blind application of the DMM can lead to obviously incorrect results, such as the transmissivity between two similar materials approaching 0.5 instead of unity [43]. Part of the difficulty stems from the fact that a single temperature is not always an adequate concept to characterize different groups of phonons. The local phonon energy spectrum at the interface may be very different from that of the incoming phonons, and the equivalent equilibrium temperature which is measured in experiments and used in most calculations is really a measure of the local energy density and does not reflect the energy of only the phonons approaching the interface. Consequently care must be taken when defining temperatures in modeling thermal interface conducance [43].

Bulk disorder and imperfect physical contact between the two materials can potentially have a much larger impact than fundamental material differences and make the interface conductance sensitive to surface preparation and contamination [40, 41]. Systematic studies on thermal interface conductance between various solids have been carried out by Stoner et. al. [16] and Cahill et. al. [20–22], who also measured solid-liquid interface conductances [44, 45]. Typical values for G are on the order of 100–200 MW/m^{2}K, although they can be as low as 30 MW/m^{2}K for highly dissimilar materials [21] or as high as 400 MW/m^{2}K for metal-metal interfaces where electrons

[1]Unfortunately, G is the standard variable choice for both the electron-phonon coupling factor and the thermal interface conductance. For the remainder of this thesis, the two concepts will not be used in close proximity so confusion will be avoided.

play an important role [22].

Thermal transport in the substrate itself is mediated by phonon-phonon collisions and, in conductive materials, also by electron-electron collisions. In order to use the Fourier equation to model thermal transport, the carrier relaxation time should be much smaller than the time scale of interest. Phonon relaxation times are longest in ordered, crystalline solids where the regular atomic structure allows small wave-vector phonons to travel long distances before scattering off defects and impurities. Molecular dynamics studies on silicon, for example, indicate that at room temperature a significant portion of the heat is carried by long-wavelength phonons with relaxation times up to 100 ps or even longer [46], an effect that has also been hinted at experimentally [47]. In amorphous solids, disorder limits phonon mean free paths and the diffusion picture is valid after shorter times.

The majority of this thesis is focused on room temperature thermal transport in the diffusion regime. We have seen that the metal film will thermalize with a few tens of picoseconds, while it may take on the order of 100 ps for phonons in a crystalline substrate to behave diffusively. Therefore, the modeling in the following chapters is not expected to be valid for times less than $\sim$100 ps.

1.3 Organization of the Thesis

This thesis is essentially comprised of three parts. In the first, the theory, design and implementation of a pump-probe system is discussed. The work is built off the contributions of many others but includes some new experimental and theoretical contributions. In the second part, the techniques developed in the first part are applied to measure thermal transport in several systems, including bulk liquids, highly ordered pyrolytic graphite and semiconductor superlattices. In the final part, optical techniques are used to study the properties of suspensions of nanoparticles in liquid from both a microscopic and macroscopic perspective.

Chapters 2 and 3 contain the heart of the thesis. In Chapter 2, the design and implementation of a pump-probe system that is uniquely suited to thermal property

measurements is described in detail, including optics, instrumentation, and sources of noise. In Chapter 3, the theory for interpreting the measurement results in the diffusion regime is developed, tying together and extending the work of other authors. A linear systems approach is used to model the measured signal in a clear consistent way, and special attention is given to the role of pulse accumulation and its relationship to radial conduction effects. Cross-plane thermal conductivity measurements of thin-film and bulk samples spanning thermal conductivities over two orders of magnitude are presented, verifying the system performance, and different approaches to fitting the data are discussed, along with the importance of sample preparation on the thermal interface and thermal conductivity measurements.

In Chapter 4, the pump-probe technique is extended into new territory. In the first section, the technique is adapted to measure the thermal properties of bulk liquids and malleable solids. This method provides a convenient way to measure liquid volumes as thin a 500 nm and also has the potential to measure solid–liquid thermal interfaces. Results spanning the range of commonly encountered liquid thermal conductivities are presented to verify the method's accuracy. In the second section, the theory developed in the previous chapter is used to analyze the sensitivity of the method to in-plane properties. Measurements on highly ordered pyrolytic graphite are shown to be in good agreement with literature, and some preliminary results for a Si/Si_xGe_{1-x} superlattice structures are presented as well. Finally, we briefly touch on the use of pump-probe for the characterization of microstructures, using a ZnO nanobelt as an example.

In Chapter 5, we turn to nanoparticle-seeded fluids, or "nanofluids," a topic which has received considerable attention in recent years[11, 48], and approach the topic from two different perspectives: (1) heat transfer between an individual nanoparticle and the surrounding fluid, and (2) the bulk thermal and viscous properties of the suspension. For the first case, we use the same pump-probe system described in the previous chapters, reconfigured for transmission geometry rather than reflection. The heat transfer dynamics of the individual nanoparticles are measured, and the critical role played by surfactants in the thermal transport between the particle and the sur-

rounding fluid is studied systematically. In the second case, we use a different optical technique, impulsive stimulated thermal scattering (ISTS)[49], which belongs to a class of techniques known as transient grating (TG) methods. The experimental apparatus for this measurement was constructed by students in the Keith Nelson group in the Department of Chemistry at MIT. Thermal conductivity measurements show that the observed thermal conductivity enhancement of nanofluids is repeatable and is not a function of the measurement technique, while acoustic attenuation measurements indicate that the nanoparticles do not form clusters in solution. Combined, the contents of Chapter 5 provide an experimental picture of nanofluids from the nanoscale to the macroscale.

Finally, Chapter 6 ties together the thesis and provides an outlook for future developments of the pump-probe technique that will continue to expand the boundaries of thermal measurement.

Chapter 2

The Experimental System

In Chapter 1, we briefly reviewed some of the previous work on pump-probe measurements of thermal transport in thin films and across interface. The first system, constructed by Paddock and Eesley [13], used two synchronously pumped dye lasers to pump and probe the sample at 633 nm and 595 nm, respectively, with pulse widths on the order of 6 ps and a repetition rate of 246 MHz. Capinski and Maris [15] added several improvements. They used a single dye laser operating at 632 nm and a repetition rate of 76 MHz that had a significantly shorter pulse width, 0.2 ps, allowing them to study acoustic phenomena as well as thermal diffusion. In addition, they incorporated an optical fiber after their delay stage that eliminated errors associated with probe beam misalignment and divergence over the length of the delay stage. More recently, Cahill and coworkers developed a system using a Ti:Sapphire oscillator to produce pump and probe pulses 150 fs long with a central wavelength of 790 nm and a repetition rate of 80 MHz. Their system added several novel features, such as an integrated CCD camera for visualizing the sample and beam spots, a geometry which allows for a single objective lens to focus both pump and probe beams, and inductive resonators in series with the photodetector which increase the signal-to-noise ratio by a factor of 10 or more [19, 50].

We have constructed a pump-probe system in the Warren M. Rohsenow Heat and Mass Transfer Laboratory at MIT. Our system incorporates several of the features from the systems listed above and adds additional improvements that will be dis-

cussed below. Like Cahill et. al., we use the output of our Ti:sapphire oscillator at 80 MHz without amplification. Compared with lower repetition-rate systems, this has the advantage of a much higher signal-to-noise ratio because shot-to-shot noise is averaged, and because it allows us to modulate the pump beam at high frequency, reducing $1/f$ noise as discussed in Section 2.4 This allows us to work with small temperature excursions for our samples; the peak energy density of the pump pulses is on the order of 1 J/m^2, which usually leads to a temperature rise of less than 1 K for a single pulse. Other features borrowed from Cahill's system include the integrated CCD camera and the use of inductive resonators.

At a pulse repetition rate of 80 MHz, the time between laser pulses is only 12.5 ns. For many situations, including the majority of thermal conductivity measurements, this is not sufficient time for the system to return to equilibrium. In this case, the effects of multiple pules accumulate, and the measured signal will be different from the response to a single pulse. We will see in Chapter 3 that, while this complicates the analysis, it also make the experimental technique more powerful by essentially probing two length scales simultaneously. Some novel features of our system include a frequency-doubled pump beam, which drastically reduces optical noise and allows for a simplified coaxial geometry, and an expanded probe beam which reduces divergence over the length of our delay stage.

In the early stages of building and testing our pump-probe system, we struggled to obtain reliable, consistent results. In retrospect, this was not due to a single error in experiment or analysis, but the result of many small factors that each contributed uncertainty and error to the final result. These include effects due to laser spot size and shape, various sources of electronic and optical noise, variation in sample quality and preparation, and false assumptions in the data interpretation.

In this chapter, we describe the design and implementation of our pump-probe system. All the details necessary to obtain an accurate measurement are included. We begin with an overview of the optical system and its major components, and then move on to some small but essential details of the instrumentation, and finally discuss the various sources of noise that can affect the measurement.

2.1 Optics

A schematic containing the essential features of our pump-probe system is shown in Fig. 2-1. The system is built around a tunable Ti:Sapphire laser which emits a train of 200 fs pulses at a repetition rate of 80.7 MHz. The center wavelength is 800 nm and the power per pulse is roughly 15 nJ. The frequency spectrum of the laser in pulsed operation is shown in Fig. 2-2(a.). The spectrum was obtained using a monchromater. The transform-limited pulse-width is calculated from the Fourier transform of the frequency spectrum; this is shown in Fig. 2-2(b.). The transform limit is the shortest possible pulse width, as it assumes a frequency-independent spectral phase. Although many mode-locked lasers can achieve close to transform-limited pulse widths, a true pulse width measurement requires a more advanced technique such as interferometric autocorrelation or frequency-resolved optical gating [51]. For our applications, the precise details on the pulse shape and width are not critical so this was not done.

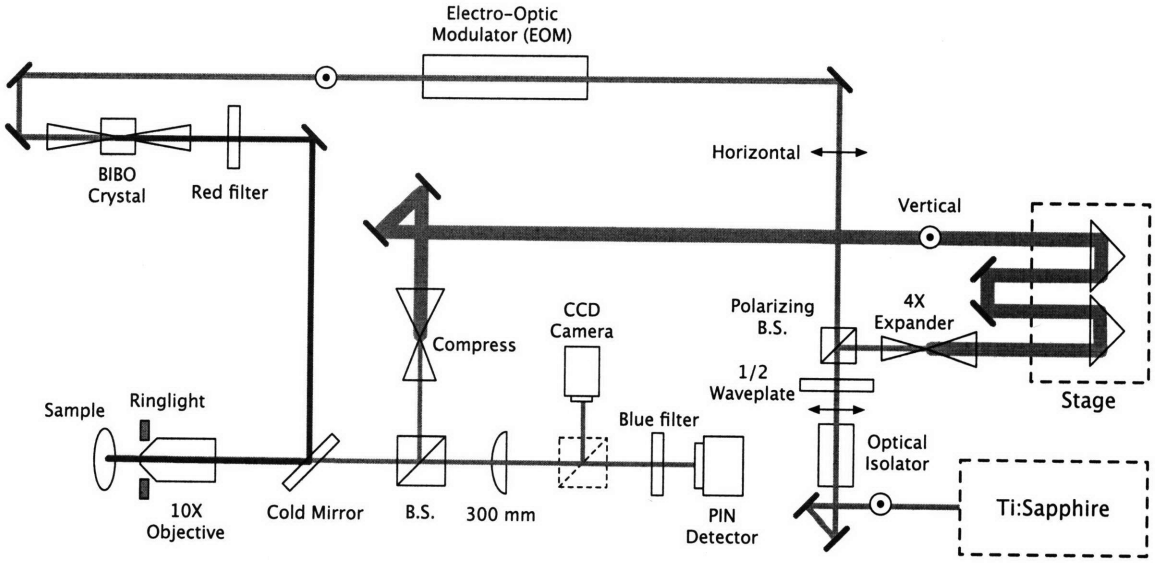

Figure 2-1: A schematic of the key elements of our pump-probe system. After the first beam splitter, the probe beam passes through a 4× beam expander to minimize divergence over the two meters (~7 ns) of delay, after which it is compressed before being directed onto the sample through an objective lens at normal incidence. The pump beam passes through an electro-optic modulator (EOM) and then a bismuth triborate (BIBO) crystal where it is frequency-doubled to 400 nm. The doubled light is directed through the same objective lens onto the sample, coaxial with the probe beam.

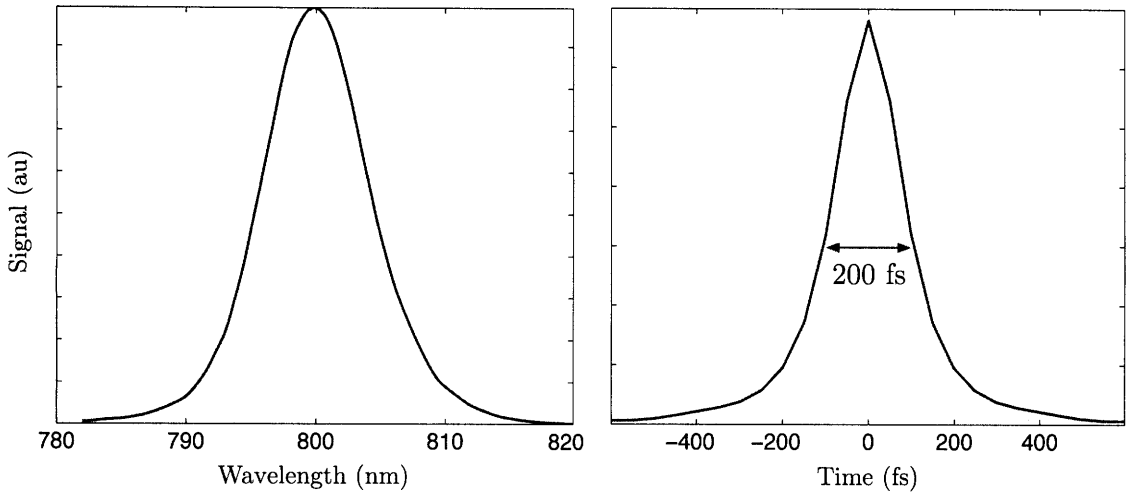

Figure 2-2: (**a.**) Frequency spectrum emitted by the Ti:Sapphire laser in pulsed operation at a center wavelength of 800 nm, and (**b.**) the transform-limited pulse width determined by a Fourier transform of the spectrum.

The main beam passes through an optical isolator (Electro-Optics Technology, Inc., model BB8-51) to prevent back reflections from de-stabilizing the laser, and is then divided into pump and probe arms with a polarizing beam-splitter; a 1/2 waveplate is used to control what fraction of light goes into each arm. Typically about 40 mW, or 3–4% of the total laser power, is split off for the probe arm and the remainder is used for the pump.

The probe beam is expanded with a pair of lenses from a $1/e^2$ diameter of $\sim$ 2 mm to 8 mm, and its optical path is adjusted up to 2.1 meters (7 ns) with a double-pass delay stage. The purpose of the beam expander is to minimize divergence of the probe beam at long delay times. A perfectly columnated beam with $1/e^2$ radius w_0 will diverge according to [52]:

$$w = w_0 \left[1 + \left(\frac{\lambda z}{\pi w_0^2} \right)^2 \right]^{1/2} \tag{2.1}$$

Here w is the $1/e^2$ beam radius, λ is the wavelength and the z is the propagation distance. Without expansion, our beam radius would increase by $\sim$12% at maximum delay, translating roughly into a corresponding increase in focused spot size. After

expansion, Eq. (2.1) yields an increase in radius of only 0.02%. The characterization of beam spot size and motion is discussed in section 2.2; the results are that the probe radius changes by around 2% (most likely higher than predicted because of a non-ideal beam shape and lens aberrations) and undergoes a lateral shift of roughly 250 nm over the entire 7 ns of stage delay. Compared to the option of using an optical fiber after the stage to maintain beam shape [15], the expander has the advantage that the probe power remains constant over the delay, eliminating the need for a normalizing detector. After the stage, the probe beam is compressed and directed through the center of a 10× objective at normal incidence. Changing the ratio of the compressor to the expander allows us to adjust the focused probe size by changing the diameter of the collimated probe beam into the objective lens.

The pump beam is modulated with an electro-optic modulator (EOM) (Conoptics, Model 350-160) which imposes a square-wave modulation on the beam, with a frequency up to 20 MHz. The purpose of the modulation is to provide a reference for a radio-frequency lock-in amplifier (SRS Model 844) which is used for signal detection. A good summary of the principle of lock-in detection is provided in the instrument's user's manual. [53]

In order for the lock-in approach to be effective, none of the pump light, which is modulated at the reference frequency, can reach the detector. This is essential since even a small amount of stray light modulated at the reference frequency could overwhelm the measurement. Other pump-probe systems described in the literature send the pump and probe beams onto the sample at significantly different angles to isolate the pump beam spatially [15, 18], or use a combination of a beam block and polarization to achieve the same purpose [5]. Both approaches are vulnerable to scattering into different angles and polarizations by rough samples, and using separate lenses at different angles to focus the pump and probe beams onto the sample makes achieving precise overlap of the two beams more difficult.

In our system, we use second harmonic generation (SHG) and a co-axial geometry to simplify alignment and give superior resistance to optical noise from the pump beam. After the modulator, the beam is focused with a 6 cm focal length lens onto

a piece of bismuth triborate (BIBO) crystal [54], a nonlinear optical medium used for second harmonic generation from the visible to infrared. The BIBO crystal is 2 mm thick and was cut for SHG at 800 nm. The conversion efficiency from 800 nm to 400 nm in our system is greater than 20%, resulting in more than 120 mW of modulated 400 nm light.

Both 800 nm light and 400 nm light emerge from the BIBO crystal. We use cold mirrors and a red filter to remove the 800 nm light after the crystal. In addition, we place a blue filter in front of the detector to eliminate any blue light that scatters off the sample. The filters are very effective at removing the unwanted light, and are insensitive to polarization. The two-color arrangement thus makes it possible to measure samples that are rougher than would otherwise be possible.

The 400 nm light emerging from the BIBO crystal is re-columated using a second lens. By changing the distance of this lens from the crystal, the divergence of the beam and therefore the final focused size on the sample can be varied from a $1/e^2$ diameter of 8 μm up to more than 100 μm. Both pump and probe beam are directed coaxially into a long-working-distance 10$\times$ objective. This arrangement make alignment relatively simple and ensures that the spots are not distorted.

When the sample is at the focal plane of the objective, the probe beam is retro-reflected and emerges collimated from the objective. A 300 mm focal length lens is used to focus the beam onto a high speed PIN photodiode (Thorlabs DET10A) with a rise time of 1 ns. A removable mirror can be placed in the probe path to direct the light into a CCD camera, essentially creating a microscope that can be used to view the sample. A ring light mounted on the objective lens generates enough scattered light to create a dark-field image of the sample [22]; the magnification of the microscope is roughly 15$\times$.

The CCD system is essential for three reasons. First, it enables the user to view the sample in detail and accurately determine which regions are measured. Second, it makes for a simple visual way of overlapping the pump and probe spots. And third, bringing the sample into focus ensures that it is a known distance from the objective, so that the sizes of the focused beam spots are known. Measurement of the beam

spots is the subject of the next section.

2.2 Beam Spot Characterization

The Ti:Sapphire produces a TEM_{00} beam with an approximately Gaussian intensity profile

$$I(r) = \frac{2A_0}{\pi w_0^2} \exp\left(\frac{-2r^2}{w_0^2}\right) \tag{2.2}$$

where A_0 is the total power in the beam and w_0 is the $1/e^2$ beam radius. When the beam is focused onto the sample, it retains this distribution although the beam radius changes. As we will see later, the radii of the pump and probe beams are important parameters in the heat transfer into the sample, so accurate characterization of them is necessary.

We use a knife-edge profiling technique to measure the spot sizes. The approach is illustrated in Fig. 2-3. A razor blade mounted on a precision stage with a resolution of 100 nm is advanced into the beam at the focal plane, determined by observing when the razor edge is in focus on the CCD camera system. If the blade motion is in the x direction, the total intensity at the detector is given by:

$$I(x) = \frac{2A_0}{\pi w_0^2} \int_{-\infty}^{\infty} dy \ \exp\left(\frac{-2y^2}{w_0^2}\right) \int_{-\infty}^{x} dx \ \exp\left(\frac{-2x^2}{w_0^2}\right) \tag{2.3}$$

A photodiode records the total transmitted intensity at each location; taking the derivative of the resulting curve yields the intensity profile in the x direction. The data is the fit with a Gaussian profile to extract the $1/e^2$ spot radius.

Figure 2-4 shows the measured pump and probe spots. Typically, a pump spot $1/e^2$ radius of 25–30 μm is used while the probe spot radius is ~ 4 μm. As discussed later, this arrangement minimizes sensitivity to the spot size and eliminates possible beam walk-off errors caused by misalignment of the probe translation stage.

The method described above yields the $1/e^2$ radius of a beam profile, but it is only a 1-D measurement. If the beam is elliptical, the results will not be accurate. The beam shape can be determined by viewing the scattered light from a diffuse

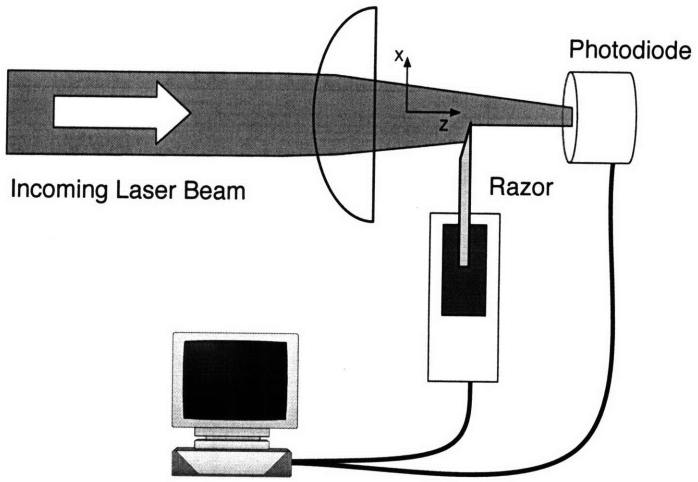

Figure 2-3: Knife-edge beam profiling system used to characterize the pump and probe spots.

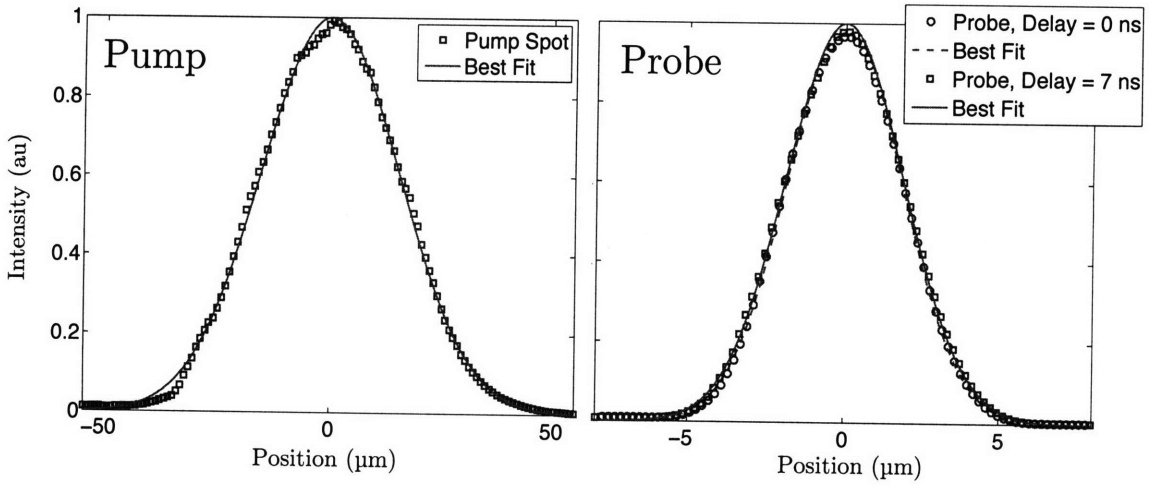

Figure 2-4: Measure profiles of the focused pump spot (left) and probe spot (right) along with the bet fit curves. The pump $1/e^2$ radius is 30 μm; the probe spot is shown at maximum and minimum delay. The radius is 3.7 μm at zero delay, 3.8 μm at maximum delay.

surface; an image of the pump spot is shown in Fig. 2-5. More detail can be obtained by focusing the beams onto a surface that is modified by the light, leaving behind intensity contours. We used a BiTe composite to do this. The resulting contours of both pump and probe spots are shown in Fig. 2-6.

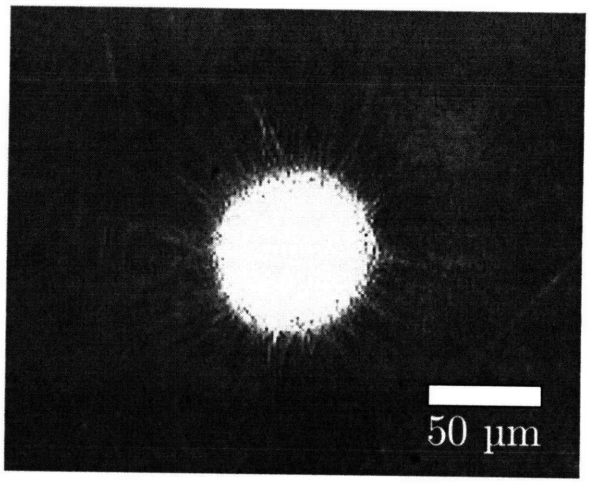

Figure 2-5: CCD image of the pump spot on a diffuse surface. The spot is approximately circular.

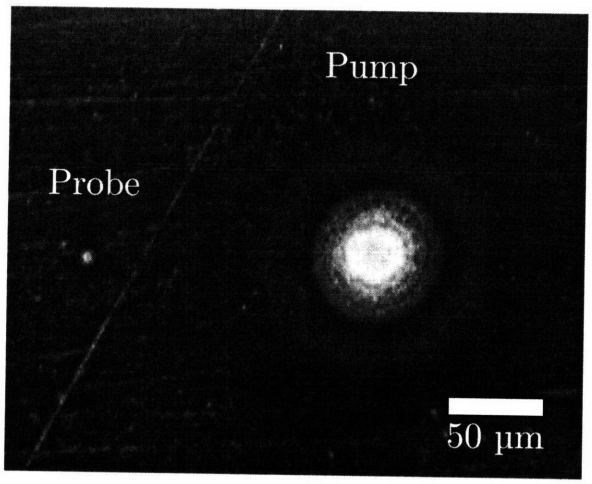

Figure 2-6: Intensity contours left in a BiTe composite by the pump and probe spots. The contours from the pump spot are easily visible and quite circular; the probe spot contours are harder to discern.

There are situations when it is desirable to have both spots small, for example when trying to characterize radial conduction or when very high pump fluence is

required. In these cases, good alignment of the probe path with the stage is important and the lateral translation should be characterized. Backlash in the stage for the knife-edge measurement prohibited repeatable absolute position measurements of the probe spot at different delay times. Instead, the blade was moved into the focused spot until the intensity was reduced by half. Then the stage was moved across the range of travel and the change in power was measured to be less than 5%. The change of measured power with beam shift, dA/dx, is given by the derivative of Eq. (2.3). Rearranging, we write

$$dx = \frac{w_0\sqrt{2\pi}}{2}\frac{dA}{A_0} \tag{2.4}$$

where dA/A_0 is the fractional change in power. Putting in the probe radius, 3.8 μm, yields a lateral shift dx of just 250 nm over the full 7 ns (2.1 m) of delay. In most practical situations, this is negligible. While it is only a measure of the shift in one direction, it gives a good idea of the overall alignment.

2.3 Instrumentation

A good optical setup is necessary but not sufficient to obtain a good measurement; the right electronics and an understanding of their limits are also required. The core electronic components have already been mentioned: the PIN photodiode, electro-optic modulator (EOM), and lock-in amplifier. However, there some additional components that play important parts as well.

A key challenge of a thermoreflectance measurement is that the change of reflectance with temperature is small – on the order of 10^{-4} or less. Thus the change in signal due to temperature is obscured by the large DC background component of reflection. The standard technique to overcome this issue is to use a lock-in amplifier, which employs phase-sensitive detection to extract the signal at a specified reference frequency from the background. A good summary of the principle of lock-in detection is provided in Chapter 2 of the user manual of our lock-in (Stanford Research Systems model SR844) [53].

In theory, the lock-in will only measure signals within a narrow bandwidth around

the reference frequency. However, in reality the SR844 mixes the measured signal with a square wave, not a sinusoid. The EOM, which provides the reference signal, also modulates the pump beam with a square wave (with a rise time of <8 ns). As a result, the signal contains contributions at all the odd harmonics of the reference frequency, with relative amplitudes of $1/n^2$ where n=1, 3, 5 ....

To remove the higher harmonics, we place an inductor in the signal line between the photodiode and the lock-in amplifier. The inductor forms a resonant filter with the photodiode at the reference frequency and increases the signal by a factor of 10 or more compared to other frequencies [50]. The filter behavior can be explained by considering a simplified circuit of the PIN photodiode, shown in Fig. 2-7. The diode is modeled as a current source in parallel with a capacitance C_J. The source of the capacitance is the depletion region in the PIN diode; for our diode size and reverse bias voltage, $C_J \sim 20$ pF. The input impedance to the lock-in, R_{LI}, is on the order of 50 Ω, and the inductive element is chosen so the circuit resonates at the reference frequency of interest.

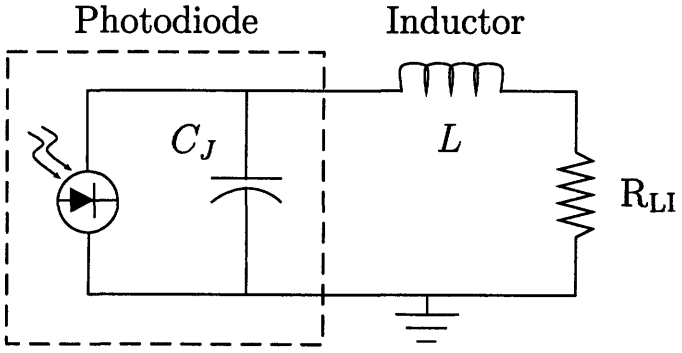

Figure 2-7: Simplified circuit diagram for the PIN photodiode. The dashed line contains the diode. The inductor is placed in the signal line to the lock-in amplifier.

In the frequency domain, the voltage response V of the circuit in Fig. 2-7 to a periodic input current of amplitude I and frequency ω is given by:

$$V = I\left[\left(\frac{-i}{\omega C_J}\right)^{-1} + (Lj\omega + R_{LI})^{-1}\right]^{-1}\left(\frac{R_{LI}}{Li\omega + R_{LI}}\right) \tag{2.5}$$

In the case where $L\omega \gg R_{LI}$ and Eq. (2.5) simplifies to

$$V = I\left(\frac{R_{LI}}{1 - LC_J\omega^2}\right) \tag{2.6}$$

This provides a quick way to estimate the resonant frequency: $\omega_0 \approx 1/\sqrt{LC_J}$.

Two measured responses from the lock-in amplifier with different inductive resonators in place are shown in Fig. 2-8, along with the curves calculated using Eq. (2.5). The junction capacitance, C_J, is taken as 18.5 pF in both cases, and the inductors L are 100 μH and 10 μH. The combined resistance R_{LI} of the inductor and lock-in input impedance is adjusted slightly to match the width of the curves; 120 Ω is used for the 100 μH resonator while 80 Ω is used for the 10 μH resonator. Figure 2-9 shows the output from the photodiode at the reference frequency with and without an inductive filter; with the filter in place, the higher harmonics have been removed, leaving a pure sinusoid.

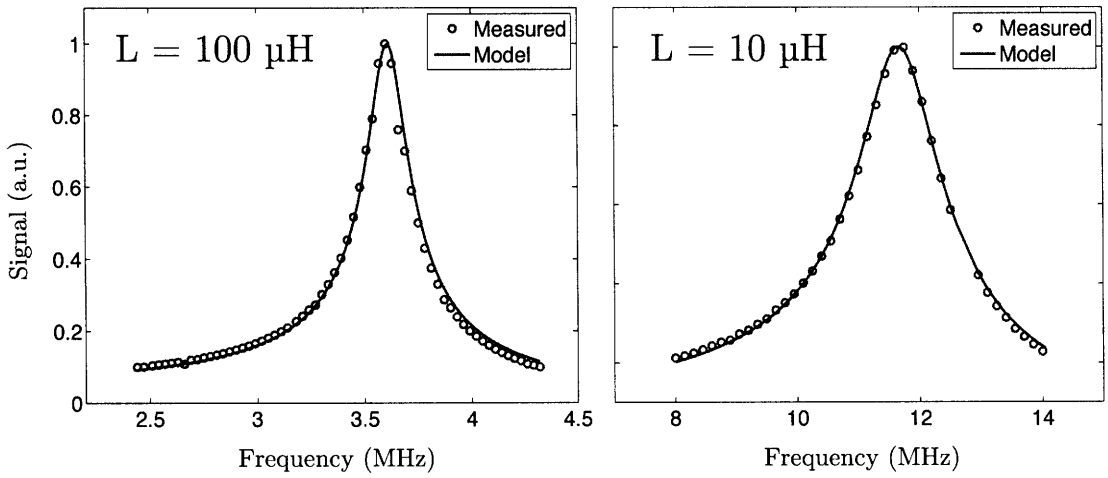

Figure 2-8: Response from the lock-in amplifier for two inductive resonators, one with 100 μH of inductance (left) and another with 10 μH of inductance (right). The junction capacitance C_J is taken as 18.5 pF in both cases. The combined resistance R_{LI} of the inductor and lock-in input impedance is adjusted slightly to match the width of the curves; 120 Ω is used for the 100 μH resonator while 80 Ω is used for the 10 μH resonator.

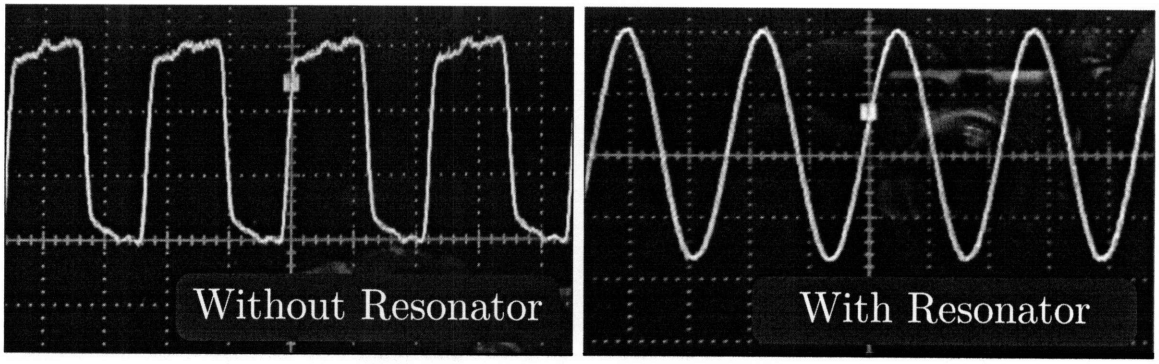

Figure 2-9: The measured output of the photodiode at a reference frequency, with and without the inductive resonator. The resonator effectively removes the higher harmonics, leaving a pure sinusoid. The offset is arbitrary.

2.4 Sources of Noise

Several sources of noise are present in the system and impact the overall signal-to-noise ratio. Care should be taken to minimize them and properly cancel out any systematic offsets to produce a good measurement. Fundamental sources of noise include Johnson noise and shot noise, which come from thermal fluctuations and the finite nature of the charge carriers, respectively. Of these, shot noise dominates in the photodiode [55]. The relative shot noise in the probe beam is $\sqrt{2e/I} \sim 2\times10^{-8}/\sqrt{\text{Hz}}$ for our typical signal levels, where e is the electron charge and I is the photocurrent generated by the diode.

The main source of noise comes from $1/f$ noise, or "pink noise," fluctuations in the probe intensity around the reference frequency. Pink noise is a spectral noise distribution that arises in many physical systems [56]. In the probe beam, $1/f$ noise results in signal fluctuations around $2\times10^{-7}/\sqrt{\text{Hz}}$ at the reference frequency around 10 MHz. Our normal lock-in settings give a measurement bandwidth of 10 Hz, giving signal fluctuations of 6×10^{-7}. Since the signals we are measuring are on the order of 10^{-4}–10^{-5}, there is ample signal-to-noise ratio. At frequencies below 1 MHz, the $1/f$ noise fluctuation increases to $\sim 10^{-6}/\sqrt{\text{Hz}}$. The signal is still measurable, although a slower lock-in time constant, which reduces the measurement bandwidth, is needed to obtain clean results.

In addition to electronic noise, coherent radio frequency (RF) pickup adds a steady offset to the signal. The signal and reference cables and even the power cord into the lock-in act as antennae, picking up signals at the reference frequency, an effect that is most prominent at frequencies from 5 MHz upward. To make matters worse, simply walking close to the instrument changes the surrounding field and causes the pickup to fluctuate. This makes it difficult to cancel out the RF pickup. To overcome this, we use RF chokes to attenuate RF current flowing along the the outside of the coaxial signal lines and in the power cord. The chokes are ferrite toroidal cores around which the cables are wrapped; a few turns around the toroid are sufficient to significantly reduce coherent pickup. Figure 2-10 shows the arrangement of the RF choke.

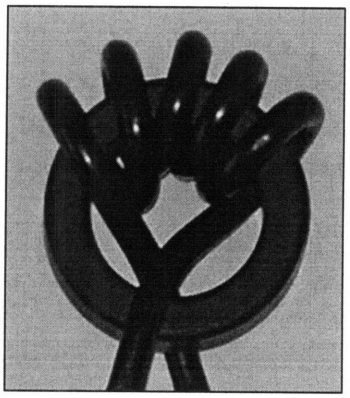

Figure 2-10: A ferrite toroidal core used as an RF choke.

The last source of noise to be considered is optical noise. Scattered pump light at the modulation frequency can easily overwhelm the measurement. In systems that use the same frequency light for both pump an probe, this is a major concern. However, in our system the color filters are extremely effective and blocking or unblocking the pump beam produces no obervable effect on the signal.

Before every measurement, any RF pickup and other DC offsets must be subtracted from the lock-in signal. With the sample in place, we block the pump beam but leave the probe beam unblocked, allowing it to reflect from the sample into the detector. This produces a small signal due to the frequency component of the probe beam at the reference frequency. In addition, there is an offset due the RF pickup (the

RF chokes cut down on the RF fluctuation but a small DC level remains). We zero the lock-in at this level, and then unblock the pump beam and make the measurement. In systems where scattered pump noise is a concern, a separate measurement of the signal with the probe beam blocked and the pump beam unblocked should be made, and this signal should be subtracted from the measurement as well.

2.5 Summary

The design and implementation of a pump-probe system has been described in detail. Our system incorporates many of the best aspects of systems built by others, notably Paddock and Eesley [13], Capinski and Maris [15], and Cahill [19, 50], while adding some new features such as a frequency-doubled pump beam, an expanded probe beam and a coaxial geometry, which reduce errors associated with optical noise, beam divergence, and spot shape and alignment, respectively. Many of the nitty-gritty details, which are so important to a successful measurement but are often left out of published material, have been included in the hope that they may be useful to anyone attempting to duplicate and extend our work.

Chapter 3

Theory and Data Analysis

In all variations of the pump-probe technique, the data is compared to a model of the system, and the unknown properties of interest are adjusted to minimize the error between the model and the data. We can divide the modeling into two distinct parts. The first part relates the output of the lock-in amplifier to the probe beam input to the photodiode. The resulting expression is given in terms of the impulse response or frequency response of the system being probed; the only limitation is that the excitation process must be modeled as a linear time-invariant (LTI) system. This is done in Section 3.1. The second half of the modeling is to solve for the thermal response of the sample. An analytical solution is given for heat flow in layered media, including the effects of radial heat flow from coaxial gaussian laser spots and thermal interface resistances. This is done in Section 3.3.

3.1 The Thermal System as an LTI System

3.1.1 Introduction

As we mentioned at the beginning of Chapter 2, we use the fundamental output of our Ti:sapphire oscillator at 80 MHz without amplification, which gives a high signal-to-noise ratio and allows us to work with small temperature excursions for our samples. However, the time between laser pulses is only 12.5 ns, and for many situations,

including the majority of thermal conductivity measurements, this is not sufficient time for the system to return to equilibrium. In this case, the effects of multiple pulses accumulate, and the measured signal will be different from the response to a single pulse. This accumulation phenomenon was first described by Capinski et. al. [15] in terms of the impulse response of the sample. This work assumed one-dimensional thermal transport. Modeling was later extended to the frequency domain by Cahil [19] to account for radial heat conduction in an isotropic medium, although the details on the interplay between pulse accumulation and radial transport effects were not explicitly discussed.

In this section, we use the theory of linear time-invariant (LTI) systems to derive the measured signal in terms of the impulse response and the frequency response of the sample in a straightforward, consistent way. Then, in Section 3.2, we look more carefully at the accumulation effects. We will see that, while they complicate the analysis, they also make the experimental technique more powerful by essentially probing two length scales simultaneously.

The theory of linear time-invariant (LTI) systems is well-developed and is commonly used in many fields, especially signal processing and control systems [57]. Such systems posses the property of superposition: the response of the system to multiple inputs is the sum of the responses to each individual input. In conduction heat transfer, if the temperature changes are small enough that physical properties can be assumed constant, the temperature of the system obeys superposition [58]. This provides a convenient way to handle many heat conduction problems, especially those involving a periodic or other time-varying heat input. In the end, we seek a thermal "transfer function," complex number, $Z(\omega)$, where ω is the period thermal input frequency, such that the output of the lock-in amplifier for a reference wave $e^{i\omega_0 t}$ is given by

$$Ae^{i(\omega_0 t+\phi)} = Z(\omega_0)e^{i\omega_0 t} \tag{3.1}$$

Here the amplitude, A, and phase, ϕ, of the lock-in output will be functions of the delay between the pump and probe pulses and the physical properties of the

sample. The reference frequency, ω_0, will be set by the EOM modulation of the pump beam. The transfer function is represented pictorially in Fig. 3-1. We represent the modulation using the complex exponential $e^{i\omega_0 t}$ for mathematical convenience; it is understood that the actual signal is represented by the real part of Eq. (3-1).

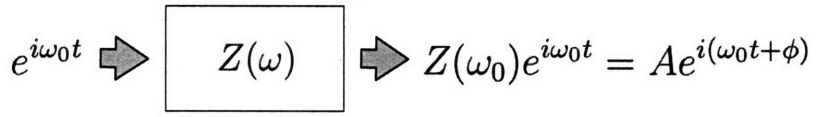

Figure 3-1: Transfer function representation of the measurement. The transfer function, $Z(\omega)$, contains the thermal response of the system as well as the properties of the pump and probe beams.

In this section, we model the output of the lock-in amplifier in two ways: in terms of the system impulse response, $h(t)$, and in terms of the frequency-response, $H(\omega)$. The impulse-response solution is convenient for numerical simulations, while the frequency-response solution is more useful when an analytical solution for the temperature in the frequency domain is known. The assumption that the thermal system is an LTI system is verified later by showing that normalized results for different input power levels are virtually identical.

To begin, we consider the response of the thermal system to a train of pulses modulated by a sinusoid. In our system, laser pulses from the pump beam arrive at the substrate with a frequency of 80 MHz, and each individual pulse has a width on the order of 200 fs. Because the pulse width is much shorter than the processes we are modeling, each individual pulse is treated as an impulse with energy Q.

The actual output of the EOM is a square wave with an 8 ns rise time that oscillates between zero and the full power of the pump beam. This signal can be broken up into its Fourier components, and because the system is linear, we can consider the response to each component independently. An ideal lock-in rejects all frequencies except those in a very narrow band around the fundamental frequency (typically less than 10 MHz). Therefore, we only need to consider the response to the fundamental harmonic. A more rigorous proof of this is provided in Appendix A.1. In our case, the lock-in mixes with a square wave and the odd harmonics would have

a small effect, but the inductive filter placed after the photodiode effectively removes these higher frequencies, as we discussed in Section 2.3. After a short period of time, the system reaches a quasi-steady state and we can ignore the DC offset as well, since it will also be rejected by the lock-in amplifier.

Figure 3-2 depicts the heat input to the sample, considering only the fundamental modulation frequency and ignoring the DC offset, as discussed above. Each impulse of heat generates a temperature response in the sample, which in general does not die away before the next pulse arrives. Figure 3-3 shows a representation of the surface temperature in response to the pump pulses.

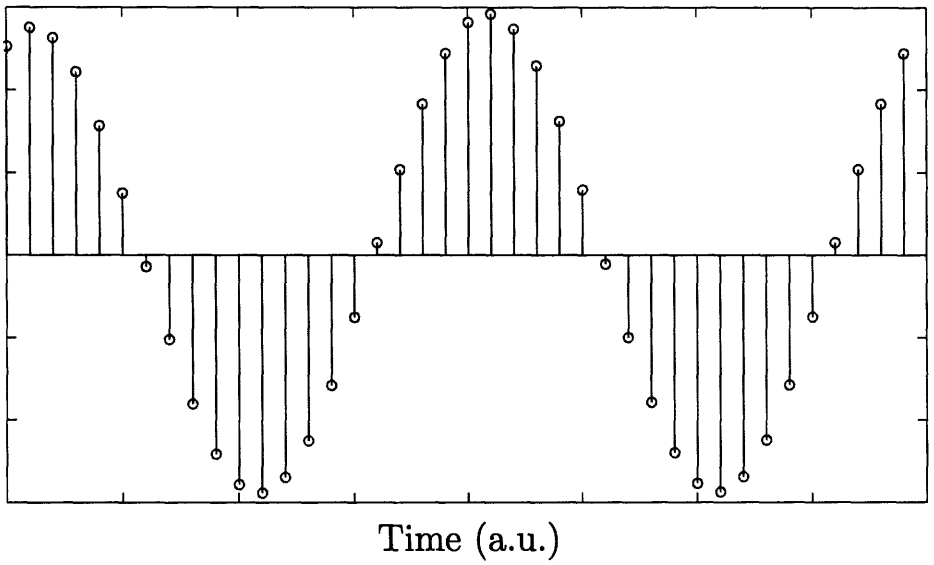

Figure 3-2: Representation of the pump beam after passing through the EOM. Although the true modulation of the EOM is a square wave with a DC offset, in steady state the lock-in amplifier only measures the fundamental harmonic, so an idealized sinusoid may be used.

The probe pulses arrive at the sample delayed from the pump pulses by a time τ, determined by the position of the delay stage. These pulses are reflected by the sample back into the photodiode. Figure 3-4 depicts the probe pulses sampling the surface temperature. Although the probe pulses also excite the sample, and indeed may even be stronger than the pump pulses, this has no effect on the measurement. This is because the probe beam has no frequency component at the modulation frequency and thus its contribution to the signal will be rejected by the lock-in. To see this, in

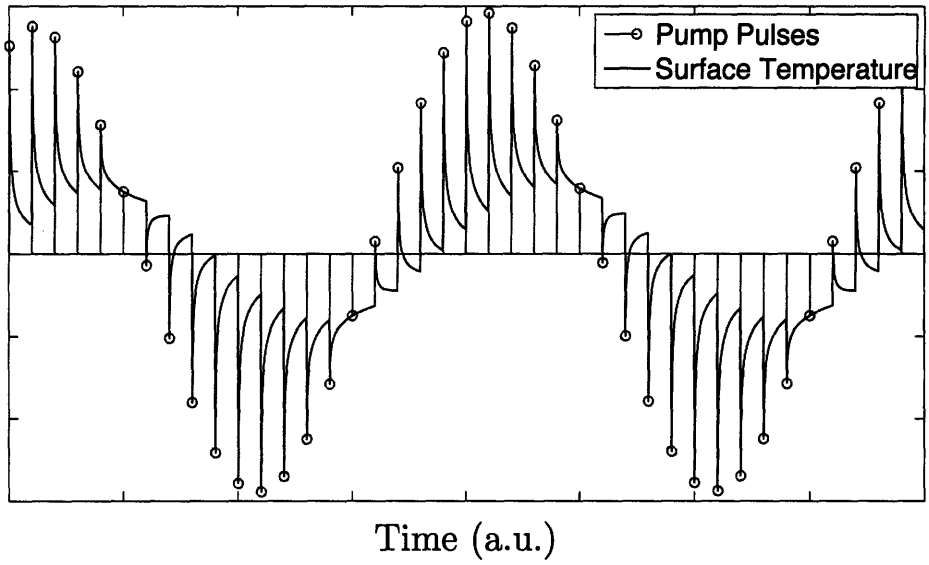

Figure 3-3: The surface temperature of the sample in response to the pump beam input described in Fig. 3-2

the time domain the probe signal can be represented by:

$$p(t) = \sum_{n=-\infty}^{\infty} \delta(t - nT - \tau) \tag{3.2}$$

where δ is the delta function, T is the period between pulses and τ is the delay time between pump and probe pulses. In the frequency domain, this becomes [57]

$$P(\omega) = \left[\omega_s \sum_{k=-\infty}^{\infty} \delta(\omega - k\omega_s)\right] e^{-i\omega\tau} \tag{3.3}$$

where we have defined ω_s as the "sampling frequency," $2\pi/T$. Equation (3.3) evaluates to zero for all frequencies except multiples of ω_s. In our experiments, ω_s (80 MHz) is one to two orders of magnitude larger than the modulation frequency (1–10 MHz). Typically, in our experiments the lock-in amplifier time-constant is around 30 ms, which gives a pass band of roughly 10 Hz [53]. Therefore, all of the probe frequencies will be well outside the lock-in pass band, and we can safely ignore the probe pulses' effect on the measurement. Instead, we can view them as simply measuring the state of the thermal system at a time τ after the pump pulses.

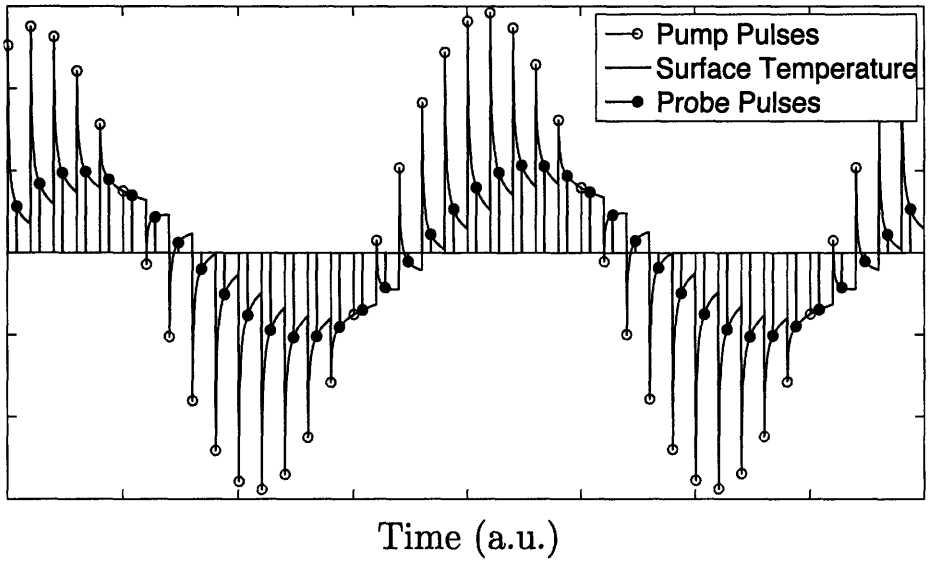

Figure 3-4: The probe pulses arriving at the sample, offset by a delay time set by the stage. Since the probe beam is not modulated by the EOM, the effect of the probe pulses on the surface temperature can be neglected. This assumption is valid as long as the probe beam is not strong enough to cause the sample to behave in a nonlinear way.

Collectively, these probe pulses excite the photodiode. The component of this probe signal at the reference frequency will be recorded by the lock-in amplifier, while all other frequencies will be rejected. Figure 3-5 "connects the dots" of the probe pulses to highlight the fundamental harmonic component. Both its amplitude and phase lag with the reference modulation are recorded by the lock-in at each delay position. It is the task of the next two sections to represent this harmonic component in terms of the thermal impulse response and frequency response, respectively.

3.1.2 Signal Analysis Using the Impulse Response

To begin, consider Fig. 3-6, which shows a close-up view of Fig. 3-4. The time period between pulses is T, and the delay time between the pump and probe pulses is τ. We first write an expression for the reflected probe intensity in the time domain. Then we take the Fourier transform of the signal to determine the frequency component at the modulation frequency. As we have mentioned, since the lock-in amplifier acts as a very narrow bandpass filter, only the amplitude and phase of the thermal response

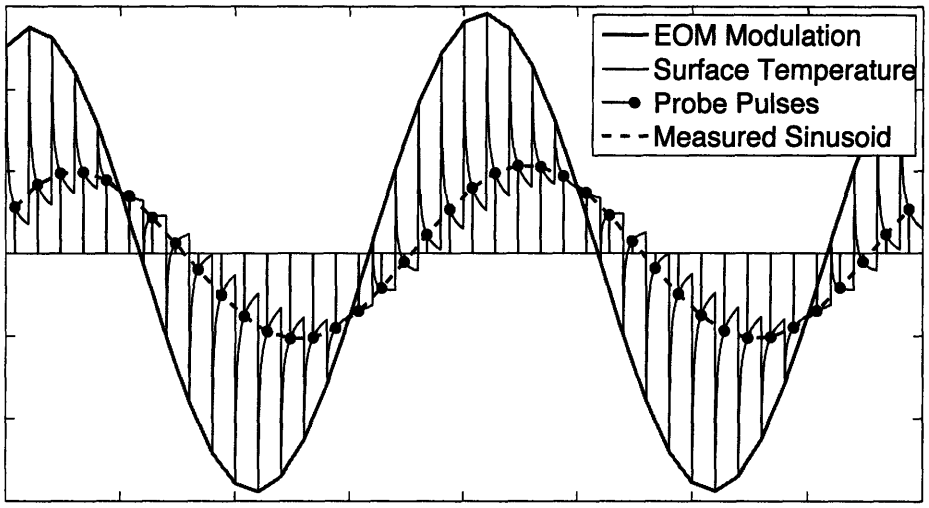

Figure 3-5: The solid line depicts the modulation envelope which serves as the reference for the lock-in amplifier. The dashed line connecting the probe pulses is the fundamental harmonic of the probe signal caused by the pump beam. Both the magnitude of this sinusoid and its phase lag from the reference frequency are measured by the lock-in at every position of the delay stage.

at this frequency will be measured.

The temperature response to an impulse of heat with strength Q, $Q\delta(t)$, is $Qh(\mathbf{r},t)$, where $\mathbf{r}$ is the spatial coordinate and t is time, and Q is the energy of the impulse. The unit impulse response, $h(\mathbf{r},t)$, has units of [temperature]/[energy]. The response to a time varying heat input $q(t)$ at the same location is given by the convolution

$$\begin{aligned}\Theta(\mathbf{r},t) &= q(t) * h(\mathbf{r},t) \\ &= \int_{-\infty}^{\infty} q(t')h(\mathbf{r},t-t')dt'\end{aligned} \tag{3.4}$$

In our case,

$$q(t) = \frac{1}{2}(1+e^{i\omega_0 t}) \sum_{m=-\infty}^{\infty} Q\delta(t-mT-T_0) \tag{3.5}$$

Here T is the time between pulses, T_0 is an arbitrary time offset between $t=0$ and the time when first pulse arrives, and Q is the energy per pulse. Since the problem obeys superposition, we can consider the periodic part and the DC part separately. The response to the DC component will not have a component at ω_0 and so will be

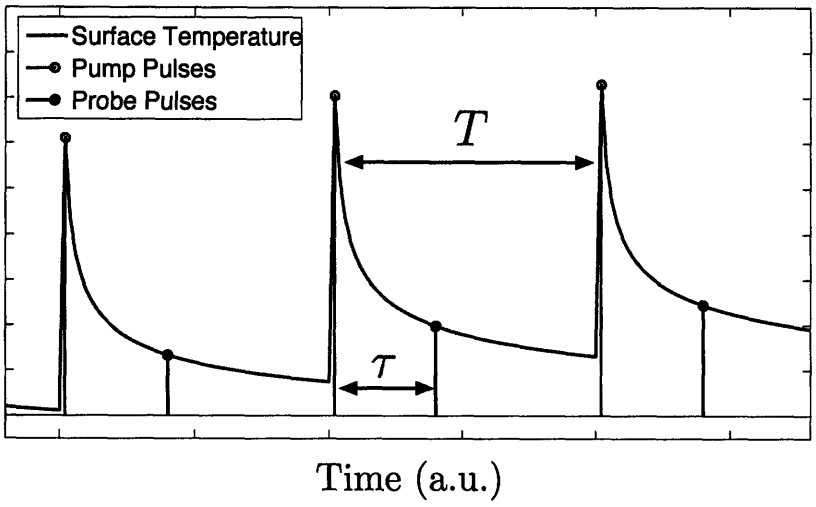

Figure 3-6: A close-up view of Fig. 3-4. The time period between pulses is T, and the delay time between the pump and probe pulses is τ.

removed by the lock-in. Therefore we need only consider the periodic heat input:

$$q(t) = e^{i\omega_0 t} \sum_{m=-\infty}^{\infty} Q\delta(t - mT - T_0) \tag{3.6}$$

This is the signal is shown in Fig. 3-2.

Inserting this heat input into Eq. (3.4) and applying the definition of convolution, we have

$$\Theta(\mathbf{r}, t) = Q \int_{-\infty}^{\infty} e^{i\omega_0 t'} \sum_{m=-\infty}^{\infty} \delta(t' - mT - T_0) h(\mathbf{r}, t - t')\, dt' \tag{3.7}$$

where $h(\mathbf{r}, t) \equiv 0$ for $t < 0$. By virtue of the property that

$$\int_{-\infty}^{\infty} f(x)\delta(x - x_0)\, dx = f(x_0) \tag{3.8}$$

the temperature of the sample is given by

$$\Theta(\mathbf{r}, t) = Q \sum_{m=-\infty}^{\infty} e^{i\omega_0(mT+T_0)} h(\mathbf{r}, t - mT - T_0) \tag{3.9}$$

The probe beam is unmodulated, and the reflectivity of the sample is assumed proportional to its surface temperature, so that the reflected probe light is described

by $\beta\Theta$ where β is a constant that includes the thermoreflectance coefficient and gain of the electronics. The probe pulses arrive at the sample at time τ after the pump pulse, where $0 \leq \tau < T$

Now, we take the Fourier transform of the probe signal and find the component at ω_0, the EOM angular modulation frequency. Mathematically, the probe signal can be represented as

$$\begin{aligned} z(t) &= \beta\Theta(t) \sum_{n=-\infty}^{\infty} Q_{\text{probe}}\delta(t - nT - T_0 - \tau) \qquad (3.10) \\ &= \left(\beta Q Q_{\text{probe}} \sum_{m=-\infty}^{\infty} e^{i\omega_0(mT+T_0)} h(t - mT - T_0)\right) \sum_{n=-\infty}^{\infty} \delta(t - nT - T_0 - \tau) \end{aligned}$$

Here Q_{probe} is the power per probe pulse, and we have dropped the spatial variable $\mathbf{r}$ in the impulse response for simplicity.

Taking the Fourier transform of Eq. (3.10),

$$\begin{aligned} \mathcal{F}\{z(t)\} = Z(\omega) &= \int_{-\infty}^{\infty} z(t) e^{-i\omega t}\, dt \qquad (3.11) \\ &= \beta Q Q_{\text{probe}} \sum_{n=-\infty}^{\infty} \sum_{m=-\infty}^{\infty} e^{i\omega_0(mT+T_0)} h(nT + T_0 + \tau - mT - T_0) e^{-i\omega(nT+T_0+\tau)} \end{aligned}$$

where $Z(\omega)$ is a complex number with both magnitude and phase. Defining the variable $q = n - m$, we have

$$Z(\omega) = \beta Q Q_{\text{probe}} \sum_{n=-\infty}^{\infty} \sum_{q=-\infty}^{\infty} e^{i\omega_0((n-q)T+T_0)} h(qT + \tau) e^{-i\omega(nT+T_0+\tau)} \qquad (3.12)$$

Rearranging,

$$\begin{aligned} Z(\omega) &= \beta Q Q_{\text{probe}} \sum_{q=-\infty}^{\infty} e^{i\omega_0(-qT+T_0)} h(qT + \tau) \sum_{n=-\infty}^{\infty} e^{i\omega_0 nT} e^{-i\omega(nT+T_0+\tau)} \qquad (3.13) \\ &= \beta Q Q_{\text{probe}} \sum_{q=-\infty}^{\infty} e^{-i\omega_0(qT+\tau)} h(qT + \tau) \underbrace{\sum_{n=-\infty}^{\infty} e^{i\omega_0(nT+T_0+\tau)} e^{-i\omega(nT+T_0+\tau)}}_{A(\omega)} \end{aligned}$$

In Appendix A.2, we show that

$$A(\omega) = e^{i(\omega_0-\omega)(T_0+\tau)}\frac{2\pi}{T}\sum_{n=-\infty}^{\infty}\delta(\omega_0-\omega+\frac{2\pi n}{T}) \tag{3.14}$$

Therefore the Fourier transform of $r(t)$ contains of a series of delta functions at frequencies $\omega = \omega_0 + 2\pi n/T$ where $n = 0, \pm 1, \pm 2, \ldots$ Since $2\pi/T$ is much typically 8–100 times greater than the EOM modulation frequency ω_0, all frequencies for $n \neq 0$ will be well outside the lock-in pass band, so to an excellent approximation the result will be:

$$Z(\omega) = \frac{\beta Q Q_{\text{probe}}}{T}\sum_{q=0}^{\infty} e^{-i\omega_0(qT+\tau)}h(qT+\tau)2\pi\delta(\omega_0-\omega) \tag{3.15}$$

We have restricted q in the sum to non-negative values since $h(t) \equiv 0$ for $t < 0$. We take the inverse Fourier transform to recover the signal in the time domain. Since the the inverse Fourier transform of the function $2\pi\delta(\omega_0 - \omega) = e^{i\omega_0 t}$, Eq. (3.15) becomes

$$z(t) = Z(\omega_0)e^{i\omega_0 t} \tag{3.16}$$

where

$$Z(\omega_0) = \frac{\beta Q Q_{\text{probe}}}{T}\sum_{q=0}^{\infty} h(qT+\tau)e^{-i\omega_0(qT+\tau)} \tag{3.17}$$

Comparing Eq. (3.16) with Eq. (3-1), we see that $Z(\omega_0)$ in Eq. (3.17) is the transfer function that we seek. It is proportional to the energy per pump pulse, Q, and the power in the probe beam, Q_{probe}/T, and gives both the magnitude and phase of the lock-in signal relative to the reference signal $e^{i\omega_0 t}$. If the impulse response decays to zero before the next pulse arrives, then the only non-zero term in Eq. (3.17) is for $q = 0$, and the solution reduces to the impulse response. However, if the response does not die away before the next pulse arrives, the results will be not be the same, as we discuss in Section 3.2.

3.1.3 Signal Analysis Using the Frequency Response

Equation (3.17) is convenient when the solution to an impulse of heat is known in the time domain, either analytically or via a numerical simulation. However, for many conduction heat transfer problems, analytical solutions are more readily obtainable in the frequency domain. Thus it is desirable to re-express Eq. 3.17 in terms of the thermal frequency response rather than the thermal impulse response. To do that, we borrow a result from signal analysis known as the sampling theorem [57]. The sampling theorem is a useful tool for understanding the frequency spectrum of a signal that is "sampled" at discrete times with a very short pulse. Given an original signal, $x(t)$, and a sampling signal $p(t)$, we can write the the sampled signal as:

$$x_p(t) = x(t)p(t) \tag{3.18}$$

where

$$p(t) = \sum_{n=-\infty}^{\infty} \delta(t - nT - T_0) \tag{3.19}$$

Here $p(t)$ is a series of unit impulses, T is the sampling period and T_0 is an arbitrary delay time. In the frequency domain, the sampling theorem tells us that

$$\begin{aligned} X_p(\omega) &= \frac{1}{T}\int_{-\infty}^{\infty} X(\theta)e^{-i(\omega-\theta)T_0} \sum_{k=-\infty}^{\infty} \delta(\omega - \theta - k\frac{2\pi}{T})\, d\theta \\ &= \frac{1}{T}\sum_{k=-\infty}^{\infty} X(\omega - k\frac{2\pi}{T})e^{-ik2\pi T_0/T} \end{aligned} \tag{3.20}$$

A more detailed derivation of the sampling theorem is given in Appendix A.3.

In our problem, we will apply the sampling theorem twice. The first time we will use it to represent the thermal response to the pump beam in the frequency domain. Then, we will apply the sampling theorem to this thermal response to find the final signal after it has been "sampled" by the probe pulses.

To begin, we take as $x(t)$ the EOM modulation. As in the impulse-response analysis, we will assume the EOM modulation is a pure sinusoid, $x(t) = e^{i\omega_0 t}$. This

has the Fourier transform $X(\omega) = 2\pi\delta(\omega - \omega_0)$. The sampling function, $p(t)$, comes from the pulsed nature of the pump beam and is mathematically treated as a series of delta functions, sampling the sinusoid $x(t)$ at a frequency $\omega_s = 2\pi/T$ where T is the time between laser pulses. For generality, we keep the arbitrary delay time T_0 between the pump pulse and the EOM reference wave. As in the impulse response solution, T_0 will eventually drop out of the final solution. Applying the sampling theorem to $X(\omega)$ gives the heat input from the pump beam in the frequency domain:

$$Q(\omega) = \frac{2\pi Q}{T} \sum_{k=-\infty}^{\infty} \delta(\omega - \omega_0 - k\omega_s) e^{-ik\omega_s T_0} \tag{3.21}$$

where again Q is the energy per pulse, T is the pulse period, ω_0 is the EOM modulation frequency, and ω_s is the "sampling frequency," $2\pi/T$.

For any linear system, the frequency response $H(\omega)$ is given by the Fourier transform of the impulse response, $h(t)$ [57]:

$$\mathcal{F}\{h(t)\} = \int_{-\infty}^{\infty} h(t) e^{-i\omega t}\, dt = H(\omega) \tag{3.22}$$

The thermal response at the surface, $\Theta(t)$, is the convolution of the impulse response $h(t)$ and $q(t)$. In the frequency domain, convolution becomes multiplication:

$$\Theta(\omega) = H(\omega)Q(\omega) = \frac{2\pi Q}{T} \sum_{k=-\infty}^{\infty} H(\omega)\delta(\omega - \omega_0 - k\omega_s) e^{-ik\omega_s T_0} \tag{3.23}$$

The probe beam samples the surface temperature with pulses at $\omega_s = 2\pi/T$ and strength Q_{probe}, delayed from the pump pulses by time τ. Now we apply the sampling theorem to the surface temperature, Eq. (3.23), to find the frequency domain representation of the reflected probe signal:

$$\begin{aligned} Z(\omega) &= \frac{2\pi\beta Q Q_{\text{probe}}}{T} \sum_{l=-\infty}^{\infty} \Theta(\omega - l\omega_s) e^{-il\omega_s(T_0+\tau)} e^{-ik\omega_s T_0} \qquad (3.24) \\ &= \frac{2\pi\beta Q Q_{\text{probe}}}{T^2} \sum_{l=-\infty}^{\infty} \sum_{k=-\infty}^{\infty} H(\omega - l\omega_s)\delta(\omega - \omega_0 - (k+l)\omega_s) e^{-il\omega_s\tau} e^{-i(k+l)\omega_s T_0} \end{aligned}$$

The delta function evaluates to zero at all frequencies except $\omega = \omega_0 + (k + l)\omega_s$ where k and l are integers. As in the previous section, since ω_s is typically 8–100 times greater than the EOM modulation frequency ω_0, the only frequency inside the lock-in pass band will be $\omega = \omega_0$. Inserting $\omega = \omega_0$ into Eq. (3.24), we see that the delta function eliminates all the terms except those where $l = -k$. Thus we can replace l with $-k$ and eliminate one of the sums:

$$Z(\omega) = \frac{2\pi\beta Q Q_{\text{probe}}}{T^2} \sum_{k=-\infty}^{\infty} H(\omega_0 + k\omega_s) e^{ik\omega_s \tau} \delta(\omega - \omega_0) \tag{3.25}$$

As we did in the impulse-response analysis, we take the inverse Fourier transform so that Eq. (3.25) becomes

$$z(t) = Z(\omega_0) e^{i\omega_0 t} \tag{3.26}$$

where now

$$Z(\omega_0) = \frac{\beta Q Q_{\text{probe}}}{T^2} \sum_{k=-\infty}^{\infty} H(\omega_0 + k\omega_s) e^{ik\omega_s \tau} \tag{3.27}$$

Equation (3.27) is the frequency-response equivalent of Eq.(3.17). In the limit that $T \to \infty$ (the pulses become far apart), Eq. (3.27) reduces to the inverse Fourier transform of $H(\omega)$, i.e. the impulse response $h(t)$, as it should. Equations (3.17) and (3.27) are mathematically equivalent; this is shown in Appendix A.4.

Components of the Lock-In Amplifier Signal

The lock-in amplifier actually mixes the signal with two reference waves that are 90° out of phase; this allows it to extract both the magnitude and phase of the measured signal, relative to the reference wave. The instrument returns two readings, an in-phase component, X, which is composed of the cosine components of the signal, and an out-of-phase (or "quadrature") component, Y, which is composed of the sine components. From this, the magnitude, R, is obtained from $\sqrt{X^2 + Y^2}$ and the phase ϕ from $\tan^{-1}(Y/X)$.

As we discuss later, the out-of-phase component is useful for correcting for any phase offset introduced into the signal via the electronics. The in-phase and out-of-

phase components X and Y are given by the real and imaginary parts of Eq. 3.27:

$$X = \mathrm{Re}\{Z(\omega_0)\} \tag{3.28}$$

$$Y = \mathrm{Im}\{Z(\omega_0)\} \tag{3.29}$$

A proof of this is given in Appendix A.5.

3.2 Accumulation Effects

In the beginning of Section 3.1, we alluded to the fact that the accumulation of multiple laser pulses is an important effect that must be accounted for in our pump-probe experiment. In addition, while it complicated the analysis of the preceding section, the resulting two expressions, Eq. (3.17) and Eq. (3.27), are more powerful than the either the impulse response or the frequency response of the sample alone. This is because the response to an impulse of heat is characterized by one time scale and the response to a modulated thermal wave is characterized by another, and we can potentially probe both simultaneously. In this section we examine the accumulation effects in detail, showing when and how they must be considered.

As we show in Appendix A.4, Eq. (3.17) and Eq. (3.27) are mathematically equivalent, and we can use either form to illustrate accumulation effects. In the limit that the time between pulses, T, becomes infinite, both expressions reduce to the impulse response as a function of delay time, τ:

$$\lim_{T\to\infty} \frac{\beta Q Q_{\mathrm{probe}}}{T} \sum_{q=0}^{\infty} e^{-i\omega_0\tau} h(qT+\tau) = \frac{\beta Q Q_{\mathrm{probe}}}{T} h(\tau) e^{-i\omega_0\tau} \tag{3.30}$$

This is easily seen from the fact that at very long times, $h(qT+\tau)$ dies to zero for all terms where $q \neq 0$. In this limiting case, the phase shift is simply the delay between the pump and probe pulses divided by the modulation frequency, as expected. The signal is proportional to the energy per pump pulse, Q, and the power in the probe beam, Q_{probe}/T. In the other limit, as T approaches zero, the expression approaches

the definition of the Fourier transform of $h(\tau)$ since τ is defined to be less than T :

$$\lim_{T\to 0} \frac{\beta Q Q_{\text{probe}}}{T^2} \sum_{q=0}^{\infty} e^{-i\omega_0 \tau} h(qT+\tau)T = \frac{\beta Q Q_{\text{probe}}}{T^2} H(\omega_0) \tag{3.31}$$

We could arrive at the same result by noting that in Eq. (3.27), $H(\omega_0 + k\omega_s)$ is the Fourier transform of a real function and must converge, so as ω_s approaches infinity (T approaches zero), all terms except $k = 0$ vanish.

In the intermediate range, where the decay time of the system is not much longer or shorter than the pulse time, T, the signal has elements of both the impulse response and the steady frequency response, and the two effects cannot be simply separated. The majority of thermal conductivity measurements fall into this category. To examine this further, we take a simple exponential system as a model and see how the measured signal changes as the decay rate or laser pulse period are varied. Although the thermal response of the sample is more complex, the basic features of the accumulation effects will be the same.

3.2.1 Example of Accumulation with a Model System

The impulse response and frequency response of our model system are given by:

$$h(t) = e^{-at} \tag{3.32}$$

$$H(\omega) = \frac{1}{a + i\omega} \tag{3.33}$$

Figure 3-7 shows the signal returned by the lock-in, Eq. (3.27) assuming an exponential decay time, $a^{-1} = 10$ ns, for three different pulse periods: 100 ns (essentially the single pulse response), 15 ns and 12 ns. The most obvious effect as the decay time approaches the pulse period is that the baseline signal at zero delay is no longer zero. If one were unaware of the the accumulation effects and subtracted off the zero-delay signal before normalizing, the results would be that signals with more accumulation effects would appear to decay faster than the single-pulse response. This is shown in Fig. 3-8.

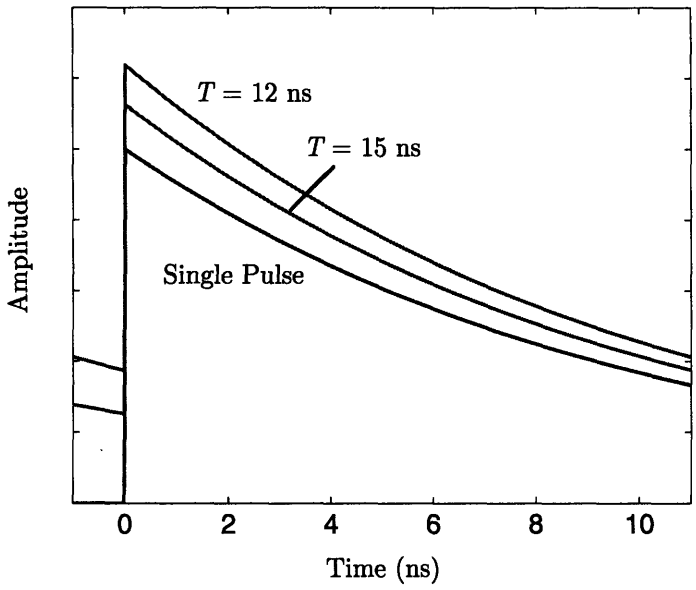

Figure 3-7: The signal returned by the lock-in, Eq. (3.27) assuming an exponential decay time, $a^{-1} = 10$ ns, for three different pulse periods: 100 ns (essentially the single pulse response), 15 ns and 12 ns.

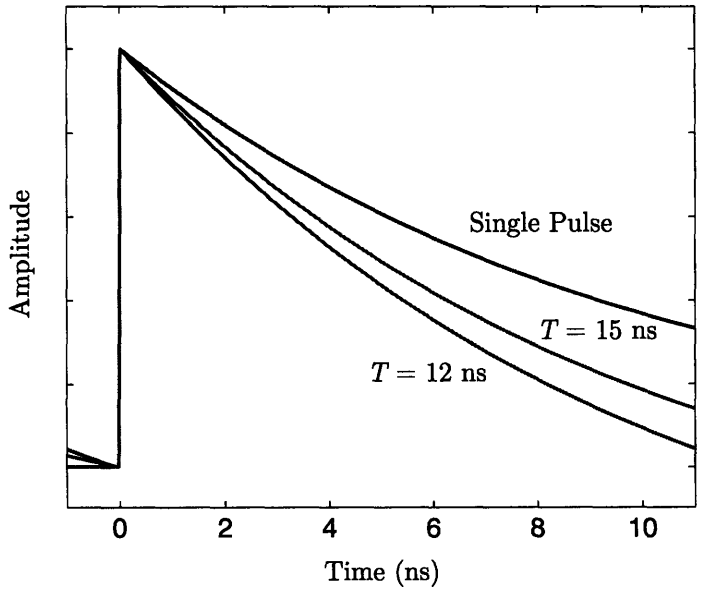

Figure 3-8: The signal returned by the lock-in, Eq. (3.27) assuming an exponential decay time, $a^{-1} = 10$ ns, after subtraction of the baseline signal and normalization.

Now we explore the result of Eq. (3.31). Figure 3-9 shows visually how the lock-in signal approaches the frequency response, $H(\omega_0)$, as the exponential decay time approaches the pulse period. In this case, we have fixed the laser pulse time, T, at 12.5 ns and varied the exponential decay time a^{-1} from 5 ns to 100 ns. As the decay time becomes long compared to the pulse period, the lock-in signal approaches $H(\omega_0)$, where in this case we have chosen $\omega_0 = 2\pi \times 10$ MHz.

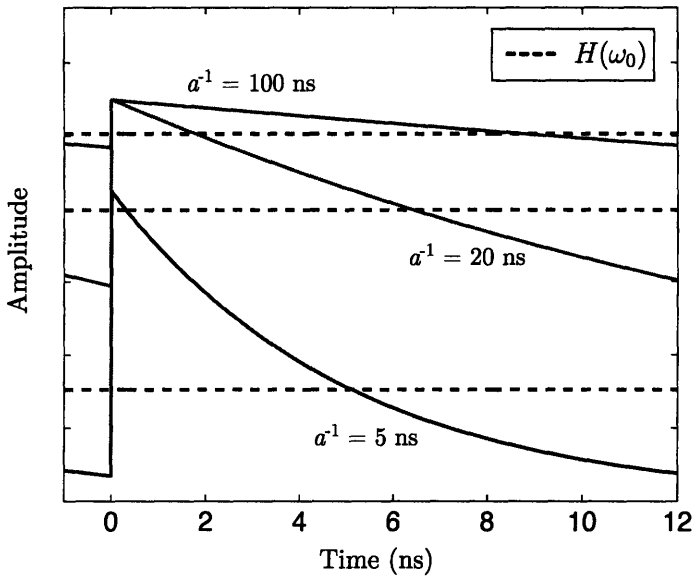

Figure 3-9: The lock-in signal approaches the frequency response, $H(\omega_0)$, as the exponential decay time approaches the pulse period. In this case, we have fixed T at 12.5 ns and varied the exponential decay time a^{-1} from 5 ns to 100 ns. As the decay time becomes long compared to the pulse period, the lock-in signal approaches $H(\omega_0)$

3.2.2 Tests for Accumulation

It is clear that if accumulation effects are present they should be accounted for. There are two simple ways to test for their presence experimentally. The first is simply observing if there is a measured signal just before the delay time crosses $\tau = 0$. After blocking the pump and canceling any probe noise and coherent RF pickup, unblocking the pump beam when τ is just before zero will produce a non-zero signal if accumulation is present.

Another way to test for accumulation is to vary the modulation frequency, ω_0, and

see if the signal changes. When there are no accumulation effects, the amplitude of the signal is unaffected by the modulation frequency: ω_0 only appears in Eq. (3.30) in the phase factor. Figure 3-10 shows the lock-in signal for three different exponential decay times at two modulation frequencies, 10 MHz and 1 MHz. The pulse period in this example is 12.5 ns. When the exponential decay time, a^{-1} is short compared to T there is no change at different frequencies. As the decay time approaches T and accumulation becomes more important, the change at different frequencies becomes more pronounced.

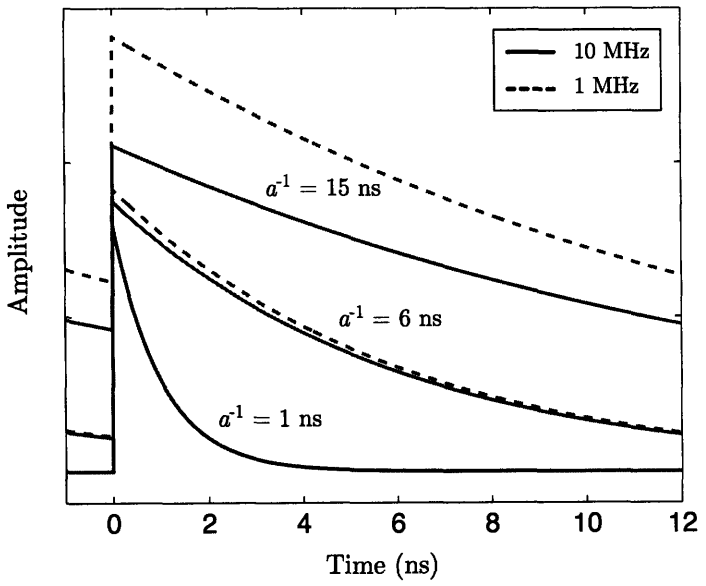

Figure 3-10: The lock-in signal for three different exponential decay times at two modulation frequencies, 10 MHz and 1 MHz. The pulse period in this example is 12.5 ns. As the decay time, a^{-1}, approaches T and accumulation becomes more important, the change at different frequencies becomes more pronounced.

3.2.3 Convergence of the Impulse-Response Solution

Analytical solutions to heat diffusion problems are often simpler to obtain in the frequency domain, and in this case Eq. (3.27) is more convenient. However, if the problem is more complex, for example the behavior of a non-equilibrium model or the Boltzmann Transport Equation, then it is more convenient to obtain the impulse response, $h(t)$, numerically. In this case, Eq. (3.17) is more useful. Since simulation

time can be costly, it is useful to know how many terms of the sum in Eq. (3.17) should be included.

In Fig. 3-11, we show the behavior of a system with a decay time $a^{-1} = 10$ ns, and a pulse period $T = 12$ ns. The solution converges rapidly and after ten terms there is no further change in the signal. In this case, the $h(t)$ should be calculated to $t = \tau + 10T$, or 137.5 ns at maximum delay time. For systems that decay more slowly, more terms in the sum would be needed.

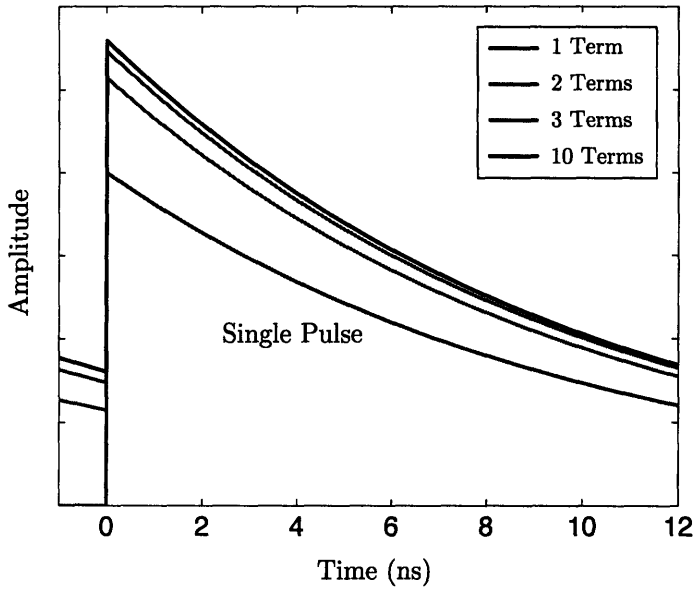

Figure 3-11: The behavior of a system with a decay time $a^{-1} = 10$ ns, and a pulse period $T = 12$ ns. The solution converges rapidly and after ten terms there is no further change in the signal.

3.3 Heat Transfer Analysis

Equations (3.17) and (3.27) are general expressions for the signal returned by the lock-in amplifier, expressed in terms of the sample impulse response, $h(t)$, and frequency response, $H(\omega)$, respectively. The two are a Fourier transform pair, as shown in Eq. (3.22). In Section 3.2, we examined the accumulation of multiple pulses using a simple exponential decay model to illustrate some basic features of the solution. Now, it is time to solve for the true thermal response of the sample. This is most

conveniently done in the frequency domain.

3.3.1 One Dimensional Heat Transfer in Layered Structures

There have been several publications on thermal conduction through layered structures in one dimensional and in isotropic media [58–60]. Here we adopt the approach described in *Conduction of Heat in Solids* by Carslaw and Jaegar [58] for one-dimensional conduction and then extend it to account for radial, anisotropic effects using a Hankel transformation. Figure 3-12 illustrates the problem for a single layer with heat flow in the z direction. In the frequency domain, thermal response of the sample, $H(\omega)$, can be found by relating the temperature θ_t, and heat flux, f_t, on the top side of the slab to the temperature, θ_b, and heat flux, f_b on the bottom side through:

$$\begin{bmatrix} \theta_b \\ f_b \end{bmatrix} = \begin{bmatrix} \cosh(qd) & \frac{-1}{\sigma_z q}\sinh(qd) \\ -\sigma_z q \sinh(qd) & \cosh(qd) \end{bmatrix} \begin{bmatrix} \theta_t \\ f_t \end{bmatrix} \tag{3.34}$$

Here d is the layer thickness, σ_z the cross-plane thermal conductivity, and $q^2 = i\omega/\alpha$ where α is the thermal diffusivity.

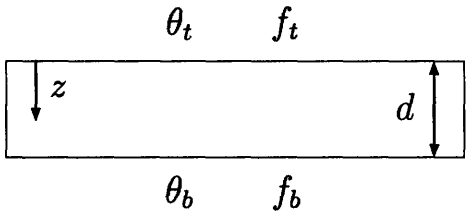

Figure 3-12: Conduction through a one-dimensional slab. The temperature and heat flux on the top surface, θ_t and f_t, can be related to the temperature and heat flux at the bottom surface, θ_b and f_b, through a matrix equation.

The case of unidirectional heat flow through multiple layers is illustrated in Fig. 3-13. Mathematically, multiple layers are handled by multiplying the matrices for individual layers together:

$$\begin{bmatrix} \theta_b \\ f_b \end{bmatrix} = \mathbf{M}_n \mathbf{M}_{n-1} \cdots \mathbf{M}_1 = \begin{bmatrix} A & B \\ C & D \end{bmatrix} \begin{bmatrix} \theta_t \\ f_t \end{bmatrix} \tag{3.35}$$

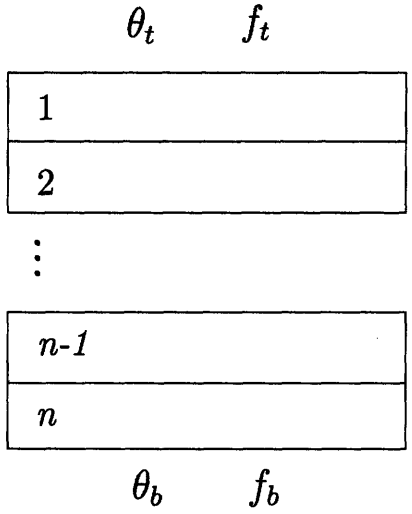

Figure 3-13: Conduction through multiple layers.

where $\mathbf{M}_n$ is the matrix for the bottom layer. Each matrix contains the thickness and thermal properties of one layer of material. If the bottom surface of the nth layer is assumed to be adiabatic, or if the nth layer is treated as semi-infinite, then in both cases Eq. (3.35) reduces to $C\theta_t + Df_t = 0$ and the surface temperature will be given by:

$$\theta_t = \frac{-D}{C} f_t \tag{3.36}$$

where f_t is the heat flux boundary condition applied to the top surface. In the majority of our experiments the semi-infinite boundary condition is an accurate description of the physical situation.

Thermal Interface Conductance

As we discussed in Section 1.2.2, thermal interface conductance between material layers can arise from fundamental sources such as acoustic and electronic impedance and from other factors such as the interface quality or contamination. The interface conductance G is defined by

$$f = G(\theta_1 - \theta_2) \tag{3.37}$$

where f is the heat flux across the interface and θ_1 and θ_2 are temperatures on either side. In matrix form, this becomes

$$\begin{bmatrix} \theta_2 \\ f \end{bmatrix} = \begin{bmatrix} 1 & G^{-1} \\ 0 & 1 \end{bmatrix} \begin{bmatrix} \theta_1 \\ f \end{bmatrix} \tag{3.38}$$

Thus interface conductances are easily incorporated into Eq. (3.35). Equation (3.38) can also be obtained from Eq. (3.34) by taking the limit as the heat capacity goes to zero and choosing σ_z and d such that $G = \sigma_z/d$.

3.3.2 Extension to Radial Conduction

As we discussed in Section 3.2, if the response from a single laser pulse dies away completely before the next pulse arrives, the measured signal is the impulse response of the sample, and transport is essentially one-dimensional. The thermal penetration depth $L = \sqrt{\alpha t}$ will be between 30 nm and 300 nm for almost all materials, assuming a decay time of 10 ns. Compared to the spot diameter of 10–100 μm, the penetration depth is small and radial effects can be ignored. However, when the pulses do not fully die away, accumulation effects enter into the measured response, Eq. (3.27), and the system begins to acquire some properties of the frequency response at the modulation frequency, $H(\omega_0)$. In this case, a better choice is the thermal penetration depth of the thermal waves induced by the modulation: $L = \sqrt{2\pi\alpha/\omega_0}$, where ω_0 is the modulation frequency. This depth can range from roughly 200 nm to 2 μm at 10 MHz modulation, and from 700 nm to 7 μm at 1 MHz modulation. If these lengths are not negligible compared to the spot dimension, radial heat conduction effects should be accounted for. In our system, with a pulse frequency of 80 MHz, the thermal response does not fully die away for the majority of samples, and so an analysis of radial conduction is necessary.

Equation (3.36) can be extended include the effects of radial conduction caused by finite laser spot sizes. The Gaussian laser spots have cylindrical symmetry, so a zero-order Hankel transform can be used to simplify the equations. The Hankel

transform of $\theta(r)$ is given by [61]:

$$\overline{\theta_r} \equiv \mathcal{H}_0\{\theta(r)\} = \int_0^\infty r J_0(kr)\theta(r)\, dr \tag{3.39}$$

where k is the transform variable, r is the radial coordinate and J_0 is the zero zero-order Bessel function of the first kind.

In cylindrical coordinates, the heat equation is:

$$\frac{\sigma_r}{r}\frac{\partial}{\partial r}\left(r\frac{\partial\theta}{\partial r}\right) + \sigma_z\frac{\partial^2\theta}{\partial z^2} = \rho c\frac{\partial\theta}{\partial t} \tag{3.40}$$

where σ_r and σ_z are the radial and cross-plane thermal conductivities, respectively, ρ is the density, and c_p is the specific heat.

Taking the Hankel transform of Eq. (3.40) yields

$$-\sigma_r k^2\overline{\theta} + \sigma_z\frac{\partial^2\overline{\theta}}{\partial z^2} = \rho c\frac{\partial\overline{\theta}}{\partial t} \tag{3.41}$$

Applying a Fourier transform Eq. (3.41) gives

$$-\sigma_r k^2\overline{\theta}(\omega) + \sigma_z\frac{\partial^2\overline{\theta}(\omega)}{\partial z^2} = \rho c i\omega\overline{\theta}(\omega) \tag{3.42}$$

This can be rearranged as

$$\frac{\partial^2\overline{\theta}(\omega)}{\partial z^2} = q^2\overline{\theta}(\omega) \tag{3.43}$$

where

$$q^2 \equiv \frac{\sigma_r k^2 + \rho c i\omega}{\sigma_z} \tag{3.44}$$

Equation (3.43) is identical to the one-dimensional heat equation in the frequency domain, except that q^2 is now given by Eq. (3.44) instead of $q^2 = i\omega/\alpha$. Thus all of the results obtained in Section 3.3.1 are valid, except the definition of q must be replaced with that given by Eq. (3.44).

The top surface boundary condition is now given by the radial heat flux distribu-

tion at the top surface due to the pump beam:

$$I(r) = \frac{2A_0}{\pi w_0^2} \exp\left(\frac{-2r^2}{w_0^2}\right) \tag{3.45}$$

where A_0 is the power absorbed and w_0 is the $1/e^2$ beam waist. Taking the Hankel transform of this gives

$$I(k) = \frac{A_0}{2\pi} \exp\left(\frac{-k^2 w_0^2}{8}\right) \tag{3.46}$$

Inserting this result into Eq. (3.36) yields the surface temperature, still in the spatial transform domain:

$$\theta_t(k) = \left(\frac{-D}{C}\right) \frac{A_0}{2\pi} \exp\left(\frac{-k^2 w_0^2}{8}\right) \tag{3.47}$$

where C and D are the matrix elements from Eq. (3.35). Taking the inverse Hankel transform gives $\theta(r)$, we get the surface temperature in real space:

$$\theta(r) = \int_0^\infty k J_0(kr) \left(\frac{-D}{C}\right) \left(\frac{A_0}{2\pi}\right) \exp\left(\frac{-k^2 w_0^2}{8}\right) dk \tag{3.48}$$

The final thermal response of the system, $H(\omega)$ in Eq. (3.27), is given by the weighted average of Eq. (3.48) by the co-axial probe beam with radius w_1:

$$H(\omega) = \int_0^\infty \left(\frac{2}{\pi w_1^2}\right) \exp\left(\frac{-2r^2}{w_1^2}\right) 2\pi r\, dr \int_0^\infty k J_0(kr) \left(\frac{-D}{C}\right) \left(\frac{A_0}{2\pi}\right) \exp\left(\frac{-k^2 w_0^2}{8}\right) dk \tag{3.49}$$

Rearranging and using Eqs. (3.45) and (3.46) collapses this into a single integral, which is solved numerically:

$$H(\omega) = \frac{A_0}{2\pi} \int_0^\infty k \left(\frac{-D}{C}\right) \exp\left(\frac{-k^2(w_0^2 + w_1^2)}{8}\right) dk \tag{3.50}$$

Offset Beam Spots

The situation where the spots are not co-axial is illustrated in Fig. 3-14. In this case, some of the symmetry is lost and instead of one integral to obtain $H(\omega)$, we need

three:

$$H(\omega) = \left(\frac{2}{\pi w_1^2}\right) \int_{-\infty}^{\infty} \int_{0}^{\infty} \theta\left(\sqrt{(x-x_0)^2+y^2}\right) \exp\left(\frac{-2(x^2+y^2)}{w_1^2}\right) dy\, dx \quad (3.51)$$

where $\theta\left(\sqrt{(x-x_0)^2+y^2}\right)$ is given by the integral shown in Eq. (3.48). While Eq. (3.51) is not as convenient to evaluate as Eq. (3.50), it is still tractable numerically.

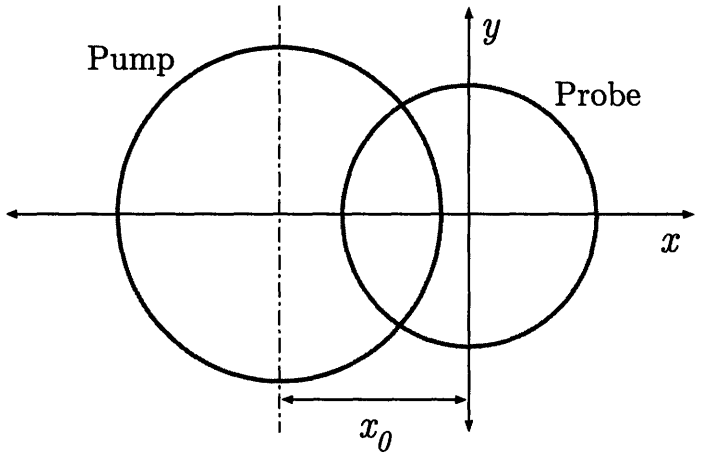

Figure 3-14: The pump and probe spots, with centers separated by a distance x_0.

3.4 Post Processing

3.4.1 Fitting Variables

The basic procedure for obtaining one or more physical properties of interest from the experiment is simple: adjust the properties until the model and the data match. We use a multi-dimensional least squares minimization routine to match the output of the lock-in amplifier to Eq. (3.27) Because the lock-in provides both amplitude and phase information, we have a choice of which observable to use to minimize the error. For example, we could use the in-phase component, X, the amplitude, R, the ratio of the in-phase to out-of-phase components, X/Y [20], or the signal phase, $\phi = \tan^{-1}(Y/X)$.

Although the amplitude seems the obvious choice, it presents two problems. The first is the issue of normalization. Since the gain of the electronics, properties of the detector photodiode, and thermoreflectance coefficient all influence the magnitude of the voltage returned by the lock-in, fitting to the absolute amplitude of either X, Y, or R is not practical. Instead, we normalize the data to the value at a specific time when the diffusion regime is valid, for example $t \geq 200$ ps. When the data is noisy, normalization is difficult because of random variations around the normalizing time and care must be taken to appropriately smooth the data. The other difficulty with fitting to the amplitude is the fact that, for low thermal conductivity materials, the Y component of the signal can be large compared to X, and also relatively constant over the delay times of the experiment. The result is that the amplitude, R, is often noisier than the in-phase component, X.

To overcome both of these problems, we fit the phase data instead. Because the phase involves the ratio of the two components, the absolute magnitudes cancel out and normalization is unnecessary. In addition, noise due to fluctuations in laser power are present in both X and Y and so will also cancel out, usually leaving a cleaner signal [20]. Figure 3-15 shows the amplitude and phase data from a sample of Al on SiO_2, with a modulation frequency of 9.1 MHz. The amplitude data, while fairly clean, is visibly noisier than the phase data, and at lower modulation frequencies where laser noise is larger, the difference becomes more pronounced.

3.4.2 Determining the Phase Offset

Fitting to the phase has an additional benefit. When there are accumulation effects, the phase baseline just before zero delay time is sensitive to the thermal properties of the substrate, and so fitting the phase is more sensitive than fitting the shape of the curve alone.

However, this introduces one difficulty: determining the true phase of the reference modulation to which the signal is being compared. Ideally, the reference modulation would be exactly in phase with the modulation signal supplied to the EOM. However, the signal cables, photodiode, inductive resonator, and lock-in amplifier all have their

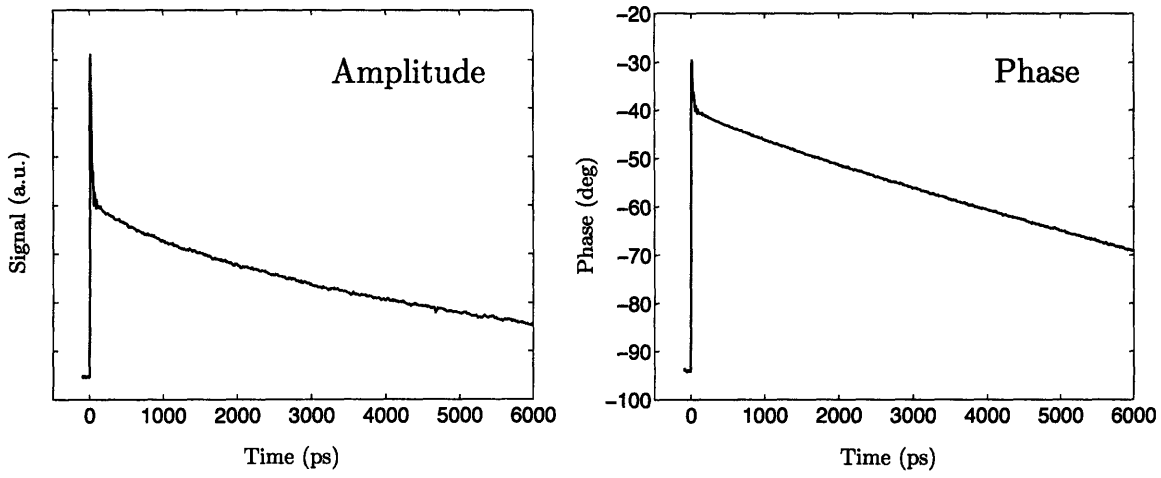

Figure 3-15: Amplitude and phase data from a sample of Al on SiO_2, with a modulation frequency of 9.1 MHz

own response, which collectively we can write as the transfer function Z_{inst}, such that for a given input $\exp(i\omega t)$ the output will be given by

$$A_{\text{inst}} \exp(i\omega t + \phi_{\text{instr}}) = Z_{\text{inst}} \exp(i\omega t) \tag{3.52}$$

where ϕ_{inst} is the phase delay introduced by the instrumentation. Thus to fit the phase data, we need a way to determine ϕ_{inst} and subtract it from the signal phase.

One way would be to "normalize" the phase data by subtracting off the phase at delay time $\tau = 0 - \epsilon$, where ϵ is a small quantity, from both the measured and calculated response. While simple, this approach throws away the absolute phase information which, as we mentioned above, can provide additional sensitivity to thermal properties. Another way would be to split off some of the pump beam and measure its phase directly. This sounds attractive, but there is a subtle problem. The phase delay of the inductive resonator is a function of the junction capacitance, C_J, of the photodiode, as determined by Eq. (2.5). The junction capacitance depends on the width of the depletion region in the PIN diode, which in turn depends on the intensity of light incident on the diode and also the applied reverse bias. Since each sample may have a different reflectivity, and since the probe is a different color and intensity than a split off pump beam, C_J will vary and the measured value of ϕ_{inst} will not

be accurate. In practice, we find this difference to be on the order of 1–2 degrees, enough to change the measured value of thermal conductivity by 5–10% .

Instead, we cancel the instrumentation phase by using the fact that the out-of-phase component of the signal, Y, should be constant as the delay time crosses $\tau = 0$ [19]. As shown in Eq. (3.29), Y is given by the imaginary part of Eq. (3.27). Figure 3-16 illustrates the point graphically by showing the imaginary part of Eq. (3.27) calculated for a typical sample, and the same signal calculated after an artificial phase shift of $\pm 1°$ has been introduced.

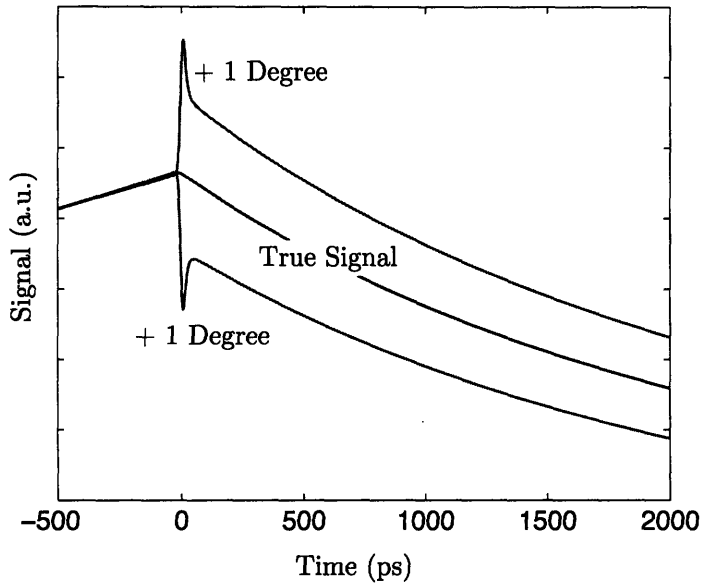

Figure 3-16: The imaginary part of Eq. (3.27) as the delay time crosses zero should be constant. A phase shift introduced by the instrumentation will cause Y signal to "jump."

After the data is collected, the change in the Y signal, ΔY_0, and the change in the X signal, ΔX_0, are measured as the delay time crosses $t = 0$, and the phase introduced by the instrumentation is computed from $\Delta\phi = \tan^{-1}(\Delta Y_0/\Delta X_0)$ Then, the measured X and Y signals are corrected by rotating the signal in the complex plain [20]:

$$\begin{aligned} X_{\text{fixed}} &= X\cos(\Delta\phi) - Y\sin(\Delta\phi) \\ Y_{\text{fixed}} &= Y\cos(\Delta\phi) + X\sin(\Delta\phi) \end{aligned} \tag{3.53}$$

The phase correction routine is performed automatically with a MATLAB script. Figure 3-17 shows a typical out-of-phase signal before and after the instrumentation phase has been cancelled via Eq. (3.53).

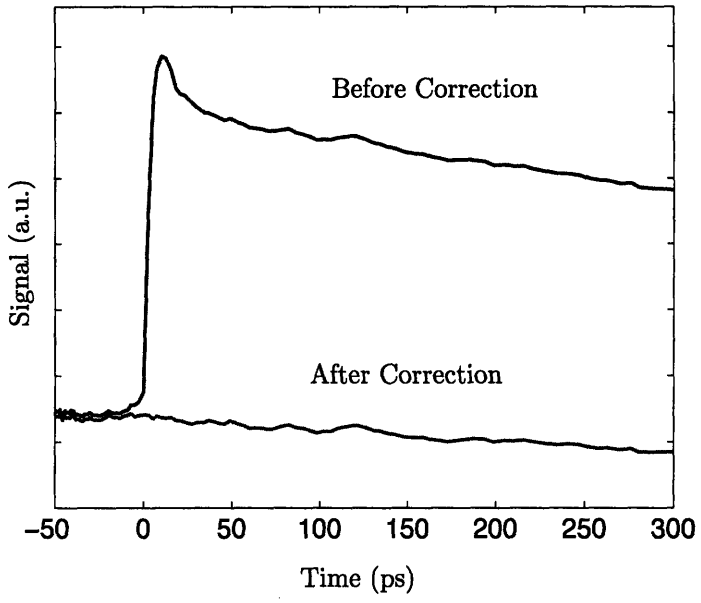

Figure 3-17: The out-of-phase signal before and after the instrumentation phase has been cancelled. The signal appears somewhat noisy because in this case the phase shift was small, so the bounds on the signal axis are tight.

3.5 Sensitivity Analysis

With any experimental technique, it is important to quantify the sensitivity of the method to the parameters of interest. As we discussed in Section 3.4.1, we can fit our data to the signal amplitude, R, or phase, ϕ, and so here we look at the sensitivity of both of these quantities to different properties of the system. We will define the sensitivities to a parameter x in a manner similar to that of Gundrum et. al. [22]:

$$S_{R,x} = \frac{d\ln R}{d\ln x} \tag{3.54}$$

$$S_{\phi,x} = \frac{d\phi}{d\ln x} \tag{3.55}$$

We use the logarithmic derivative for a sensitivity analysis because it normalizes the absolute magnitudes of the quantities being studied, since $d\ln x = d\ln x/x$.

A typical thermal conductivity measurement involves two fitting parameters: the thermal conductivity of the substrate, and the thermal interface conductance between the Al layer and the substrate. In Fig. 3-18, we plot the amplitude sensitivity, S_R, for both of the parameters for two different substrates: SiO_2, with a thermal conductivity of 1.38 W/mK, and Si, with a thermal conductivity of 140 W/mK, as a function of the stage delay time. All sensitivity calculations in this thesis are done using typical best-fit values of the thermal interface conductances. For Si and SiO_2, the thermal interface conductances were taken as 100 MW/m^2K and 150 MW/m^2K, respectively. The modulation frequency is 10 MHz.

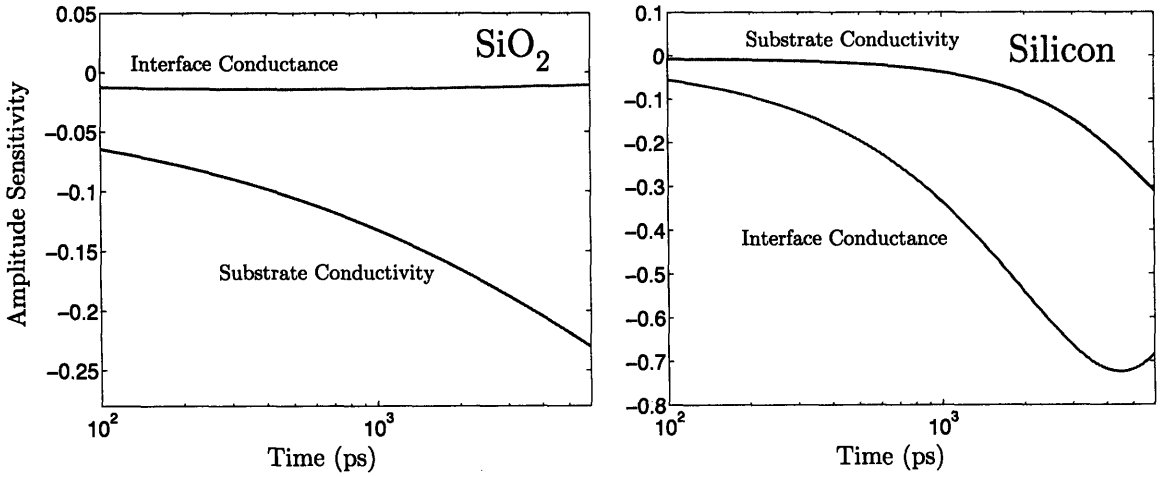

Figure 3-18: The amplitude sensitivity, S_R to thermal conductivity and thermal interface conductance for two different substrates: SiO_2, with a thermal conductivity of 1.38 W/mK, and Si, with a thermal conductivity of 140 W/mK, as a function of delay time for a modulation frequency of 10 MHz.

There are two notable features in Fig. 3-18. First, in SiO_2, a low thermal conductivity material, the sensitivity to the thermal interface conductance is much smaller than the sensitivity in Si, a high thermal conductivity material. The other main feature, present in both materials, is that the sensitivity to thermal conductivity increases at longer delay times. This makes physical sense, since at the long-time response is dominated by thermal diffusion into the substrate.

As we discussed in Section 3.4.1, we often find it more convenient to fit to the phase of the lock-in signal. Figure 3-19 plots the phase sensitivity S_ϕ for the same parameters described in Fig. 3-18. As with the amplitude sensitivity, phase sensitivity to the interface is small in SiO_2 and large in Si. The dependence of the sensitivity on delay time is not as simply interpreted, since the phase data is more strongly affected by accumulation effects which shift the initial value of the signal phase.

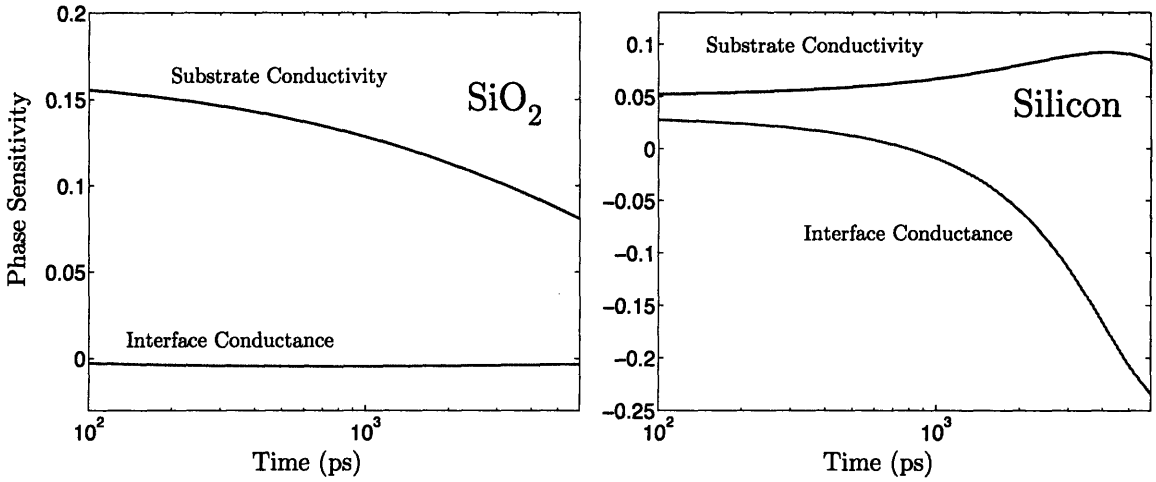

Figure 3-19: The phase sensitivity, S_ϕ to thermal conductivity and thermal interface conductance for two different substrates: SiO_2 and Si, as a function of delay time.

Another way of illustrating sensitivity is to plot the best fit curve along with the experimental data, and then vary the parameter of interest by a certain percentage and see how the solution changes. Figure 3-20 shows the best fit curves for phase and amplitude data from 2 μm of thermal SiO_2. Solutions obtained by varying the SiO_2 thermal conductivity in the model by $\pm 20\%$ are also shown, giving a visual picture of the sensitivity to that parameter.

3.6 Sample Results

In this section we present some sample measurements from some common materials as a verification of the analysis laid out in the preceding sections. All results in this section were taken with a pump $1/e^2$ radius of 25 μm, a probe $1/e^2$ radius of

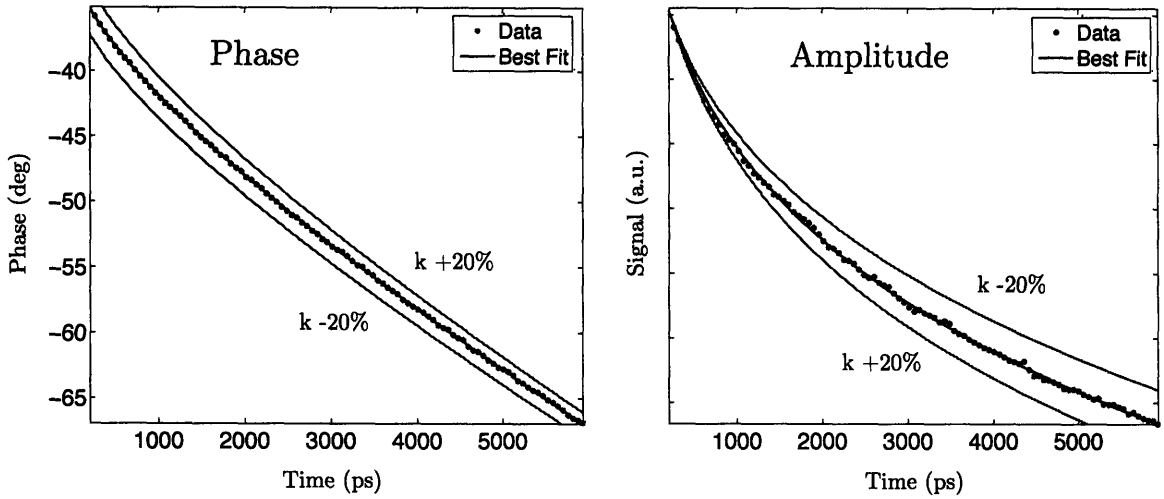

Figure 3-20: Best fit curves for phase and amplitude data from 2 μm of thermal SiO_2, and solutions obtained by the thermal conductivity in the model by $\pm 20\%$.

4 μm, and a modulation frequency of 9.1 MHz. In Fig. 3-21, we show some typical experimental data, taken from a piece sapphire coated with 75 nm of Al. The phase data was used to fit both the thermal conductivity and thermal interface conductance, and the resulting values were used to generate the curves for the other components of the signal: amplitude, in-phase and out-of-phase data. In this case, the measured thermal conductivity 39.6 W/mK, and the interface conductance was 78 MW/m^{2}K, in good agreement with literature values [16, 62].

In Fig. 3-22, we show phase data and best fit values for four materials with thermal conductivities spanning two orders of magnitude. All thermal conductivity values are within 3% of accepted values [63]. Values for the thermal interface conductance were on the order of 100–200 MW/m^{2}K. Since these values are extremely sensitive to interface quality and sample coating, it is difficult to compare with existing measurements. They are, however, of the same order of magnitude as previously reported values [16, 20]. Figure 3-23 shows the amplitude data and fit for the same samples.

3.6.1 The Impact of the Interface

As we discussed in the previous section, extracting thermal conductivity from the pump-probe measurement typically requires two fitting parameters: the thermal con-

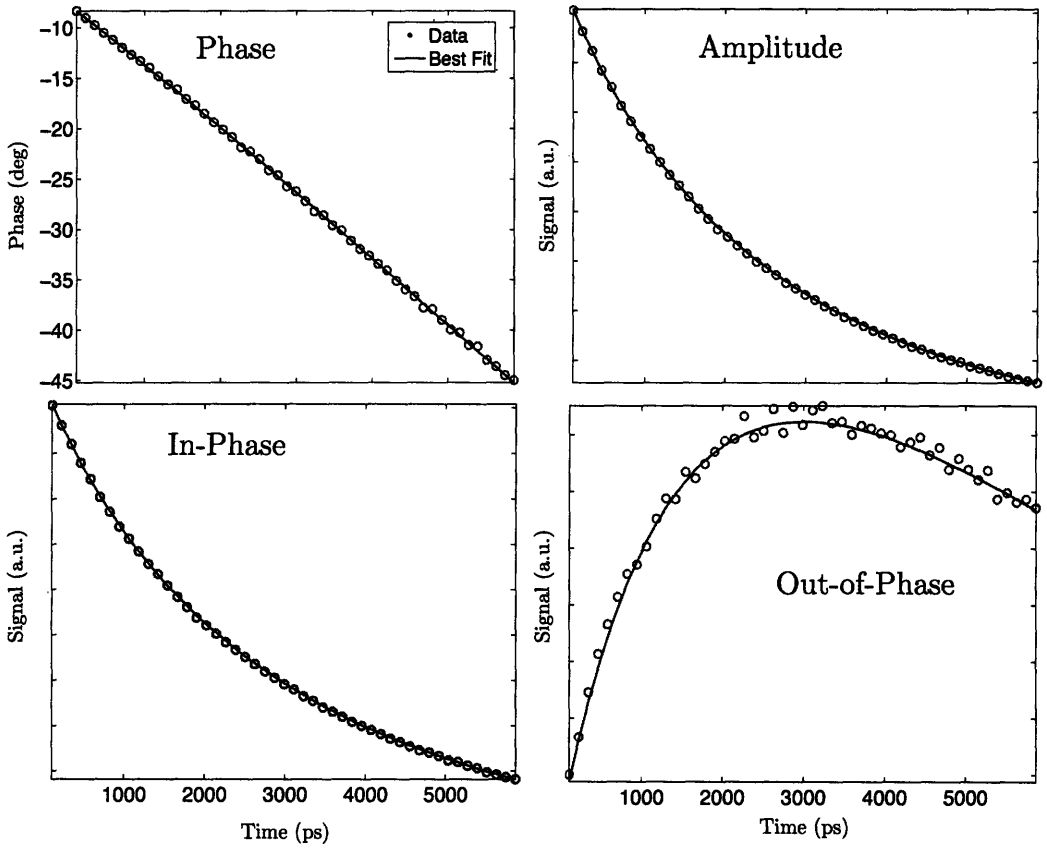

Figure 3-21: Experimental data from sapphire coated with 75 nm of Al. The measured thermal conductivity 39.6 W/mK, and the interface conductance was 78 MW/m^2K, in good agreement with literature values [16, 62]

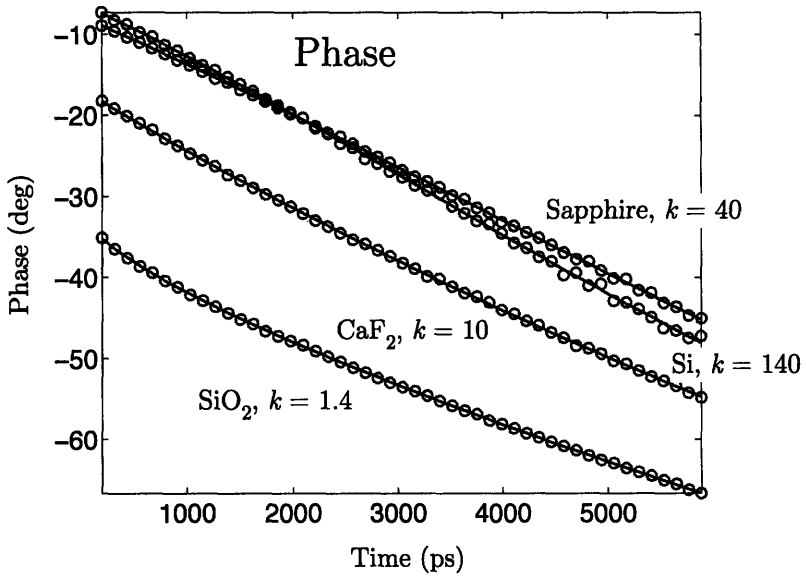

Figure 3-22: Phase data and best fit values for four materials, taken with a modulation frequency of 9.1 MHz.

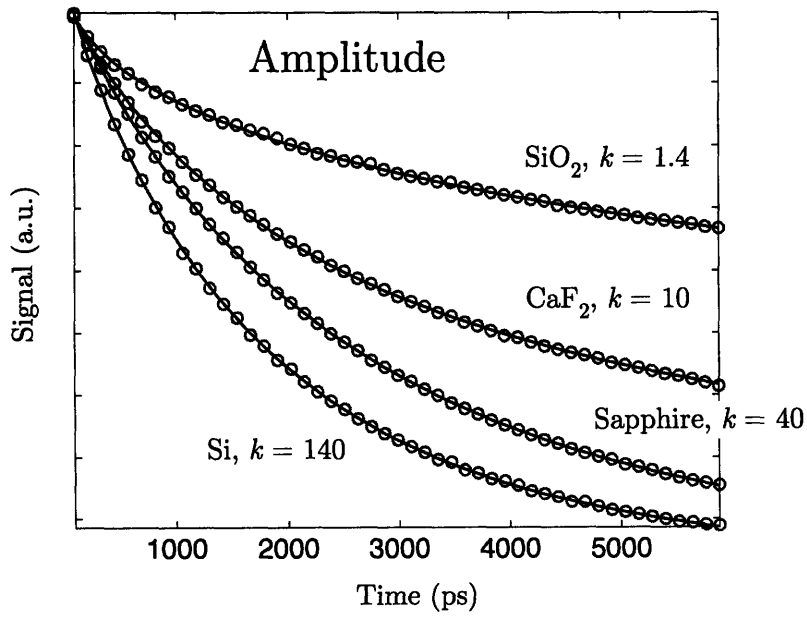

Figure 3-23: Amplitude data and best fit values for four materials, taken with a modulation frequency of 9.1 MHz.

ductivity of the substrate, and the thermal interface. When fitting multiple parameters to match one set of data, it is important that the parameters affect the model in independent ways. In the case of our model, certain sets of parameters (for example, thermal conductivity and heat capacity, or thermal conductivity and the metal layer thickness) affect the model in a similar way and so cannot be fit simultaneously. Thermal conductivity and the interface conductance, however, affect the model differently and can be fit simultaneously.

This fact is corroborated by additional information: acoustic echos generated by stress pulses induced in the metal film by the laser pulse. This pulse travels through the Al layer and is partially reflected at the Al-substrate interface. When the reflected pulses reach the surface of the Al, they produce a bump in the signal, and if the pulse makes multiple trips through the film then multiple echo bumps will be visible in the signal. This phenomenon has been studied in detail by others [64, 65], and a quantitative description is outside the scope of this thesis. The key point here is that if the interface is poor (for example due to a very thin layer of a contaminating material or surface roughness), then the echos will be stronger, and in addition the thermal transport across the interface will be smaller than for a good interface.

Figure 3-24 shows data from two identical substrates (thermal SiO_2) with different Al coatings. In the data on the left, the interface was contaminated during the deposition process, probably from glue used to hold a nearby sample, while in the data on the right, there was no contamination. The acoustic echos in the contaminated sample are clearly much stronger than in the clean sample, and we would therefore expect the thermal interface conductance to be much lower.

The full scans from these same two samples are shown in Fig. 3-25. In both cases the thermal conductivity is the same and matches the literature value [66], but the thermal interface conductance, G, is very different. In the case of the sample with many echos, the best fit value is $G = 48$ MW/m^{2}K, while for the sample without echos, $G > 200$ MW/m^{2}K. Above this value for a low thermal conductivity substrate, the interface conductance has little impact on the signal and can be considered infinite.

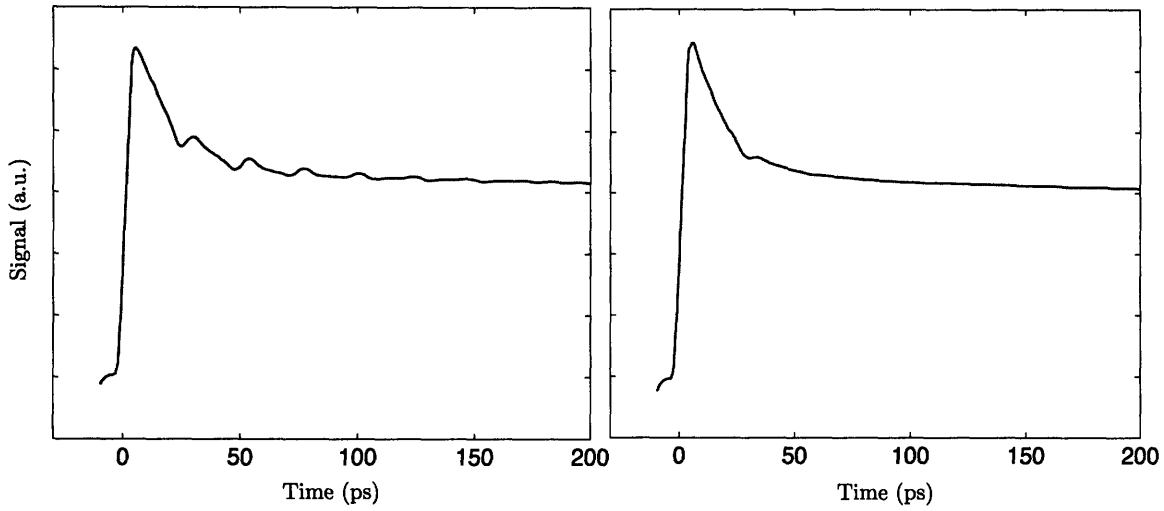

Figure 3-24: Data from Al on thermal SiO_2. In the figure on the left, the interface was contaminated during the deposition process, while in the data on the right, there was no contamination. The acoustic echos in the contaminated sample are clearly much stronger than in the clean sample.

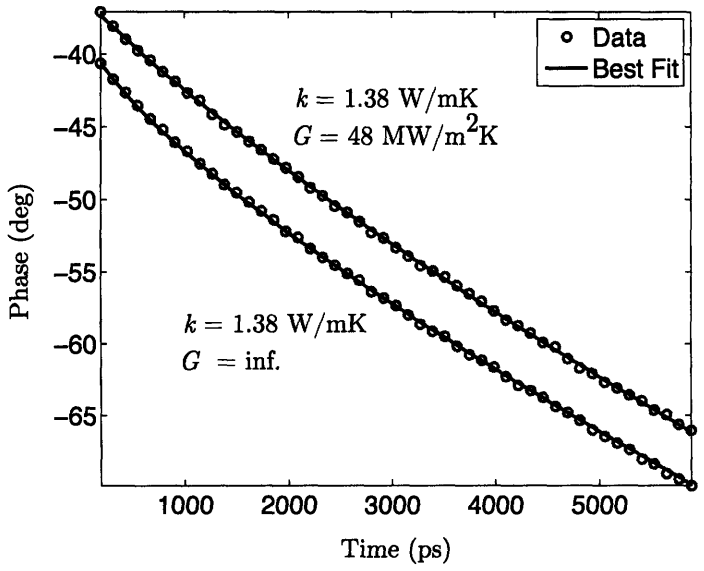

Figure 3-25: Full scan from the samples shown in Fig. 3-24. In the case with many echos, the thermal interface conductance is low, while in the case without echos it is high enough to have no impact on the measurement. The same value of thermal conductivity value is used in both fits.

3.7 Sample Preparation

3.7.1 Choice of the Metal Transducer

The thickness and optical quality of the metal absorber are critical to the accuracy of the pump-probe measurement. The metal layer must be sufficiently thick to prevent light from reaching the substrate, which may have its own transient reflection signal that would interfere with the measurement. On the other hand, if the layer is too thick, the diffusivity of excited electrons in the film begin to interfere with the result and can lead to incorrect results [17].

We use aluminum as the metal transducer layer, although other metals could also be used depending on the application. For most cases, aluminum is the superior choice for two reasons. The first is its high absorptivity at both 400 nm and 800 nm. Figure 3-26 shows the 99% absorption depth of aluminum, silver and gold from wavelengths from 350 nm to 850 nm [67]. Although the figure indicates that 40 nm of Al should be sufficient to absorb all incoming light, the actual optical properties of thin metallic films is highly dependent on the deposition process [68]. In practice, it has been found that an Al layer between 80 nm and 120 nm thick is optimal for pump-probe measurements [17]. The other reason for using Al is that at the probe wavelength, 800 nm, Al has the highest thermoreflectance coefficient of common metals [39]. Therefore, for a given temperature change an Al-coated sample will have the best signal-to-noise ratio.

As we saw in the preceding section, the quality of the Al-substrate interface can have a huge effect on the measured signal, although the model allows the thermal interface and substrate conductivity to be obtained simultaneously. Unfortunately, film thickness and thermal conductivity affect the measurement in similar ways and cannot be determined simultaneously. Therefore, it is important to understand the impact of the thickness of the Al layer on the measurement result.

Figure 3-27 shows the phase sensitivity, S_ϕ of the measurement to the Al layer thickness, Al layer thermal conductivity, and for comparison, the sensitivity to the thermal conductivity of the substrate for SiO_2 and Si. The thickness of the Al layer

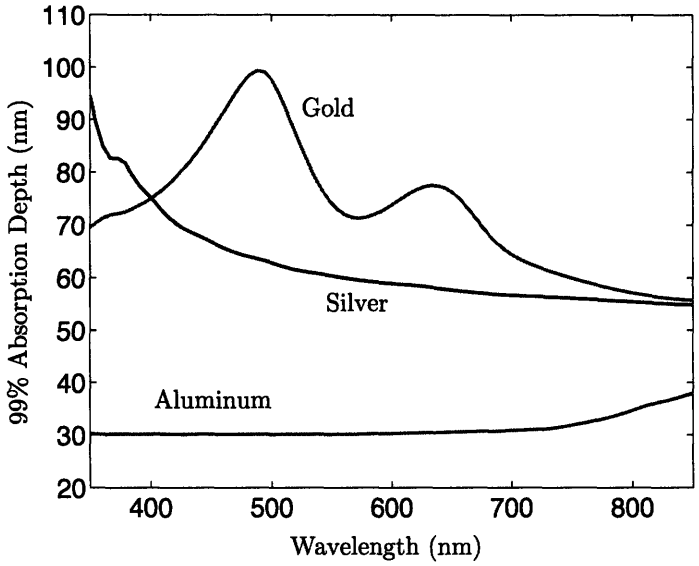

Figure 3-26: The 99% absorption depth for Aluminum, Silver and Gold.

has an equal or greater impact on the signal than substrate thermal conductivity, depending on the delay time, due to the heat capacity of the layer. A 5% error in film thickness will typically lead to a 5–10% error in the thermal conductivity value. The thermal conductivity of the metal layer, however, has virtually no impact on the measurement a long as it is above 150 W/mK. Since bulk Al has a thermal conductivity of 240 W/mK, even a relatively poor quality film will meet this requirement.

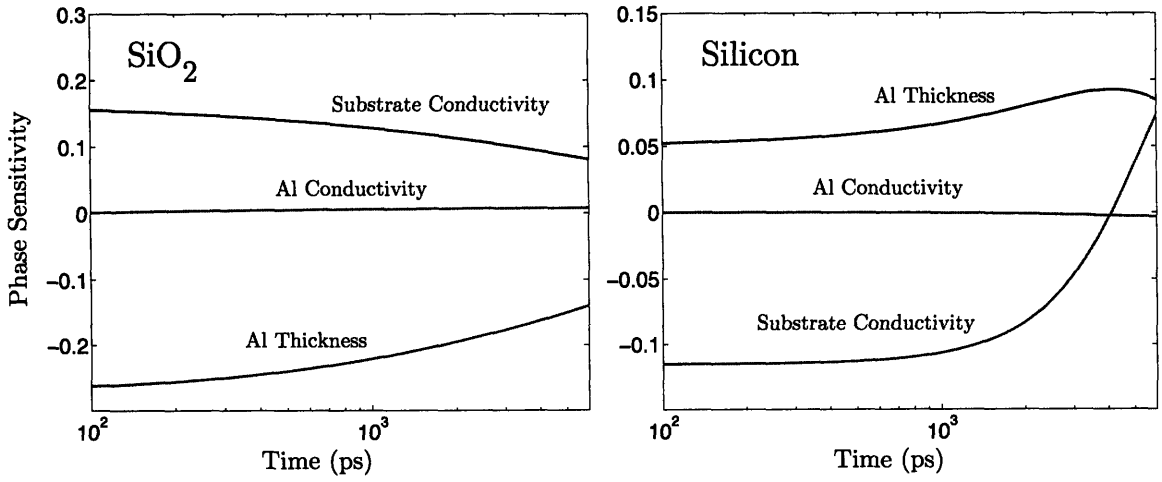

Figure 3-27: Phase sensitivity of the measurement to the Al layer thickness, Al layer thermal conductivity and the thermal conductivity of the substrate for SiO_2 and Si.

3.7.2 Film Thickness Characterization

As Figure 3-27 indicates, the measurement is quite sensitive to the thickness of the metal layer. Therefore, it is important that we characterize this thickness as accurately as possible. Fortunately, the measurement itself often provides this information in the form of acoustic echos [64], as we discussed in Section 3.6.1, and the thickness of the film can be accurately determined to within 1–2 nm. Figure 3-28 shows the acoustic echos in an 75 nm Al film on an SiO_2 substrate.

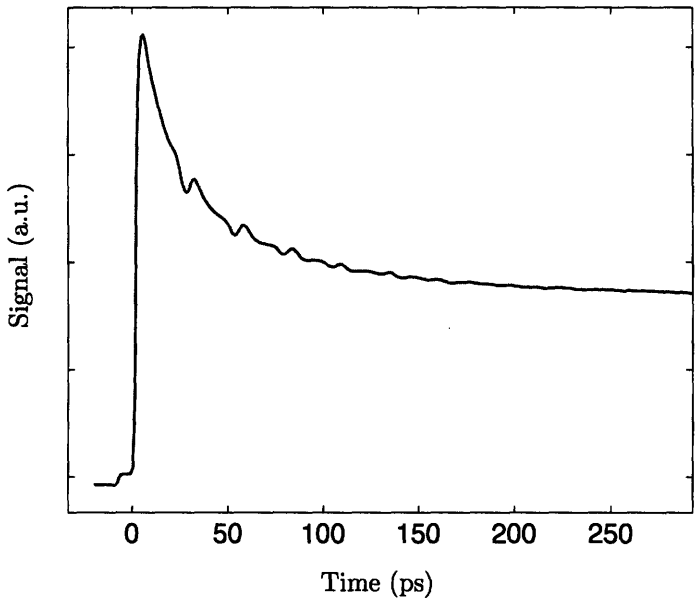

Figure 3-28: Acoustic echos in an 75 nm Al film on an SiO_2 substrate.

Each echo results from the sound pulse making one round trip through the Al film, and so the film thickness can be determined from:

$$d = \frac{1}{2} t_{\text{echo}} v_s \tag{3.56}$$

where d is the film thickness, t_{echo} is the time between echos and v_s is the longitudinal sound speed in the medium. In the case of Al, the longitudinal sound speed is taken as 6260 m/s [69]. Figure 3-29 illustrates the process for determining the film thickness graphically.

The thickness of the deposited Al film may vary significantly across the exposed

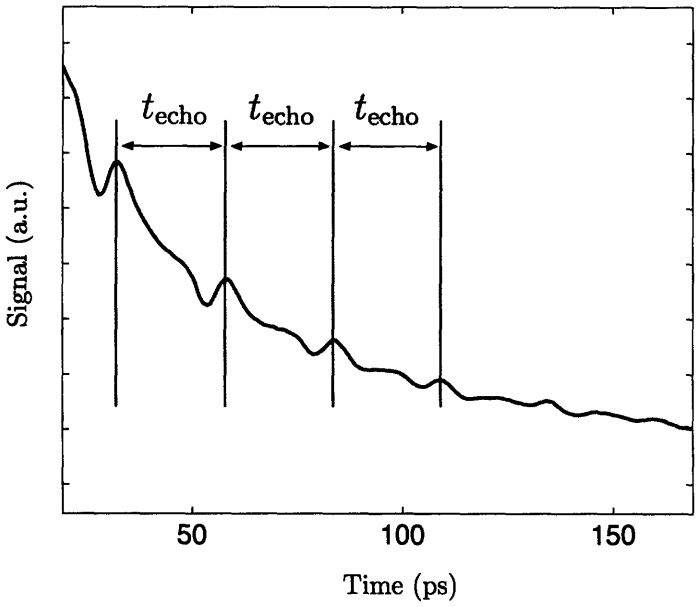

Figure 3-29: Measurement of the round-trip time of a sound pulse in an Al film.

area of the deposition chamber, and the nominal thickness value returned by the deposition machine is often only a rough estimate of the true thickness at any given location on the sample. For example, we used the acoustic echo technique to map out the Al thickness over an entire wafer coated in the ebeam chamber in MIT's Exploratory Materials Laboratory. The results are shown in Fig. 3-30. The desired thickness entered into the machine was 75 nm, but the actual thickness varied from 62 nm to 87 nm.

These results indicate that it is important to measure the Al thickness using acoustic echos for each sample tested, or at least for samples separated in the chamber by more than a few centimeters, depending on the deposition process and chamber. For some materials, if the acoustic impedance of the Al layer and the substrate match well and the interface is clean, the echos will not be strong enough to clearly measure the echo time. In this case, an alternative method is to place a small piece of a known substrate next to the sample in the deposition chamber. The thermal properties of the known substrate can then be used to calibrate the thickness of the Al layer in the nearby vicinity. We tried this approach for samples of SiO_2 and Si that did show strong acoustic echos, and found that the thickness determined via echos and

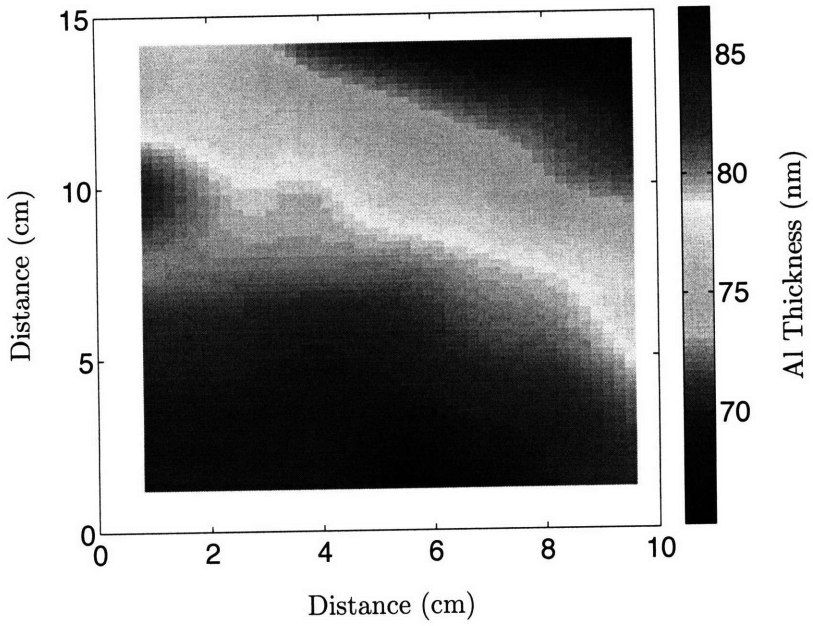

Figure 3-30: Aluminum thickness over an entire wafer coated in the ebeam chamber in MIT's Exploratory Materials Laboratory, as measured with acoustic echos.

determined via calibration to the known thermal properties typically agreed within 2 nm.

3.8 Steady Heating and Linearity

All of the analysis in this chapter is built upon the assumption of linearity. This requires that the thermoreflectance coefficient is linear with temperature over the range of temperatures we induce in the experiment, and that the physical properties remain constant. In addition, there is a steady temperature rise in the sample due the accumulation of heat in the sample which is balanced by loss to the surroundings. We can estimate each of these effects.

Roughly, we can estimate the temperature rise in the metal absorber due to a pump pulse by

$$\Delta T \simeq \frac{Q}{\rho c_p d} \tag{3.57}$$

where Q is the absorbed energy per unit area and d is the absorption depth of the metal at the pump wavelength. If we put in typical values (a pump spot with $1/e^2$

radius of 25 μm and power 100 mW, an absorption depth of 10 nm and a reflectivity of 98%), we get a temperature rise on the order of 0.5 K. This is small enough that the thermoreflectance coefficient and physical properties can be treated as constant.

The steady temperature rise can be estimated by solving the problem of a semi-infinite medium subjected to a steady heat input $q(r) = (2A_0/\pi w_0^2)\exp(-2r^2/w_0^2)$ where A_0 is the total absorbed power and w_0 is the $1/e^2$ beam radius. Figure 3.58 shows the calculated surface temperature due to both pump and probe beams in SiO_2, with $k = 1.4$ W/mK, and Si, with $k = 140$ W/mK. The input parameters were a pump radius of 25 μm and power of 60 mW, and probe radius of 4 μm and 5 mW, and a reflectivity of 0.98.

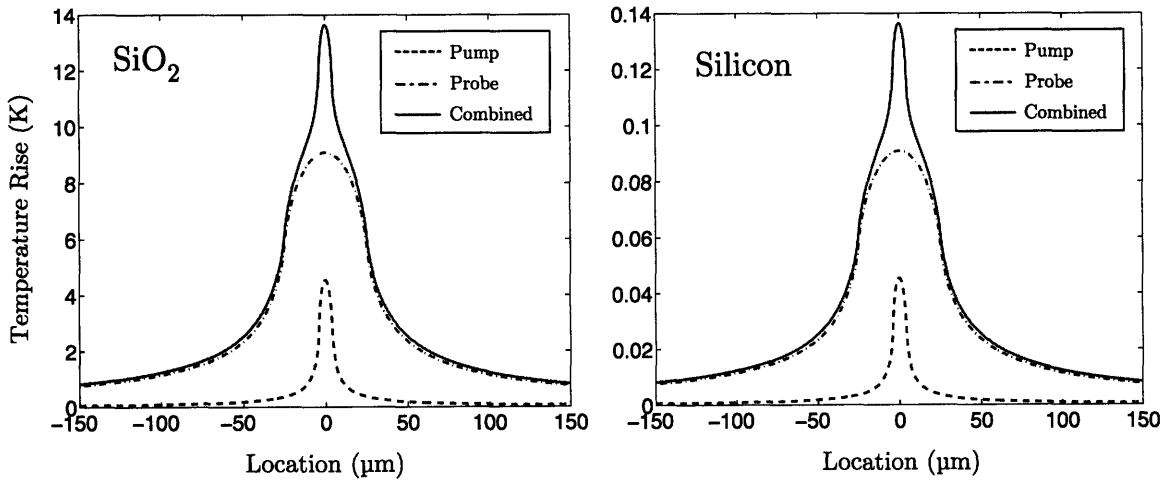

Figure 3-31: Calculated steady temperature rise in SiO_2 and Si under typical experimental conditions.

We can also quickly estimate the mean temperature rise by taking the low frequency limit of Eq. (3.48) [19]:

$$\overline{\Delta T} = \frac{(1-R)\dot{q}}{\sigma(2\pi w_0^2 + 2\pi w_1^2)^{1/2}} \tag{3.58}$$

Here $\overline{\Delta T}$ is the probe-averaged steady temperature rise, $\dot{q}$ is the combined incoming laser power of the pump and probe beams, R is the sample reflectivity, σ the thermal conductivity, and w_0 and w_1 are the pump and probe radii, respectively. For a thermal conductivity of around 1 W/mK, this gives a temperature rise of 10–15 K, while for

a thermal conductivity of 100 W/mK, the temperature rise is around 0.1 K under typical experimental conditions.

The above calculations indicate that the thermal system should behave in a linear way and that the steady temperature rise should be modest. We can verify this by making several measurements at different fluence levels and comparing the results. The mean fluence, or energy delivered in one pulse per unit area, over the $1/e^2$ radius w_0 is given by

$$\overline{f} = \frac{1}{\pi w_0^2} \int_0^{w_0} \frac{2A_0}{\pi w_0^2} \exp\left(\frac{-2r^2}{w_0^2}\right) 2\pi r\, dr = \frac{A_0}{\pi w_0^2} \tag{3.59}$$

where hereA_0 is the total energy per pulse. The peak fluence is given by

$$f_{\text{peak}} = \lim_{R\to 0} \frac{1}{\pi R^2} \int_0^{R} \frac{2A_0}{\pi w_0^2} \exp\left(\frac{-2r^2}{w_0^2}\right) 2\pi r\, dr = \frac{2A_0}{\pi w_0^2} = 2\overline{f} \tag{3.60}$$

Figure 3-32 shows data from a silicon sample taken at four mean fluence levels from 0.75 J/m^2 to 5 J/m^2. The plot on the left show the amplitude signal plotted on a linear scale, while the plot on the right shows the same data plotted on a log scale. Because the system is behaving linearly and steady heating is not having a noticeable effect, on a log scale the signals are simply shifted copies of each other. At lower fluence levels the signal becomes increasingly noisy.

In Fig. 3-33 we subtract the signal at $t = 0$ and normalize all four curves at $t = 100$ ps. Aside from an increase in noise at lower fluence levels, the curves are indistinguishable.

Finally, we perform a similar test on an SiO_2 sample. Since the thermal conductivity is 100 times smaller than in Si, steady heating could be more of a factor. Figure 3-34 shows data taken at three fluence levels, plotted on a log scale. As in the case of the Si data, the curves appear as shifted copies of each other. The thermal conductivity of SiO_2 increases with increasing temperature at a rate of roughly 0.2%K^{-1} near 300 K [70], so the fact that the shape of the curves does not change implies that temperature rise is at most a few degrees K and steady heating is not an important factor under typical experimental conditions. However, if the optical quality of the metal film is poor and the reflectivity is significantly lower, the absorbed

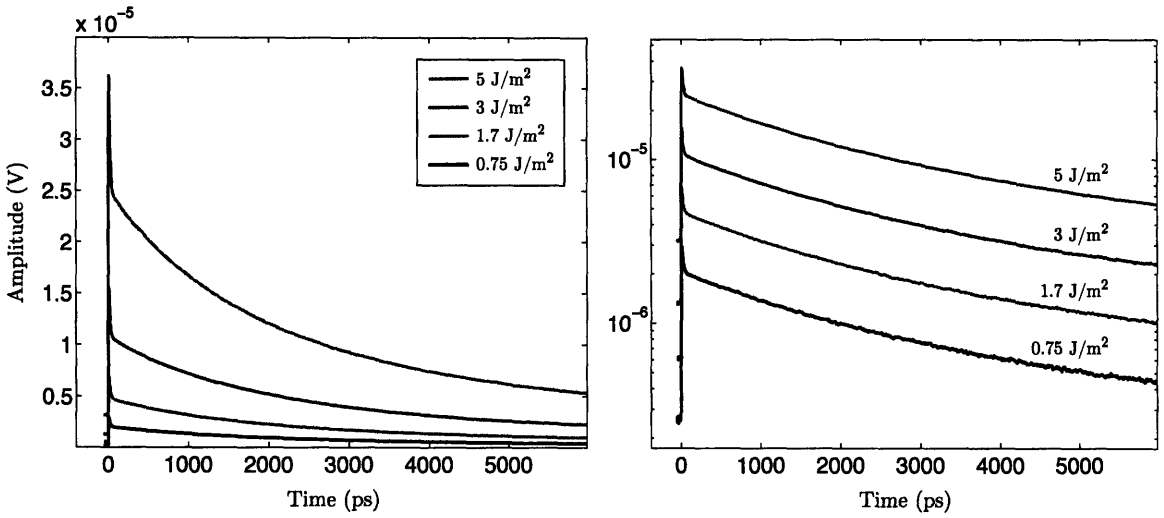

Figure 3-32: Data from silicon at four fluence levels. The plot on the left has a linear scale, while the plot on the right shows the same data plotted on a log scale. Because the system is behaving linearly and steady heating is not having a noticeable effect, on a log scale the signals are shifted copies of each other.

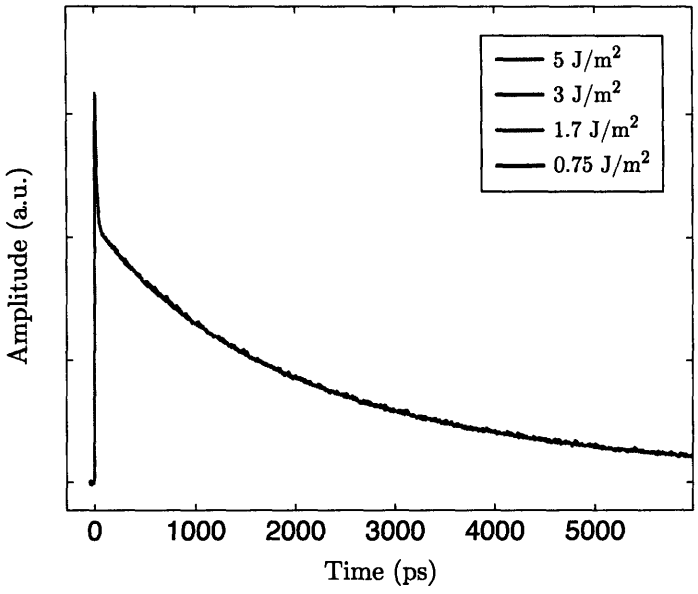

Figure 3-33: The data at four fluence levels from Fig. 3-32. The signal at $t = 0$ has been subtracted and each curve is normalized at 100 ps. Aside from an increase in noise, the curves are indistinguishable.

power will increase and the measurement will be affected; at some point the absorbed power may high enough to burn the sample.

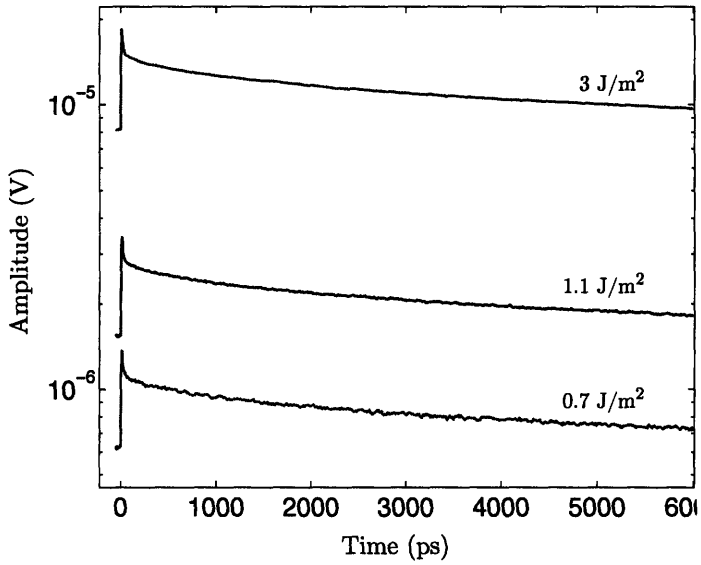

Figure 3-34: Data from SiO_2 at three fluence levels. The fact that shape of the curves does not change implies the steady temperature rise is small.

3.9 Summary

A mathematical description of the measurement process has been given using the language of linear systems theory, encompassing the work on pulse accumulation by Capinski et. al. [15] and its extension to radial isotropic heat conduction through multilayer structures by Cahill [19], in a clear, consistent way. This approach enables us to explore the relationship between pulse accumulation and radial conduction effects and clearly show how pulse accumulation essentially allows two length scales to be probed simultaneously. In addition, our analytical solution for radial heat transfer through multilayer structures includes anisotropic thermal properties without any additional computational expense over the isotropic solution given by Cahill [19].

A method has been presented for fitting the phase data and the various factors that can affect the final measured thermal conductivity were discussed. The measured value is sensitive to the thickness of the Al layer, although this can be determined

using acoustic echos or via a reference material placed near the sample during Al deposition. Finally, it was shown that nonlinearity and steady heating are not important factors under typical experimental conditions.

Chapter 4

Application of the Pump-Probe Technique to Liquids, Anisotropic Properties, and Microstructures

In the previous two chapters, we described the apparatus and theory for measuring the thermal properties of solids. Now, we build on those results to extend the pump-probe technique into new territory. Three topics will be addressed: (1) the measurement of liquids; (2) measurement of in-plane thermal properties in anisotropic samples; and (3) the characterization of microstructures.

4.1 Thermal Conductivity of Liquids

In this section, we present a convenient method for measuring the thermal conductivity of liquids. The principle is simple: liquid is placed on a glass substrate coated with a thin film of metal. The laser impinges on the metal through the glass, and the cooling of the metal film is used to deduce the thermal conductivity of the adjacent liquid.

This approach has unique advantages over other methods for measuring the thermal conductivity of liquids. Only a few μL of liquid (often a single droplet) are needed to obtain a reliable measurement. This is far less than the volume needed for

the standard hot-wire method developed by Nagasaka [71], and at such small volumes the effects of convection are eliminated. And, because there is no direct interaction between the laser light and the liquid, there are no restrictions on its optical properties. This is an advantage over transient grating methods which rely on thermally induced changes in the optical properties of the liquid to obtain thermal diffusivity [72, 73]. In addition to liquids, the technique can be applied to malleable solids such as viscous grease and epoxy.

The method requires that the thermal properties of the Al-coated glass slide are well-known. We find the thermal conductivity of the glass, the Al-glass thermal conductance, and the thickness of the Al layer by applying the methods described in the previous section to the coated slide. Once these properties are known, they are kept constant while multiple liquids are tested.

4.1.1 Experimental Setup and Procedure

Liquid samples are held in the arrangement shown in the left-hand illustration of Fig. 4-1. A piece of glass is coated with 70–100 nm of Al which acts a temperature transducer. Liquid is placed in contact with the Al and is held in place with a second piece of glass. The second piece of glass typically has a channel 100–200 μm deep etched in it to contain the liquid, although in practice we achieve identical results if a flat piece of glass is used to trap a thin liquid layer with surface tension. The pump and probe beams impinge through the glass onto the Al, and the properties of the liquid are deduced from the cooling curve. The same approach works for amorphous solids like pastes, greases and epoxies, which are simply applied to the Al surface as shown in the right-hand illustration of Fig. 4-1.

4.1.2 Theory

As with solids, an analytical solution for heat transfer in the sample is most easily obtained in the frequency domain. In Section 3.3, the solution for the surface temperature was obtained for unidirectional heat flow through a multilayer structure;

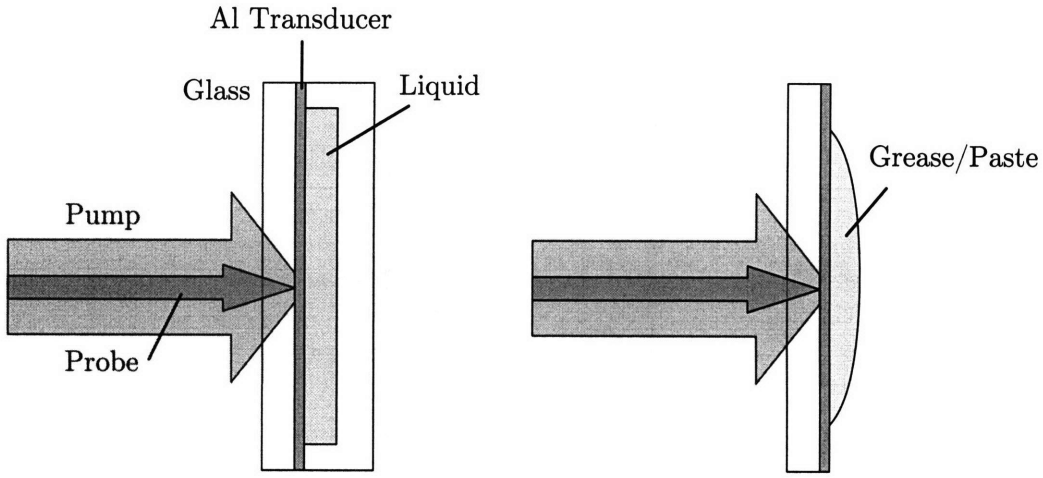

Figure 4-1: Sample arrangement for measurement of liquid thermal conductivity (left) and greases, pastes and other malleable solids (right).

the final result, including radial conduction, is given by Eq. (3.50). Now, we extend the solution to the case of bidirectional heat flow by solving two layered systems and matching the boundary conditions at the interface. The model problem is illustrated in Fig. 4-2.

The problem is comprised of two multilayer systems, each of which can be represented by a system matrix found by multiplying matrices for the individual layers together as was done in Eq. (3.35) for unidirectional heat flow. The first system, $\mathbf{M}_1$, is a two-layer stack consisting of the interface conductance G_1 between the glass slide and the Al, and a semi-infinite glass layer. The second system, $\mathbf{M}_2$, has three layers: the Al layer, the conductance G_2 between the Al and the liquid, and a liquid layer. Optionally, if the liquid layer is very thin (less than ~ 1 μm, a fourth, semi-infinite glass layer can be included.

For each matrix system, we can write

$$\begin{bmatrix} \theta_{b,1} \\ f_{b,1} \end{bmatrix} = \begin{bmatrix} A_1 & B_1 \\ C_1 & D_1 \end{bmatrix} \begin{bmatrix} \theta_{t,1} \\ f_{t,1} \end{bmatrix} \tag{4.1}$$

$$\begin{bmatrix} \theta_{b,2} \\ f_{b,2} \end{bmatrix} = \begin{bmatrix} A_2 & B_2 \\ C_2 & D_2 \end{bmatrix} \begin{bmatrix} \theta_{t,2} \\ f_{t,2} \end{bmatrix}$$

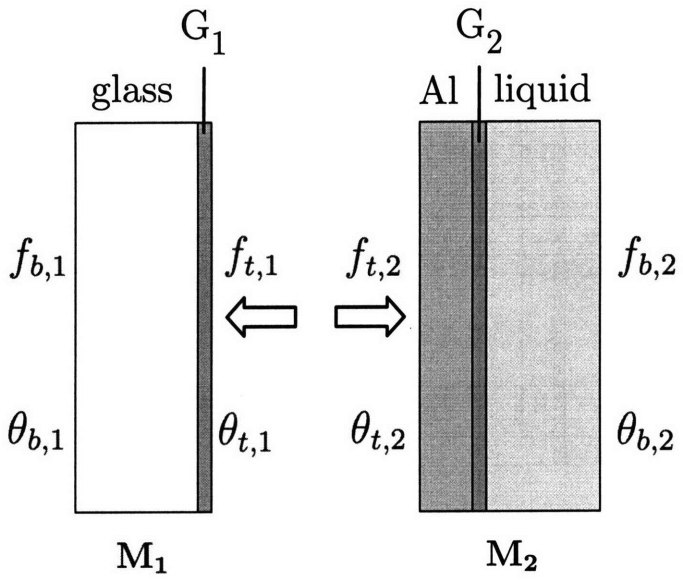

Figure 4-2: Thermal model for bidirectional heat conduction into the liquid and glass substrate. The problem is divided into two multi-layer stacks: Stack 1 consists of the thermal conductance between the glass and the Al transducer layer, and a semi-infinite layer of glass; stack 2 consists of the Al transducer, the thermal conductance between the Al and the liquid, and a semi-infinite liquid layer.

The boundary conditions at the interface are:

$$\theta = \theta_{t,1} = \theta_{t,2} \tag{4.2}$$

$$f = f_{t,1} + f_{t,2} \tag{4.3}$$

where θ is the common interface temperature and f is the total heat flux supplied to the system.

Again assuming either adiabatic or semi-infinite bottom surfaces for each stack, we can we write:

$$\begin{aligned} C_1\theta + D_1 f_{t,1} &= 0 \\ C_2\theta + D_2(f - f_{t,1}) &= 0 \end{aligned} \tag{4.4}$$

After some algebra, we find the temperature of the Al layer at the Al-glass interface:

$$\theta = \left(\frac{-D_1 D_2}{D_1 C_2 + D_2 C_1} \right) f \tag{4.5}$$

In a method analogous to the one used in Section 3.3.2, we find that this result holds true for one-dimensional conduction, or two dimensional conduction with radial transport after taking a Hankel transform of the diffusion equation to get the matrix elements in Eq. (4.1). The final frequency response of the measured aluminum temperature in real-space is identical to Eq. (3.50), except that the term $-D/C$ has been replaced by combination of matrix elements in Eq. (4.5):

$$H(\omega) = \frac{A_0}{2\pi} \int_0^\infty k \left(\frac{-D_1 D_2}{D_1 C_2 + D_2 C_1} \right) \exp\left(\frac{-k^2(w_0^2 + w_1^2)}{8} \right) dk \tag{4.6}$$

This solution for the frequency response is inserted in Eq. (3.27), which we integrate numerically.

4.1.3 Sensitivity

We can use the phase sensitivity, S_ϕ, as defined in Eq. (3.54) to examine the sensitivity of the measurement in various situations. We focus on the phase sensitivity here since generally we use the signal phase to fit the physical properties. In general, sensitivity is limited by heat flow into the glass, which has a thermal conductivity on the order of 1 W/mk; sensitivity increases as the fraction of heat flowing into the liquid increases. Figure 4-3 shows sensitivity to both the liquid thermal conductivity and the Al-liquid interface conductance for water and decane. Water has the highest thermal conductivity of commonly encountered liquids, around 0.6 W/mK at room temperature, while decane has a low value typical of many hydrocarbon liquids, 0.13 W/mK. In both liquids, sensitivity to the thermal conductivity is significantly greater than sensitivity to the interface conductance, and in decane the interface sensitivity is so small that it is difficult to obtain a reliable value. For the sensitivity calculation, the Al-liquid interface conductance is taken as 60 MW/m^{2}K, a value

that typically produced good fits in our measurements and is in line with previously published observations [44].

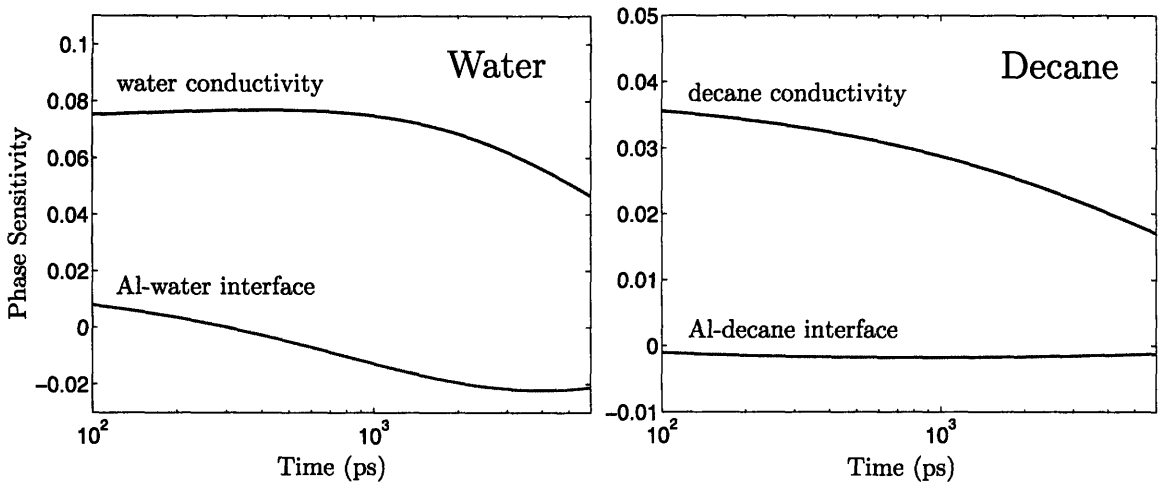

Figure 4-3: Sensitivity liquid thermal conductivity and the Al-liquid interface conductance for water and decane. Water has a thermal conductivity of 0.6 W/mK at room temperature, while that of decane is 0.13 W/mK. The Al-liquid interface conductance is taken as 60 MW/m^{2}K.

Figure 4-4 plots the phase sensitivity to the liquid thermal conductivity and the Al-liquid conductance as a function of liquid thermal conductivity. The values are plotted for a delay time τ of 1000 ps, although the curves look similar over the range of delay times. As the figure shows, the model is an order of magnitude more sensitive to the liquid thermal conductivity than to the interface conductance, and in general sensitivity to both quantities increases with liquid thermal conductivity since a larger fraction of heat flows into the liquid rather than the glass slide.

Finally, we look at the effect of the thickness of the liquid layer on the measurement. Since the thermal conductivity of both liquid and glass are low, accumulation effects will be important and the relevant length scale of the problem will be determined by the penetration depth of the thermal waves at the EOM modulation frequency, which is typically 1–10 MHz. In Fig. 4-5, the sensitivity to the liquid thickness is plotted for water and decane at 1 MHz and 10 MHz. As expected, a thicker layer of liquid is probed for water since it has 5× higher thermal conductivity. Also, for both liquids decreasing the frequency from 10 MHz to 1 MHz increases the

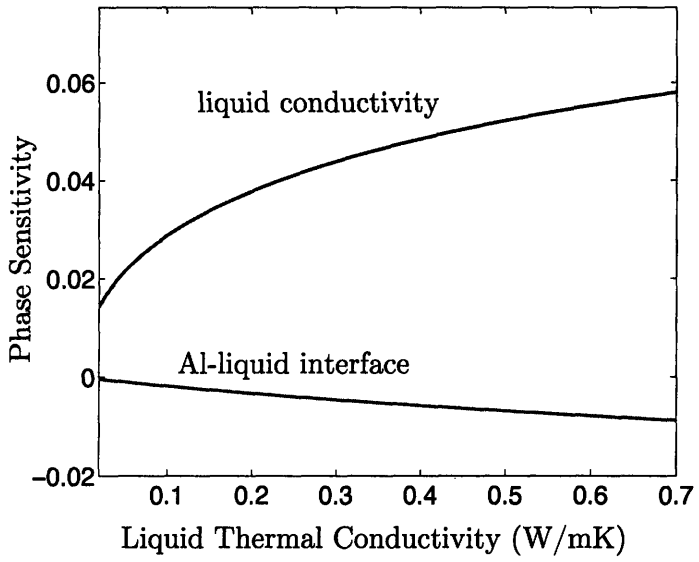

Figure 4-4: Phase sensitivity to the liquid thermal conductivity and the aluminum-liquid thermal interface conductance taken at a delay time of 1000 ps, plotted as a function of liquid thermal conductivity.

thickness of the liquid being probed by a factor of ~3, or $\sqrt{10}$. This is expected since the thermal penetration depth is given by $L = \sqrt{2\pi\alpha/\omega_0}$ where α is the thermal diffusivity of the liquid. At 10 MHz, sensitivity to the liquid layer thickness vanishes after 200 nm of liquid for both liquids. This implies that an extremely thin film of liquid is sufficient to obtain thermal properties without accounting for the effects of the containing glass slide or channel.

4.1.4 Results

The amplitude and phase of a typical liquid measurement, in this case from deionized water, are shown in Fig. 4-6. Qualitatively, the data appear similar to data obtained from solids, except for the a superimposed weak, decaying oscillation. Figure 4-7 shows the first 500 ps of a similar set of data, exposing the oscillations more clearly. Theses oscillations are due to the fact that we are now probing the Al through a transparent medium and are detecting a phenomena known as Brillouin back-scattering (BBS) [33]. BBS is well known and has been used to study a wide range of acoustic phenomena in solids and liquids. A detailed treatment is outside the scope of the

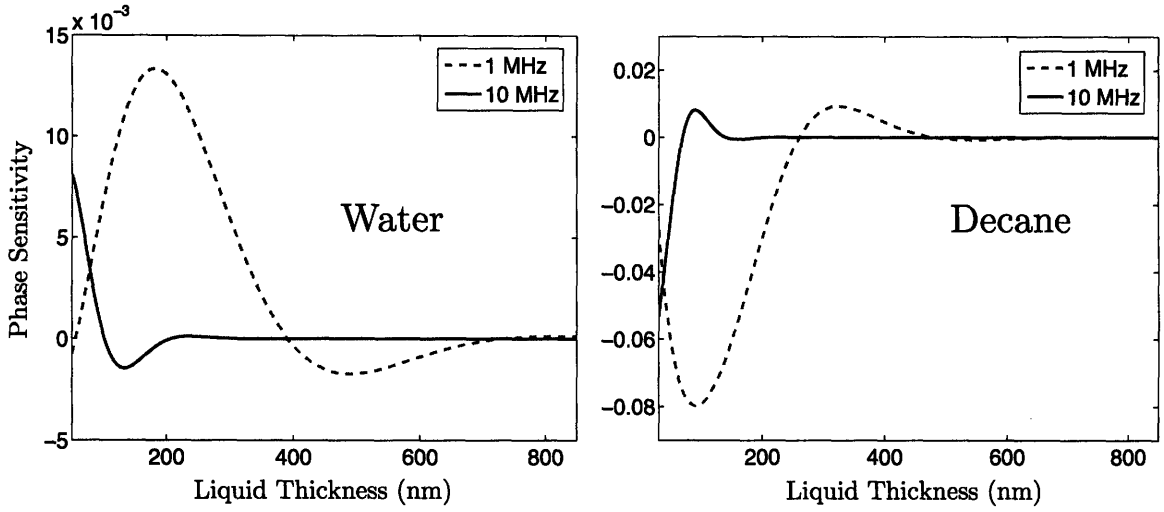

Figure 4-5: Sensitivity to the liquid thickness is for water and decane at 1 MHz and 10 MHz.

this thesis, but in essence the oscillation arise from the interference between the reflected acoustic pulse and the probe wavelength. Through conservation of momentum, at normal incidence the acoustic frequency, f_{ac}, is related to the probe wavelength through $f_{ac} = 2nc/\lambda$ where n is the index of refraction, c is the speed of sound in the transparent medium, and λ is the probe wavelength. The measured acoustic frequency in this case is 21 GHz, and the result can be used to calculate the speed of sound in the glass slide: $c = 5500$ m/s, consistent with the accepted value for Pyrex glasses. The oscillations are small enough compared to the thermal signal that they do not interfere with the model fit, especially in the case where the phase data is used since no normalization of the data is necessary.

As with solid measurements, we use a least-square minimization routine to vary the liquid thermal conductivity and the Al-liquid thermal conductance, G_2, to match Eq. (3.27) to the data. The fit value for the interface conductance varied widely at different locations on the sample, and from liquid to liquid. We attribute this to the fact that our slides became microscopically scratched after numerous tests, and also to the fact that the model is generally not very sensitive to the interface parameter, as shown in Fig. 4-5. Nonetheless, values for G_2 typically ranged from 50–100 MW/m^{2}K for our samples, in fair agreement with other findings. [44] Sample phase data and

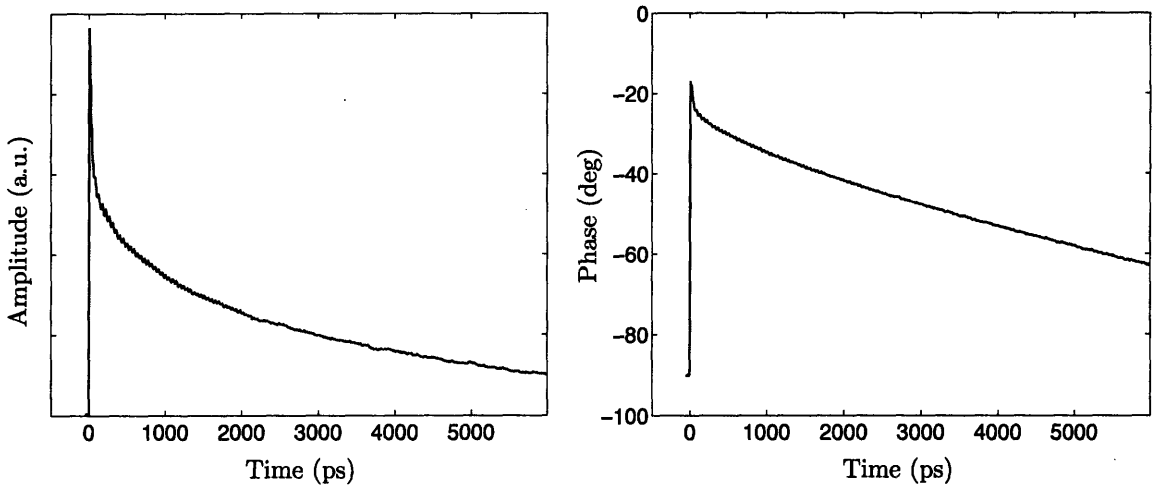

Figure 4-6: Amplitude and phase of a typical liquid measurement, in this case from deionized water.

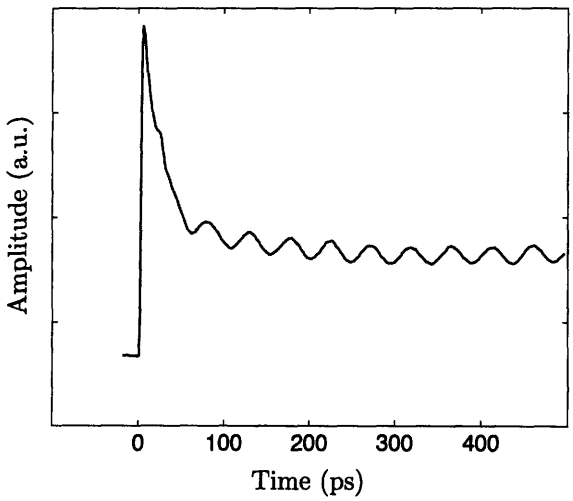

Figure 4-7: Signal oscillations caused by Brillouin back-scattering in the glass slide

best fit curves for three liquids and air are shown in Fig. 4-8. The same fits for the amplitude data are shown in Fig. 4-9. Water is among the most thermally conductive liquids (excluding liquid metals and salts), while air it fit well assuming an adiabatic boundary condition at the Al-air interface. Thus, most liquid measurements will fall within the range of these four curves. For this data, a Pyrex slide with a thermal conductivity of 1.1 W/mK was used. The slide was coated with 75 nm of Al.

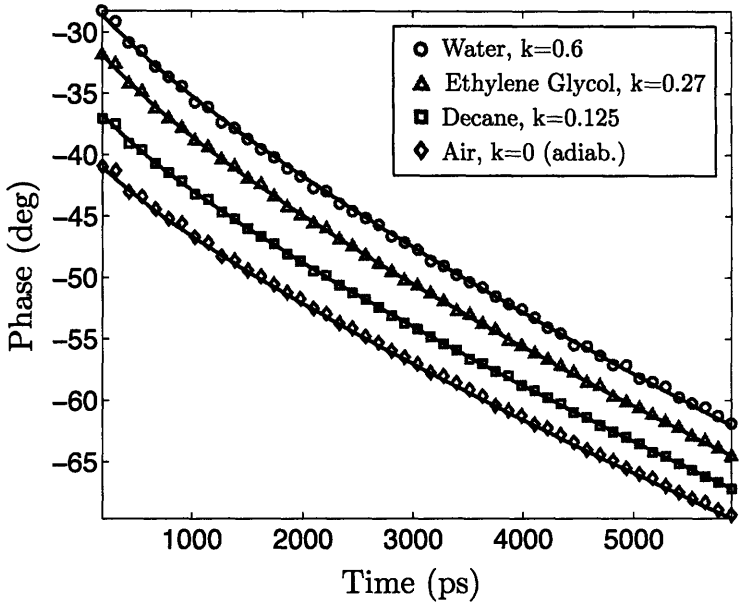

Figure 4-8: Phase data and best fit curves for three liquids and air.

Six liquids and a thick silicone grease were measured with this method at room temperature. Typically, we would measure five locations on a sample and take the mean value; variation between locations was on the order of 10%, slightly higher for the low conductivity liquids. The results are compared to the accepted values at 300 K in Fig. 4-10. The largest error is less than 5%.

We verified that convection was not present by trying three liquid channel depths (200 μm, 100 μm, and a droplet squeezed between two slides) for two liquids, water and decane. One would expect that viscous forces would overwhelm inertial forces at these length scales, and indeed we saw no change in our results among these configurations. The steady temperature rise in the liquid is similar to that for glass

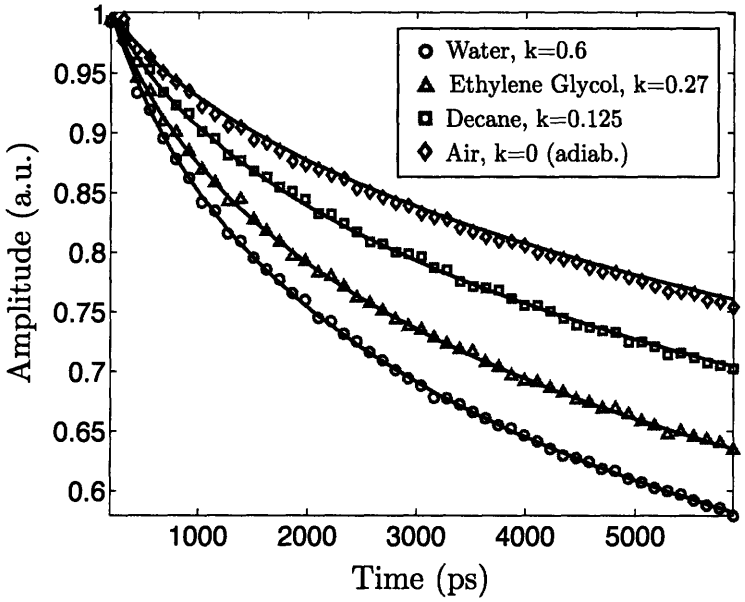

Figure 4-9: Amplitude data and best fit curves for the same three liquids and air.

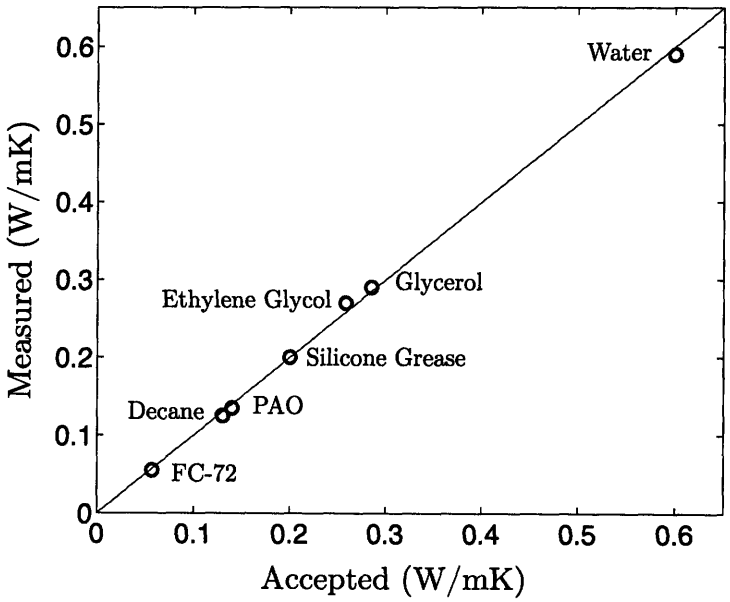

Figure 4-10: Measured and accepted thermal conductivity values for six liquids and silicone grease.

as we discussed in Section 3.8. We did not see a significant change in our results as we changed the pump power from 20–80 mW, although above 80 mW signal stability decreased, possibly due to bubble formation.

One additional observation is that water proved the most difficult liquid to measure, due to a reaction between the aluminum and water while the laser was focused onto the sample. For an Al film on the order of 70 nm, the signal would usually become unstable within a few seconds and obtaining a reliable measurement was impossible. Other liquids, such as decane, remained stable indefinitely. We overcame this problem by using a slide coated with 100 nm of Al. The thicker film degraded more slowly and the signal would usually remain stable for a minute or more, long enough to obtain several measurements from one location. A better solution may be to change the transducer metal to a nonreactive metal such as gold, which has a smaller thermoreflectance coefficient but would not react with the water.

Malleable Solids

As we mentioned in the introduction to this section and showed in Fig. 4-1, this technique provides a convenient way to measure the thermal conductivity of a whole class of malleable solids such as greases, pastes and epoxies. In Fig. 4-11 we show sample phase and amplitude data from two such materials: silicone grease ($k = 0.2$ W/mK) and an alumina-impregnated epoxy ($k = 2.1$ W/mK). In addition, measurements were made on a silver paint and on a boron nitride film that was applied via spray can, but the measured signals in these cases were identical to that of a slide with no material applied, indicating that there was a gap between the Al layer and the applied substance. This hints at the potential of the method for evaluating the behavior of thermal interface materials in practical applications, such as between a heat-sink and a microprocessor, a possibility we discuss further in Section 6.2.

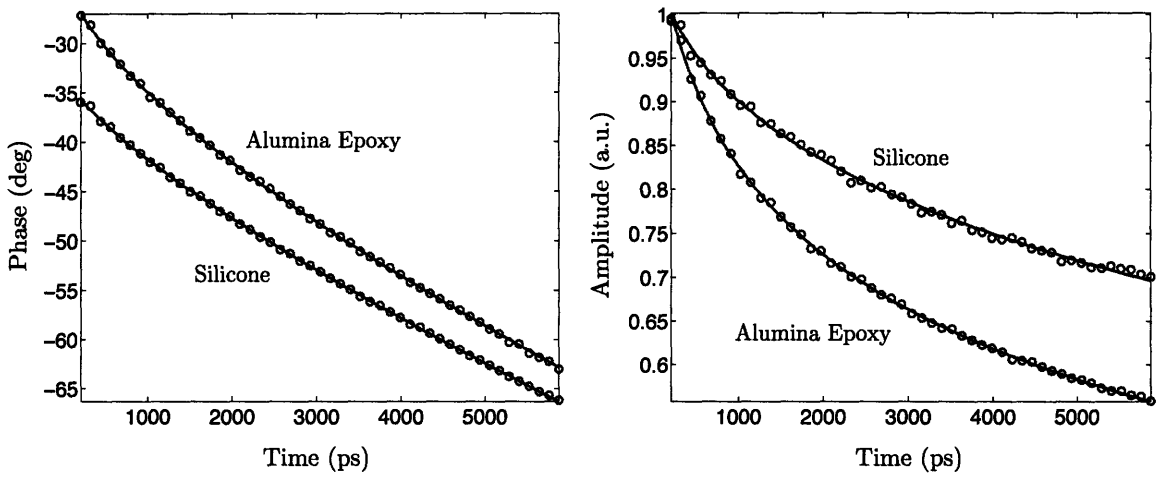

Figure 4-11: Sample phase data (left) and amplitude data (right) and best fit curves for silicone grease ($k = 0.2$ W/mK) and an alumina-impregnated epoxy ($k = 2.1$ W/mK).

4.2 In-Plane Thermal Properties

In the previous chapter, special attention was given to the role of pulse accumulation effects and they way they mix the impulse response of the thermal system, $h(\tau)$, with the response to a periodic input, $H(\omega)$, in the measured signal. As we discussed in Section 3.3.2, the impulse response decays over a length scale sufficiently short compared to the beam spot radius that all transport is essentially one-dimensional. The frequency response, however, has a characteristic length of $L = \sqrt{2\pi\alpha/\omega_0}$ which can be comparable to the focused spot size. In this case, radial conduction effects enter into the signal and should be accounted for to obtain an accurate measurement. As we showed, the one-dimensional solution, Eq. (3.34), can be extended to include radial effects by re-defining the variable q as

$$q^2 \equiv \frac{\sigma_r k^2 + \rho c i\omega}{\sigma_z} \tag{4.7}$$

which contains both the radial, or in-plane thermal conductivity, σ_r, and the cross-plane thermal conductivity, σ_z.

In this section, we take advantage of the fact that both thermal conductivities are present in the solution and show how, under the right conditions, we can experimentally obtain both the in-plane and cross-plane thermal conductivities. The primary example will be single-crystal graphite. It is highly anisotropic, and its thermal properties are well-known, so it is a convenient way to verify the technique. We also examine the more difficult case of a SiGe superlattice and discuss the limitations of the method.

4.2.1 Highly Ordered Pyrolytic Graphite

Graphite has a lamellar structure, composed of stacked planes. The bonding forces within the lateral planes are much stronger than those between the planes, thus explaining its highly anisotropic elasticity and lattice thermal conductivity [74]. Highly ordered pyrolytic graphite (HOPG) is characterized by large, single-crystal regions

which can be expected to exhibit maximum mechanical and thermal anisotropy. Literature values for the cross-plane thermal conductivity are on the order of 5–8 W/mK, while the in-plane thermal conductivity is around 2000 W/mK, or 300× higher than the cross-plane value [63]. Figure 4-12 shows an image of a HOPG sample from our CCD camera. The large, single-crystal grains are clearly visible. The pump and probe spots are focused within the white circle in the image.

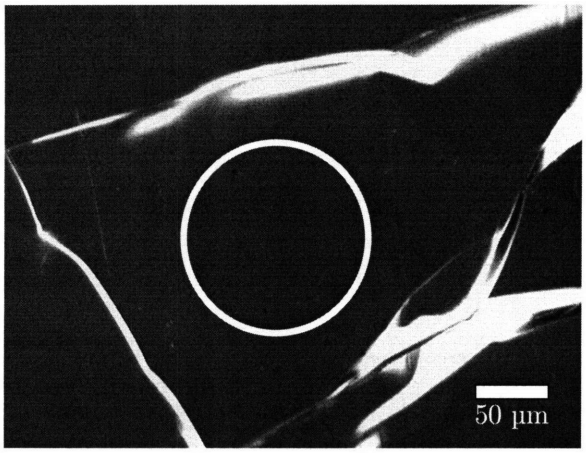

Figure 4-12: An image of our HOPG sample. Large, single-crystal grains are clearly visible. The pump and probe spots are focused within the white circle in the image.

The sample was coated with 72 nm of Al, as determined by acoustic echos. Figure 4-13 shows the clear echo signal.

Unlike the thermal measurement of a thermally isotropic sample, the model for an anisotropic solid requires three unknown parameters: the cross-plane conductivity, σ_z, the in-plane conductivity, σ_r, and the Al-sample interface conductance, G. However, when the beam spot is large and the modulation frequency is high, the model is insensitive to the in-plane properties. Thus, we can perform a measurement with a large pump spot at high frequency to measure σ_z and G in exactly the same was as described in the previous chapter, ignoring anisotropy. Then, we can perform additional measurements at lower frequencies, or smaller spot sizes, or both, to extract σ_r, using the values we obtained for σ_z and G from the high-frequency measurement.

In Fig. 4-14, we show how the sensitivity of graphite to in-plane thermal conductivity varies as a function of modulation frequency and pump spot size. All calculations

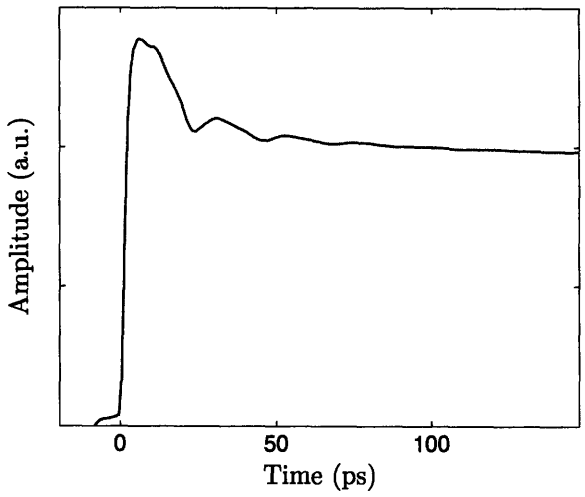

Figure 4-13: Acoustic echos from the HOPG sample. The measured Al thickness is 72 nm.

use the best-fit values for thermal properties, as listed in Table 4.1. In the left figure, the probe $1/e^2$ radius is 5 μm and pump $1/e^2$ radius is 25 μm. By reducing the modulation frequency from 12 MHz to 1 MHz, sensitivity is increased by more than an order of magnitude. In the figure on the right, the delay time is fixed at $\tau = 1000$ ps and the probe $1/e^2$ radius is held at 5 μm while the pump radius is varied. At 12 MHz modulation, when the pump radius is 50 μm there is virtually no sensitivity to σ_r. At lower frequencies smaller pump sizes, however, the measurement is sensitive to radial conductivity.

Figure 4-15 shows both the phase and amplitude data, along with best fit curves, at a modulation frequency of 11.6 MHz, a probe radius of 5 μm and a pump radius of 50 μm. Under these conditions, the measurement is insensitive to the in-plane conductivity and we find the cross plane thermal conductivity, σ_z, to be 5.7 W/mK and the interface conductance, G, to be 48 MW/m^{2}K. The density and specific heat were taken as 2700 kg/m^3 and 709 J/kgK, respectively [63].

Following this measurement, the pump spot radius was reduced to 26 μm and the measurement was repeated at three frequencies: 11.65 MHz, 3.65 MHz, and 1.11 MHz. The phase data and best fit curves are shown in Fig. 4-16. As we would expect from our discussion in Section 3.2, when the EOM modulation period becomes long

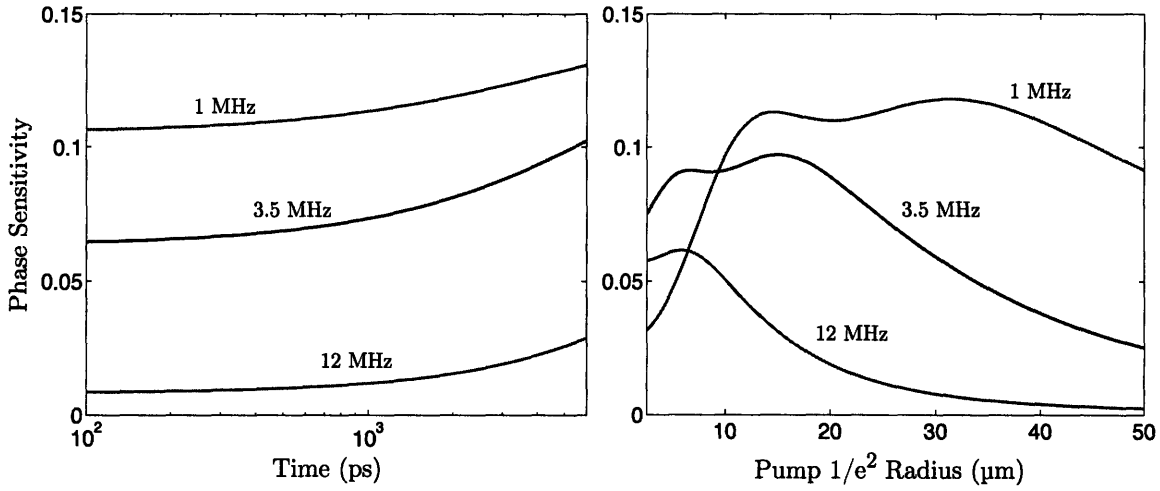

Figure 4-14: Sensitivity of graphite to in-plane thermal conductivity. In the left figure, the probe $1/e^2$ radius is 5 μm and pump $1/e^2$ radius is 25 μm. In the figure on the right, the delay time is fixed at $\tau = 1000$ ps and the probe $1/e^2$ radius is held at 5 μm while the pump radius is varied.

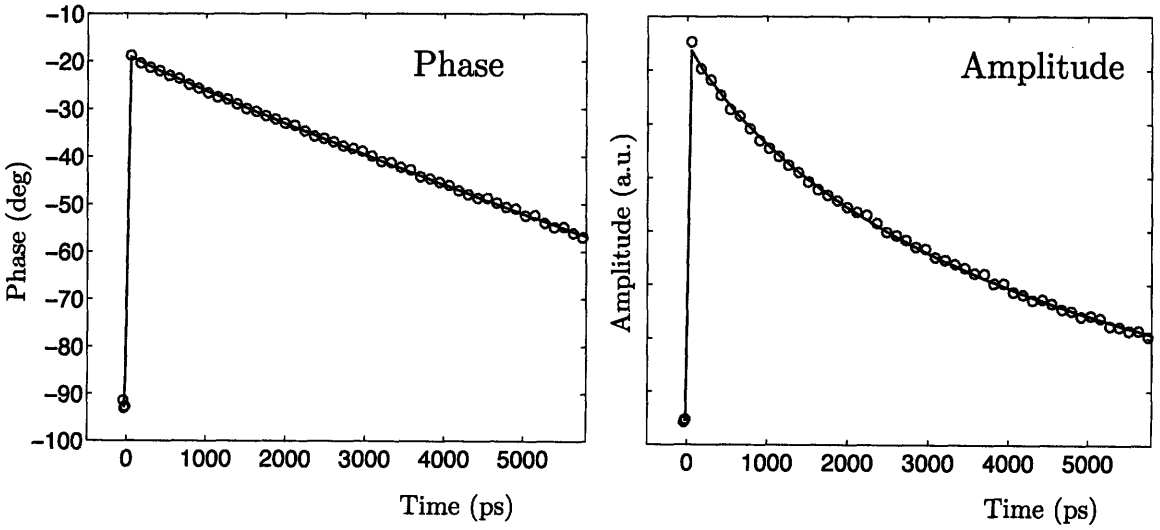

Figure 4-15: Phase and amplitude data for HOPG, along with best fit curves, at a modulation frequency of 11.6 MHz, a probe radius of 5 μm and a pump radius of 50 μm.

compared to the pulse period, the signal begins to approach the frequency response at the modulation frequency. This is apparent in Fig. 4-16, where the phase angle of $H(\omega_0)$ is indicated at each frequency.

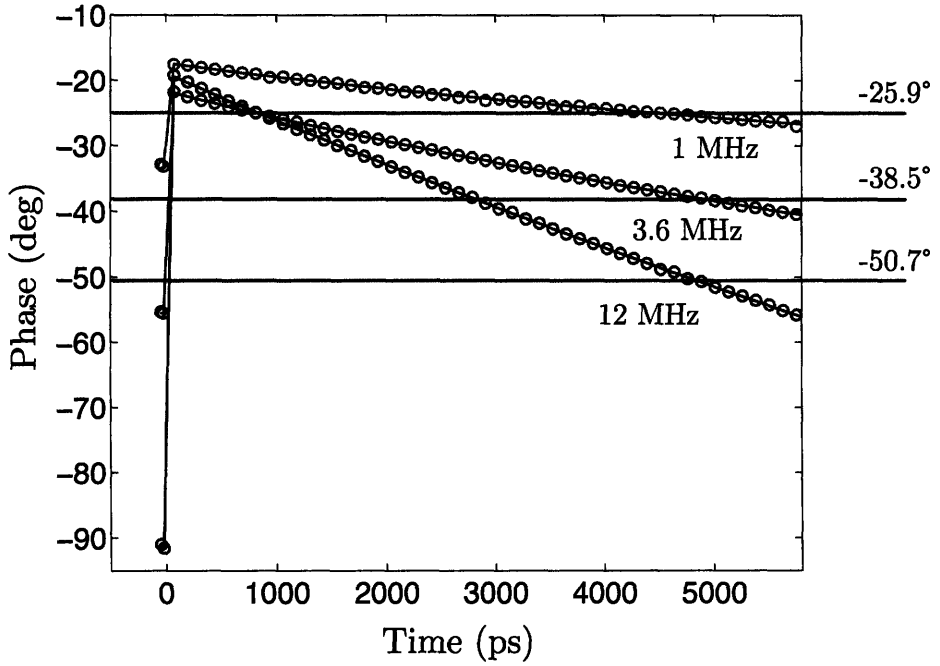

Figure 4-16: HOPG data and best fit curves at three frequencies. The pump spot radius is 26 μm and the probe radius is 5 μm. Values of the phase angle of $H(\omega_0)$ are indicated at each frequency.

From the sensitivity analysis shown in Fig. 4-14, with a 26 μm pump radius we expect the measurement to be somewhat sensitive to in-plane conductivity at 3.65 MHz and more sensitive at 1.11 MHz. In Fig. 4-17, we plot the data and best fit curves at both frequencies, and also the solutions obtained by varying the in-plance conductivity by $\pm 20\%$. The cross-plane conductivity and interface resistance values are taken from the high frequency measurement shown in Fig. 4-15.

The best-fit value obtained for the in-plane thermal conductivity at 3.6 MHz is 1875 W/mK, 4% lower than the literature value of 1950 W/mK [63]. At 1.11 MHz the value is 2034 W/mK, 4% higher than the literature value. This discrepancy could arise from small non-idealities in spot geometry which would manifest themselves differently at different frequencies, or simply from measurement error due to the

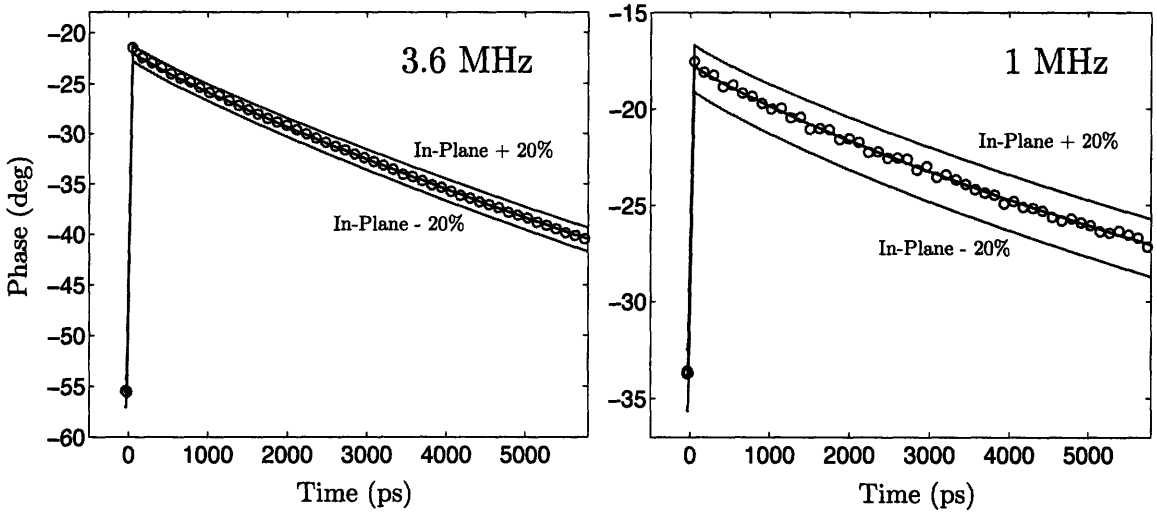

Figure 4-17: HOPG data and best t curves at 3.6 MHz (left) and 1 MHz (right). Solutions obtained by varying the in-plane thermal conductivity ±20% are also shown.

different amount of noise and level of sensitivity at each frequency. The results for HOPG are summarized in Table 4.1.

Table 4.1: Results for HOPG at 300 K

Property	Frequency	Pump Radius	Measured	Literature [63]
σ_z	11.65 MHz	50 μm	5.72 W/mK	5.7 W/mK
σ_r	3.65 MHz	25 μm	1875 W/mK	1950 W/mK
σ_r	1.11 MHz	25 μm	2034 W/mK	1950 W/mK

4.2.2 SiGe Superlattices

In the previous section, we demonstrated the ability to measure in-plane thermal conductivity and produced results that matched well with literature values. Now we turn to a more difficult sample which illustrates the potential and also the limitations of this technique. The sample is a superlattice (SL) comprised of hundreds of alternating layers of Si and $Si_{0.7}Ge_{0.3}$. The basic unit cell is illustrated in Fig. 4-18.

Such structures have been extensively studied both theoretically and experimentally due to their potential value as thermoelectric materials [75] and as unique systems for characterizing phonon transport [76]. Because the superlattice films are typ-

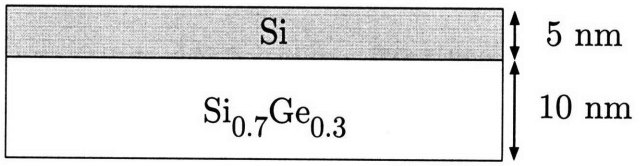

Figure 4-18: Unit cell of our $Si/Si_{0.7}Ge_{0.3}$ superlattice

ically thin, the majority of thermal measurements have been made in the cross-plane direction [77, 78]. In-plane thermal measurements are considerably more difficult because the contribution of the substrate must be subtracted from the measurement, and data for in-plane thermal conductivity are scarce [75]. Typical values for cross-plane thermal conductivity at room temperature range from roughly 1–4 W/mK, depending on the alloy composition and period of the layers [77]. For one particular SL, Si(80 Å)/Ge(20 Å), the measured cross-plane thermal conductivity was 2 W/mK while the in-plane conductivity was 5× higher [75]. Theoretically, the ratio of thermal conductivities has been estimated as between 2–12×, depending on the period and phonon reflection properties at the layer interfaces [76].

Although we would like to simply apply the same experimental approach to this sample that we did for HOPG, we are hindered by the fact that the cross-plane thermal conductivity is low, and the anisotropy ratio is 10× smaller, so the measurement will not be sensitive using the same experimental parameters. In order to measure the in-plane properties, we need to reduce both the laser spot sizes and the modulation frequency. Unfortunately, when the spots sizes become small enough to achieve the necessary sensitivity to the in-plane conductivity, the measurement becomes extremely sensitive to the spot size. Figure 4-19 show the sensitivity to the anisotropy ratio, σ_r/σ_z, and also the sensitivity to the pump spot radius, where the sensitivity here is the phase sensitivity as defined in Eq. (3.54). The cross-plane thermal conductivity is assumed to be 2 W/mK and the in plane thermal conductivity is assumed to be 10 W/mK. The probe $1/e^2$ radius is taken as 2 μm while the pump radius is varied.

As the figure shows, the measurement is 4–5× more sensitive to spot size than

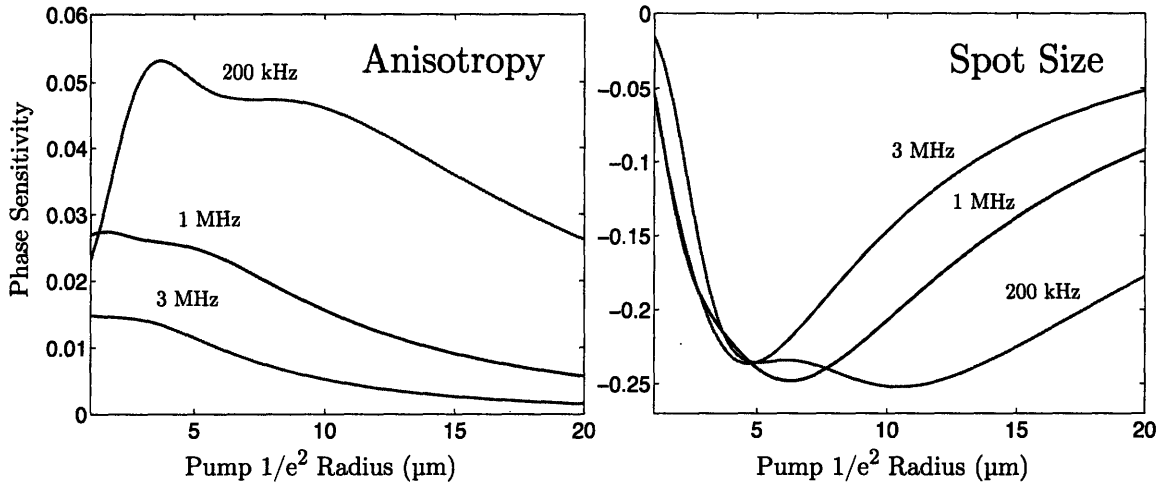

Figure 4-19: Sensitivity to the anisotropy ratio, σ_r/σ_z (left), and the sensitivity to the pump radius (right). The probe $1/e^2$ radius is taken as 2 μm while the pump radius is varied.

the anisotropy ratio for this sample. Sensitivity to thermal anisotropy is greatest when the pump radius is small, around 2–3 μm. We also see that the sensitivity to anisotropy increases with decreasing frequency for small pump sizes, while sensitivity to spot size does not change significantly with frequency when both spots are small. Therefore, our best hope is to make the measurements with low frequency and small spots. This is counterbalanced by the fact that the signal-to-noise ratio of our system degrades at lower frequencies, and also by the fact that measuring beam radii below 4 μm is unreliable with our current beam profiler.

Therefore, we adopt the following procedure for this measurement. First, we perform a "normal" cross-plane thermal measurement on the sample, using a high frequency and a large pump spot, to obtain the σ_z and G. Next, we change the focusing lens to a 50× objective and focus the spots to ~ 2 μm radii, as determined roughly by the beam profiler. We use this arrangement to measure a known isotropic sample (usually thermal SiO_2), and then adjust the beam radius in our model to match the data, essentially fitting the beam radii using the thermal signal. From Eq. (3.50), we see that the pump and probe radii do not act independently; as a result, we can use a single effective beam radius, $w_{\text{eff}} = \sqrt{w_0^2 + w_1^2}$, to characterize the system. Using the beam radius obtained in this way and the cross-plane properties

from the high-frequency measurement, we perform a third measurement, using the 50× objective and a low frequency, 200 kHz. The measurement process is depicted graphically in Fig. 4-20.

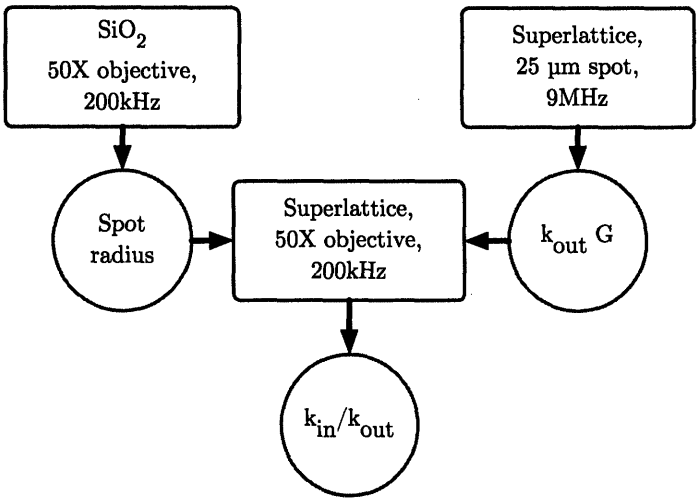

Figure 4-20: Measurement procedure for obtaining in-plane thermal properties from an $Si/Si_{0.7}Ge_{0.3}$ superlattice

The result from the high-frequency measurement with a 25 μm pump radius is show in Fig. 4-21. The best-fit cross-plane thermal conductivity obtained is 1.7 W/mK and the thermal interface resistance is $\sim$ 200 MW/m^{2}K. Figure 4-22 shows the second step in the process, fitting the effective spot radius using a piece of thermal SiO_2. The best fit $1/e^2$ diameter, 4 μm, is indicated, along with the curves produced by varying the diameter by $\pm$20%. Finally, in Fig. 4-23, we show the data and best fit curve for the in-plane thermal conductivity using the results from the previous two measurements. The best fit value is 18.7 W/mK, or 11× the cross-plane thermal conductivity. This is also more than 2× the anisotropy reported by Yang et. al. [75], although it is a different superlattice system.

Limitations

While this result is interesting, its accuracy is questionable. As we showed in Fig. 4-19, the result is 5× more sensitive to spot size than to the in-plane thermal conductivity. Roughly speaking, a spot-size error of 10% (just 200 nm) translates into a 50% error

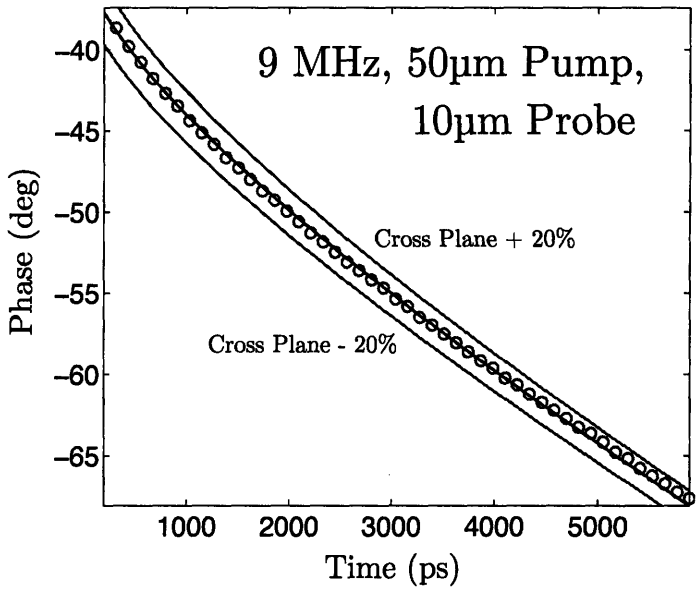

Figure 4-21: Cross-plane thermal conductivity measurement of the $Si/Si_{0.7}Ge_{0.3}$ superlattice. The measured value is 1.7 W/mK and the thermal interface resistance is ~ 200 MW/m^{2}K.

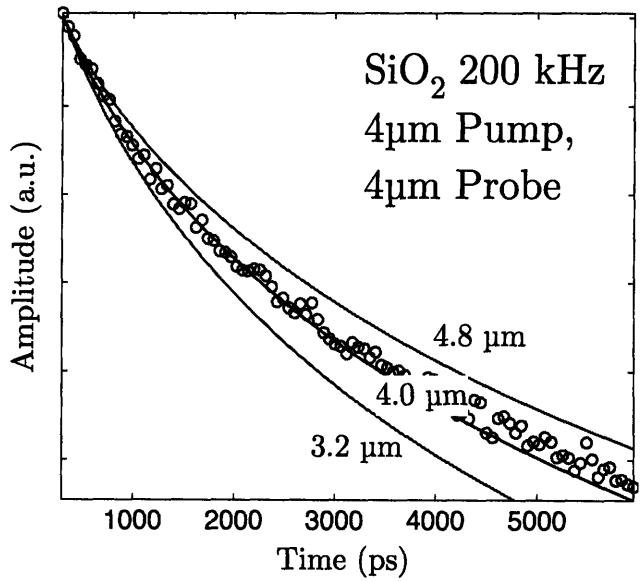

Figure 4-22: Fit of the effective spot radius using a piece of thermal SiO_2. The best fit $1/e^2$ diameter, 4 μm, is indicated, along with the curves produced by varying the diameter by $\pm 20\%$

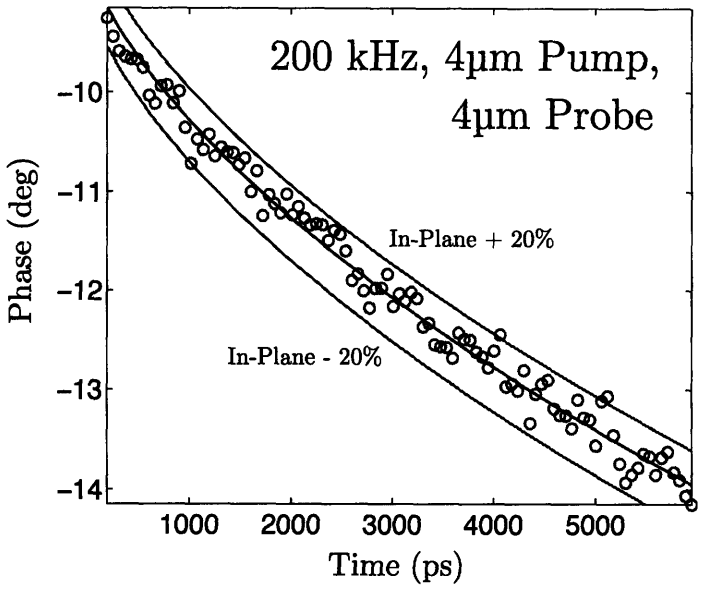

Figure 4-23: Data and best fit curve for in-plane thermal conductivity of the $Si/Si_{0.7}Ge_{0.3}$ superlattice, obtained using a 50× objective and a modulation frequency of 200 kHz. The best fit value for σ_r is 18.7 W/mK.

in σ_z. In addition, although strictly speaking we only calculated the sensitivity to spot diameter in Fig. 4-19, at low frequency and small spot size we would expect the measurement to be similarly sensitive to to spot misalignment, and eccentricity of the spot shape. These effects compound and make it difficult to obtain anything other than an order-of-magnitude estimate on the in-plane thermal conductivity. The results could be made more compelling if a series of measurements were made while varying one parameter systematically, such as the superlattice period or alloy composition.

4.3 Characterization of Microstructures

Now we touch on the possibilities of using the pump-probe technique for characterizing microstructures. We take as an example a zinc oxide (ZnO) belt approximately 30 μm wide and several mm long. The thickness is on the order of a few microns, as we will see later. The belts were grown via molten-salt-assisted template-free thermal evaporation at Boston College [79]. While this section deals with structures

that are a few microns or more in all dimensions, the technique could potentially be extended to nanostructures which are of scientific and commercial interest. Zinc oxide nanostructures, for example, have potential applications in optoelectronics, sensors, transducers and biomedical sciences [80].

An image of a ZnO belt coated with 80 nm of Al is shown in Fig. 4-24. For scale, a human hair is shown under the same magnification. One of the primary difficulties in obtaining a clean, stable signal from the sample was the poor surface quality of the samples; the low reflectivity of the samples made the reflected probe signal weak and also increased the absorption in the sample, limiting the input power to prevent burning of the sample. The surface of the belt shown in Fig. 4-24 was sufficiently reflective to obtain a clean signal.

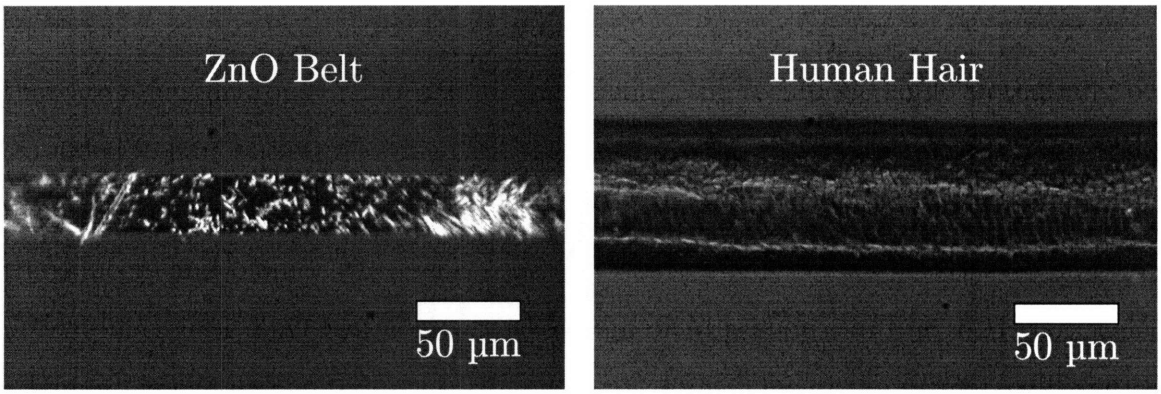

Figure 4-24: An image of a ZnO belt (left), and for scale a human hair is under the same magnification (right).

The pump and probe beams were focused onto the sample using the CCD camera as a guide. An image of the beams focused onto the sample is shown in Fig. 4-25. The probe spot was 10 μm in diameter and was fully contained on the belt, but the pump spot had a diameter of 50 μm and was not. The pump spot was kept large to reduce errors in misalignment and to prevent burning of the sample that would result from focusing the beam too tightly.

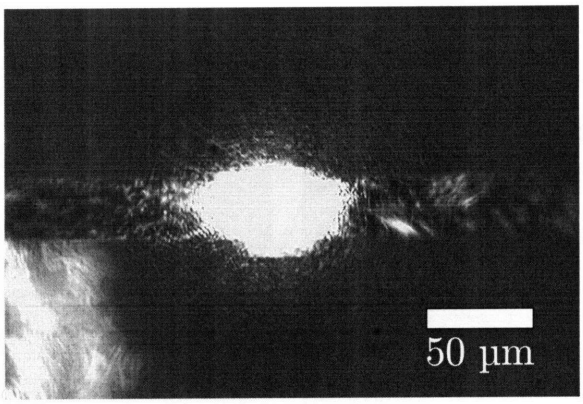

Figure 4-25: The pump and probe spots focused onto the ZnO belt. The pump spot diameter is 50 μm and is not fully contained on the belt.

4.3.1 Thermal Properties

A signal obtained from a ZnO belt is shown in Fig. 4-26. The general decay of the signal can be used to obtain the thermal conductivity of the sample, while the periodic ripples can be used to obtain structural properties, as we see in the following section.

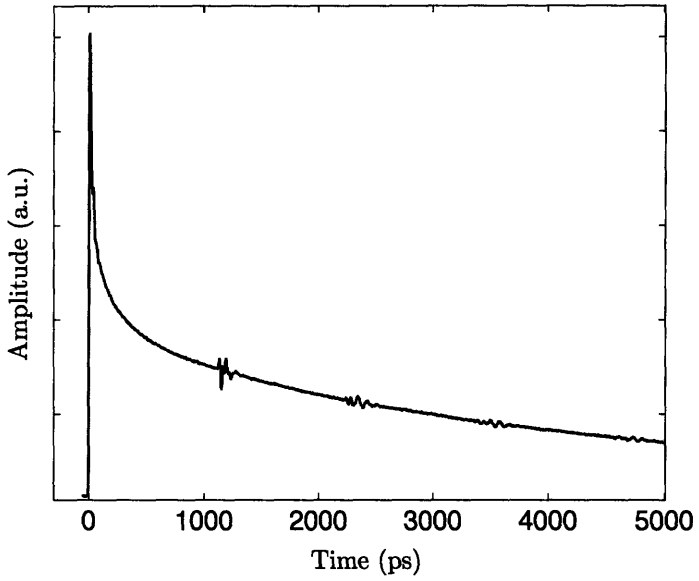

Figure 4-26: Signal obtained from a ZnO belt.

We apply the method described in the previous chapter to fit the cross-plane thermal conductivity of the belt. The best fit of the amplitude data is shown in Fig. 4-27, and the thermal conductivity is found to be 7.3 W/mK. The reported thermal conductivity value of bulk ZnO is 14–35 W/mK, depending on the porosity [81], although the thermal properties are a strong function of the synthesis process [82], and it is not surprising that these structures have a lower conductivity.

The phase data is shown in Fig. 4-28, along with the calculated curve. In this case, the agreement is poor. This is not surprising since the pump spot is larger than the width of the belt. As we saw, the phase is sensitive to radial effects and the lack of cylindrical symmetry in our experiment makes it impossible to obtain consistent fits of both the amplitude and phase data using a mathematically symmetric solution. The problem would potentially be solved by focusing the pump beam more tightly onto the belt, although a better surface quality would probably be needed to limit

localized heat generation that could burn the sample.

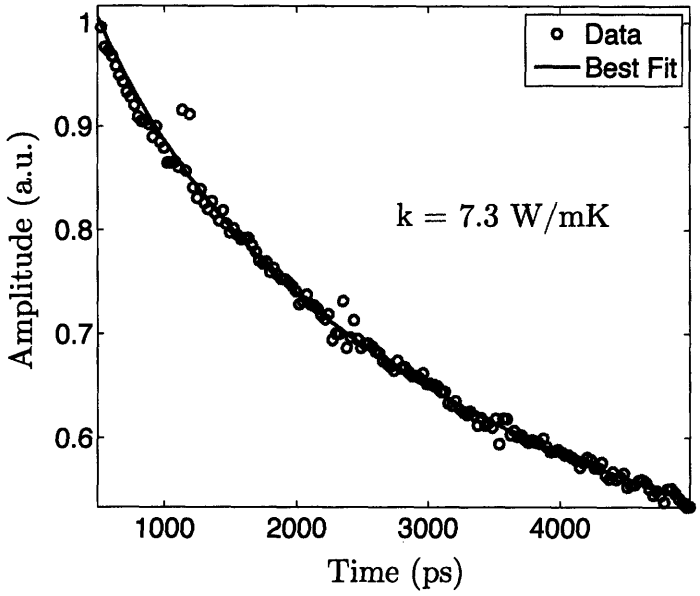

Figure 4-27: Amplitude data and best fit curve for the ZnO belt.

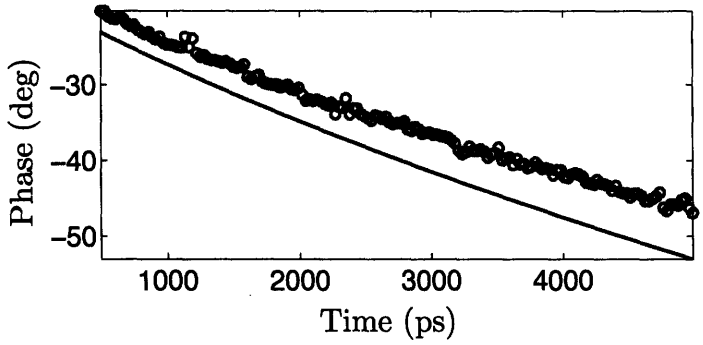

Figure 4-28: Phase data for the ZnO belt and the calculated result using a thermal conductivity of 7.3 W/mK.

4.3.2 Mechanical Characterization

A series of periodic disturbances are visible in the signal shown in Fig. 4-26. These are the result of an acoustic impulse making round-trips through the thickness of the belt. Conceptually, the situation is similar to that in the Al film described in Section3.7.2. Here, however, the acoustic signal is more complex because the echo signal caused by the Al-ZnO interface travels through the thickness of the belt and is transmitted back through the interface, causing additional ripples. The initial impulse signal from the Al film and the reflected pulse after one round-trip through the belt are shown in Fig. 4-29

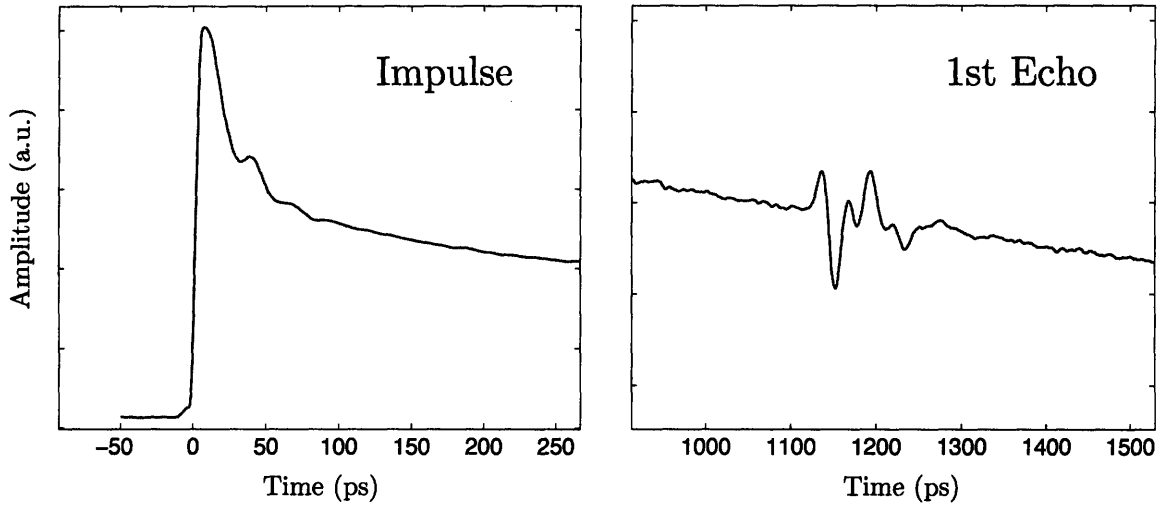

Figure 4-29: The initial impulse signal from the Al film (left) and the reflected pulse after one round-trip through the belt (right).

While a detailed analysis of the pulse shape and dispersion of its Fourier components after multiple round-trips is outside the scope of this thesis, it is simple to use the period between echos to estimate either the elastic properties of the belt or its thickness. The longitudinal sound speed in an elastic isotropic solid is given by [83]

$$v_s = \sqrt{\left(K + \frac{4}{3}\mu\right)/\rho} \tag{4.8}$$

where K is the bulk modulus, μ is the shear modulus and ρ is the density. If the Young's modulus, E, and Poisson ratio, σ, are known, then the bulk and shear

modulus can be found from

$$\begin{aligned} K &= (1/3)E/(1-2\sigma) \\ \mu &= (1/2)E/(1+\sigma) \end{aligned} \tag{4.9}$$

Since each disturbance in the signal is the result of one round-trip of the pulse through the film, the period between pulses, t_{echo}, is related to the thickness of the sample, d, through Eq. (3.56), which we repeat here for convenience:

$$d = \frac{1}{2} t_{\text{echo}} v_s \tag{4.10}$$

If the thickness of the sample is known from an independent method, such as a scanning electron microscope (SEM) image, then Eq. (4.10) can be used to extract the sound speed. In our case, the thickness of the sample in unknown, so we assume the room temperature sound speed of bulk ZnO, 6015 m/s [81], and estimate the thickness as 3.55 μm. The process is depicted graphically in Fig. 4-30. While this result is not in itself particularly interesting, it highlights the potential of the technique for the characterization of the thickness of microstructures.

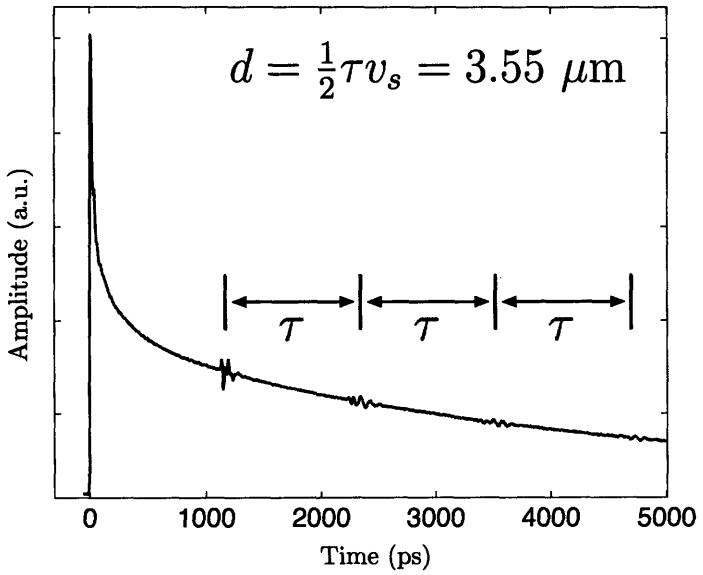

Figure 4-30: Determination of the thickness of a ZnO belt using acoustic echos.

4.4 Summary

Three applications of the pump-probe technique have been described, building on the foundation of the previous chapter. The first is a new approach for measuring the thermal conductivity of liquids, greases and pastes which has unique advantages over existing methods, notably the ability to measure liquid films as thin as a few hundred nanometers, with no dependence on the optical properties of the liquid itself. Results spanning the range of commonly encountered liquid thermal conductivities were presented as validation of the method.

The second major application is the measurement of both cross-plane and in-plane thermal properties through a variation of the spot size and modulation frequency. The technique was successfully demonstrated on highly ordered pyrolytic graphite, verifying that the idea is sound. Following this, the approach was applied to a SiGe superlattice structure. The low thermal conductivity and modest anisotropy compared to HOPG required the use of 2 μm pump and probe radii and a 200 kHz modulation frequency to obtain sufficient sensitivity. Under these conditions, spot size uncertainty and signal noise limited the accuracy of the in-plane thermal conductivity to a rough estimate and highlighted the technique's limitations.

Finally, in the last section we touched upon the possibilities for the characterization of microstructures using a ZnO belt structure 30 μm wide and several mm long as an example. The thermal conductivity of the belt was measured as 7 W/mK and the thickness, characterized using acoustic echos, was found to be 3.55 μm.

Chapter 5

Experimental Investigations of Nanofluids

5.1 Introduction

In this chapter, we turn to the topic of nanoparticle-seeded fluids, or "nanofluids," a topic which has received considerable attention in recent years [11, 48], and approach the topic from two different perspectives: (1) heat transfer between an individual nanoparticle and the surrounding fluid, and (2) the bulk thermal and viscous properties of the suspension. For the first case, we use the same pump-probe system described in the previous chapters, reconfigured for transmission geometry rather than reflection. In the second case, we use a different optical technique, impulsive stimulated thermal scattering (ISTS) [49], which belongs to a class of techniques known as transient grating (TG) methods. The experimental apparatus for this measurement was constructed by students in the Keith Nelson group in the Department of Chemistry at MIT.

5.2 Transient Absorption of Gold Nanorods

Gold nanorods (Au NRs) are ideal candidates for studying the thermal interaction between a nanoparticle and its surroundings for several reasons. Absorption and scat-

tering of electromagnetic radiation by noble metal nanoparticles are strongly enhanced due to surface plasmon (SP) resonance, the collective oscillation of conduction-band electrons in the nanoparticles [84]. The frequency of the SP resonance depends on the size and shape of the nanoparticles as well as their dielectric constant and that of the surrounding medium. The size and aspect ratio of the rods can be precisely controlled through chemical synthesis techniques, making it possible to create rods with a strong absorption peak that matches a particular wavelength. As we discuss in the next section, our rods were created to have an SP resonance at 800 nm, our probe wavelength, allowing for a good signal to noise ratio. In addition, Au NRs are interesting in their own right because they are bio-compatible and have potential applications as biological imaging agents and for photo-thermal cancer therapy [85].

5.2.1 Sample Preparation and Experimental Setup

The basic experimental setup discussed in Chapter 2 and shown schematically in Fig. 2-1 is unchanged, with the exception that the reflective sample is replaced with a suspension of Au NRs in deionized H_2O, and a blue filter and detector have been placed behind the sample. The suspension was contained in a cuvette 1 mm thick and typically contained Au NRs in concentrations of 1 nM. The typical laser fluence at the sample was $\sim$2 J/m^2. As with the reflection measurements discussed in Section 3.8, increasing or decreasing the laser fluence did not alter the shape of the curve, only its amplitude, indicating that we are not perturbing the sample beyond the linear regime. The sample arrangement is shown in Fig. 5-1.

Gold nanorods were prepared in the Hamad-Schifferli Group at MIT according to a modified protocol of the non-seeding method described in [86]. Briefly, $HAuCl_4$:$3H_2O$ and $AgNO_3$ are added to a CTAB containing saline solution which turns yellow upon inversion. L-ascorbic acid is added, and the solution turns clear. Next, $NaBH_4$ is added, and the solution is again mixed by inversion. On the time scale of hours, the solution turns from clear to a deep purple brown. After at least three hours of room temperature incubation, the excess reactants are washed from the solution. Finally, the Au NRs are concentrated by centrifugation. All chemicals used were

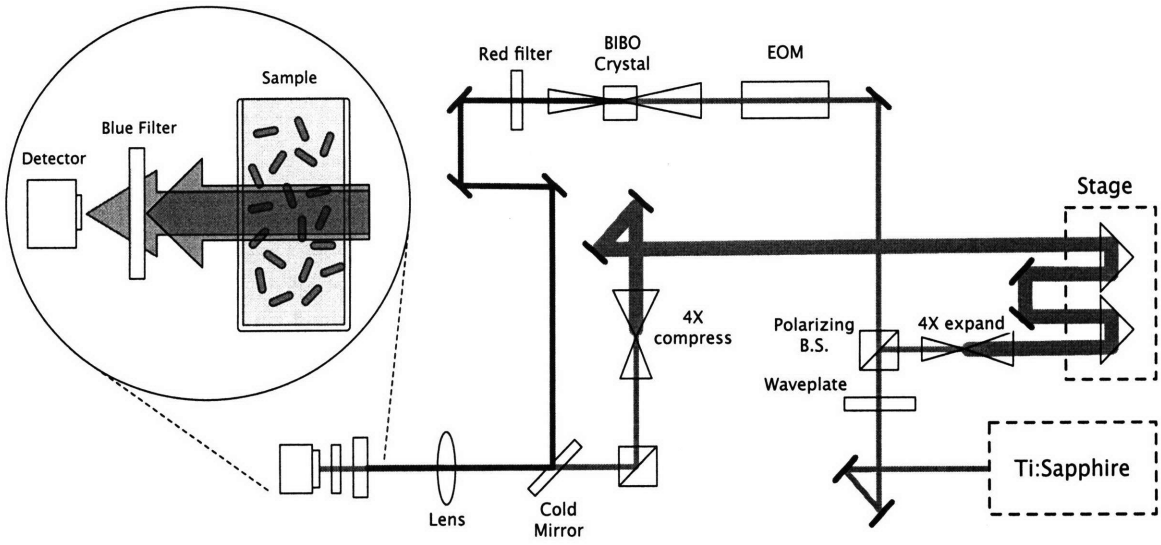

Figure 5-1: Experimental setup for transmission geometry.

purchased from Sigma Aldrich Co. and used without further purification. CTAB is used in the synthesis of gold nanorods to direct the preferential growth along the length of the nanorod. It is hypothesized that the amine headgroups coordinate more strongly to certain facets of gold nanoparticles, directing the growth along the [110] crystal direction during nanorod synthesis [87]. This leaves the hydrophobic tails of the CTAB protruding from the surface of the nanorods. If there is presence in enough quantity, free CTAB coordinates with these tails to form bilayers around the nanorods. This likely occurs near the critical micelle concentration of 1 mM [88, 89]. The CTAB bilayer then serves to stabilize the Au NRs in solution, preventing their aggregation by a combination of steric and electrostatic effects.

Transmission electron microscope (TEM) imaging shows (Fig. 5-2(a)) that the Au NRs are 10.3 $\pm$2.6 nm in diameter and 34.9$\pm$7.4 nm long with an average aspect ratio of 3.5:1. These Au NRs were synthesized to have a strong SPR for wavelengths near 800 nm [84]. This is confirmed by measured absorption spectra, shown in Fig. 5-2(c).

A ligand molecule is required to prevent the Au NRs from agglomerating and falling out of solution. In our case, we used the ligand cetyl trimethylammonium bromide (CTAB), which is commonly used in the synthesis process [90]. CTAB is a

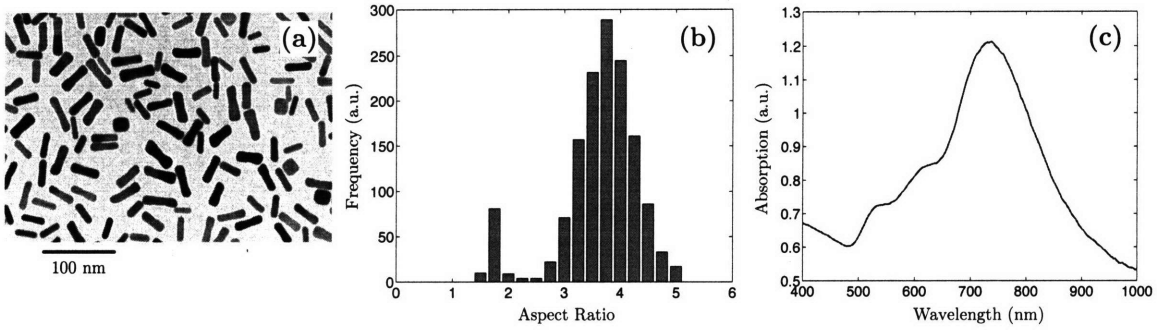

Figure 5-2: Gold NR characterization. (a) TEM image of Au NRs. (b) Absorption spectra of Au NRs in 10 mM CTAB with longitudinal SPR peak at 768 nm. (c) Distribution of Au NR aspect ratios. Mean = 3.7 Standard Deviation = 0.5 Yield = 93%. Note that an Au NR is defined to have an aspect ratio greater than 1.75. Otherwise, it is considered a sphere.

cationic surfactant with a hydrophilic "head" region and a hydrophobic "tail" region. In aqueous solutions, CTAB forms micelles, aggregates in which the head regions are in contact with the solvent while the tail regions are sequestered in the center. In addition, above a critical concentration, CTAB forms a bilayer sheet on the surface of gold nanocrystals [91, 92], which is estimated to be ~4 nm thick [92]. Illustrations of both the bilayer state and a micelle are shown in Fig. 5-3.

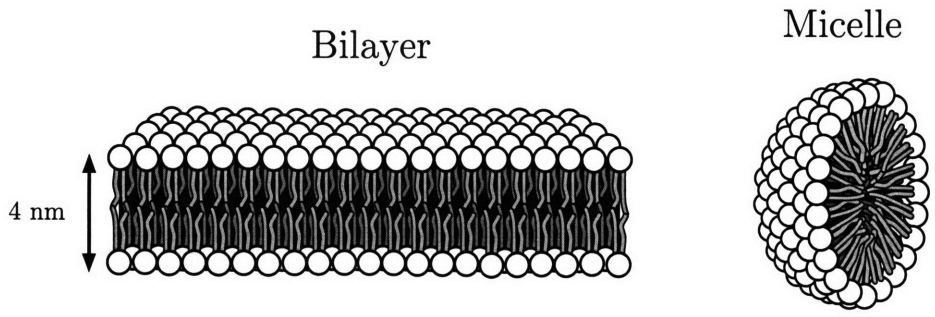

Figure 5-3: Bilayer state and a micelle structures formed by CTAB above a critical concentration. (Image courtesy of Wikipedia Commons, `http://en.wikipedia.org/wiki/Image:Phospholipids_aqueous_solution_structures.svg`)

5.2.2 Results

A typical absorption signal obtained during measurement is shown in Fig. 5-4. There are several distinct energy transfer regimes for an Au NR following excitation by an ultra-short pulse of light [93]. Initially, the there is a fast electron bleaching process which relaxes within one picosecond, followed by a period of electron-phonon non-equilibrium similar to the one described in bulk metals in Section 1.2.1, which can last a few picoseconds. This followed by a coherent vibrational response of the rod, which is dominated by the longitudinal extensional mode of the rod. The period T is given by [93, 94]

$$T = \frac{2L}{\sqrt{E/\rho}} \tag{5.1}$$

where E is Young's modulus, ρ is the density and L is the length of the rod. Inserting the values for bulk gold and 37.5 nm for the length of the rod, we find $T = 37$ ps, in good agreement with the observed period shown in Fig. 5-4. This is followed by a long tail of thermal diffusion which is sensitive to the size of the rod, the surrounding fluid and the thermal interface between the two. Here we focus on the thermal diffusion regime, and in particular the role that CTAB plays in the heat transfer process.

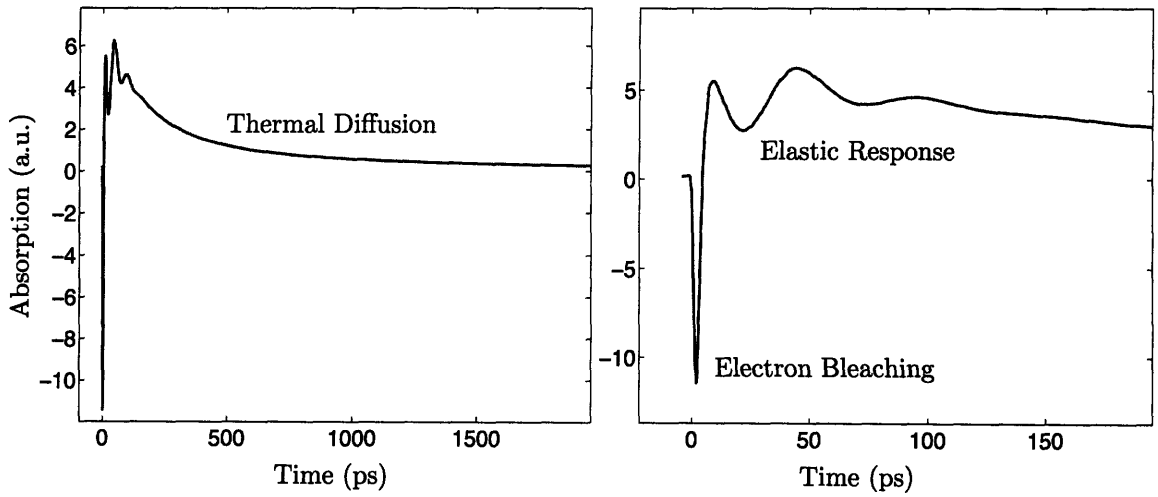

Figure 5-4: Absorption signal of a gold nanorod to an ultrashort pulse of light. The rapid electron bleaching is followed by electron-phonon non-equilibrium and coherent vibration. Eventually the deposited energy is transferred to the surrounding fluid via thermal diffusion.

Measurements were made on 1 nM suspensions of Au NRs in deionized water with varying concentrations of CTAB to systematically study the role of ligand in the heat transfer process. Suspensions with CTAB concentrations from less than 1 mM to 300 mM were studied. Because of the synthesis process, it was not possible to remove 100% of the CTAB from the rods, so even at 0 mM concentration a small amount remained. Above 300 mM, the CTAB crystallized rapidly, making it impossible to obtain stable measurements.

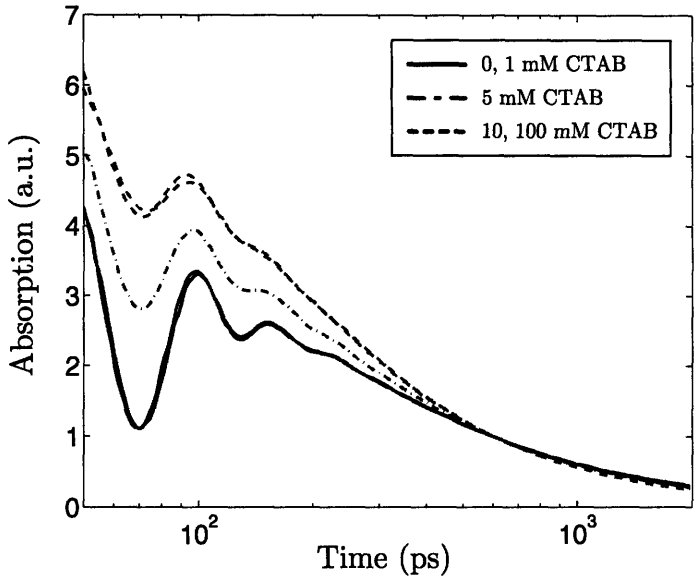

Figure 5-5: Cooling curves for CTAB concentrations up to 100 mM. There is clear transition in the cooling behavior that occurs between 1 mM and 10 mM of CTAB. For concentrations of 1 mM and below the initial excitation is smaller and the thermal decay is slower, while for concentrations of 10 mM the initial excitation is larger decays at a faster rate. At 5 mM, the rod cools in an intermediate way.

A subset of the results are shown in Fig. 5-5. All curves have been normalized to the absorbance at 600 ps. A clear transition in the cooling behavior of the nanorods occurs between 1 mM and 10 mM concentrations of free CTAB. For concentrations of 1 mM and below, the initial excitation is smaller and the thermal decay is slower, while for concentrations of 10 mM and above, the initial excitation is larger and it decays at a faster rate. At 5 mM, the rod cools in an intermediate way. The transition in behavior corresponds to the critical micelle concentration and thus can be attributed to the formation of a stable CTAB bilayer on the nanorod.

5.2.3 Analysis

To calculate the heat transfer properties of the CTAB layer, we fit the data in Fig. 5-5 to a transient continuum model for heat conduction from the nanorod to the surrounding liquid. We use a two-dimensional axisymmetric numerical model to carry out this analysis, consisting of the rod, a layer of CTAB, and a region of surrounding water sufficiently large to be essentially infinite. We take the CTAB layer thickness as 4 nm, corresponding to the approximate thickness of a CTAB bilayer [92], and the volumetric heat capacity as $2\text{x}10^6$ J/m^{3}K, a value characteristic of lipid bilayers in the gel phase [95], although the results are relatively insensitive to this property. We note that this approach accounts for the thermal mass of the ligand layer in the transient cooling process, and also essentially lumps together the thermal conductance of the layer with the ligand-fluid thermal interface conductance.

In order to avoid numerical difficulties associated with working with very small numbers, the cylindrical diffusion equation was non-dimensionalized using the following definitions:

$$\begin{aligned} \zeta &\equiv \frac{\alpha_s t}{L_c^2} \\ \eta &\equiv \frac{r}{L_c} \\ \mu &\equiv \frac{z}{L_c} \end{aligned}$$

Here α_s is the thermal diffusivity of some scaling material (which in this problem will be taken to be water), and L_c is some characteristic scaling length for the from (for example, 10 nm is a good choice here.) Using these definitions the heat equation becomes

$$\frac{\partial}{\partial \eta}\left(k_n \eta \frac{\partial T}{\partial \eta}\right) + k_n \eta \frac{\partial^2 T}{\partial \mu^2} + L_c^2 \eta q = \eta \alpha_s (\rho c)_n \frac{\partial T}{\partial \zeta} \tag{5.2}$$

The boundaries and mesh of our dimensionless numerical model are shown in Fig. 5-6

The laser pulse delivers an impulse of strength Q. Numerically, this is treated as time dependent heat generation term with some appropriate shape, such as a gaussian pulse with a standard deviation $\sigma = 0.5$ ps. If the total energy contained in the pulse

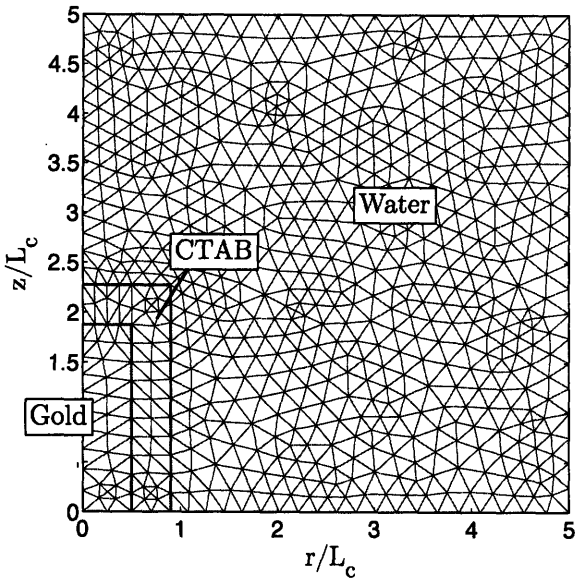

Figure 5-6: Numerical model used to calculate the transient cooling of a rod.

is Q, then

$$q = \frac{2Q}{\sigma\sqrt{2\pi}} \exp\left(\frac{-t^2}{2\sigma^2}\right) \tag{5.3}$$

The area under Eq. 5.3 integrated from $t = 0$ to ∞ is the total power deposited, Q. In terms of the dimensionless, cylindrical system developed above, we define

$$\sigma' \equiv \frac{\alpha_s \sigma}{L_c^2}$$

Then Eq. 5.3 can be written as

$$q = \frac{2Q}{\sigma'\sqrt{2\pi}} \exp\left(\frac{-\zeta^2}{2\sigma'^2}\right) \alpha_s \eta \tag{5.4}$$

The model was applied to data from each of the three cooling regimes shown in Fig. 5-5. Results for a 50 mM solution, a 5 mM solution and a 1 mM solution are shown in Fig. 5-7(a), Fig. 5-7(b), and Fig. 5-7(c), respectively. For the 50 mM CTAB solution, we find that an effective thermal interface conductance, G, of 130 MW/m^{2}K, produces the best agreement with the data after $\sim$ 300 ps, corresponding to an effective thermal conductivity of the CTAB bilayer of 0.52 W/mK. This result is indicated

in the figure, along with the result obtained by assuming a layer with infinite thermal conductance. For the 5 mM solution the best fit value of G is 200 MW/m^{2}K, and for the 1 mM solution, G = 450 MW/m^{2}K. The initial absorption and cooling are characterized by electron-phonon non-equilibrium followed by a strong elastic response [93]. These effects are not included in our model and so we do not expect good agreement for times less than $\sim$ 300 ps. We performed transient hotwire measurements on the water and surfactant without Au NRs and found the effective thermal conductivity of 50 mM CTAB solution was as much as 10% lower than that of pure deionized water. However, accounting for this produces no significant impact on the calculated interface conductance results.

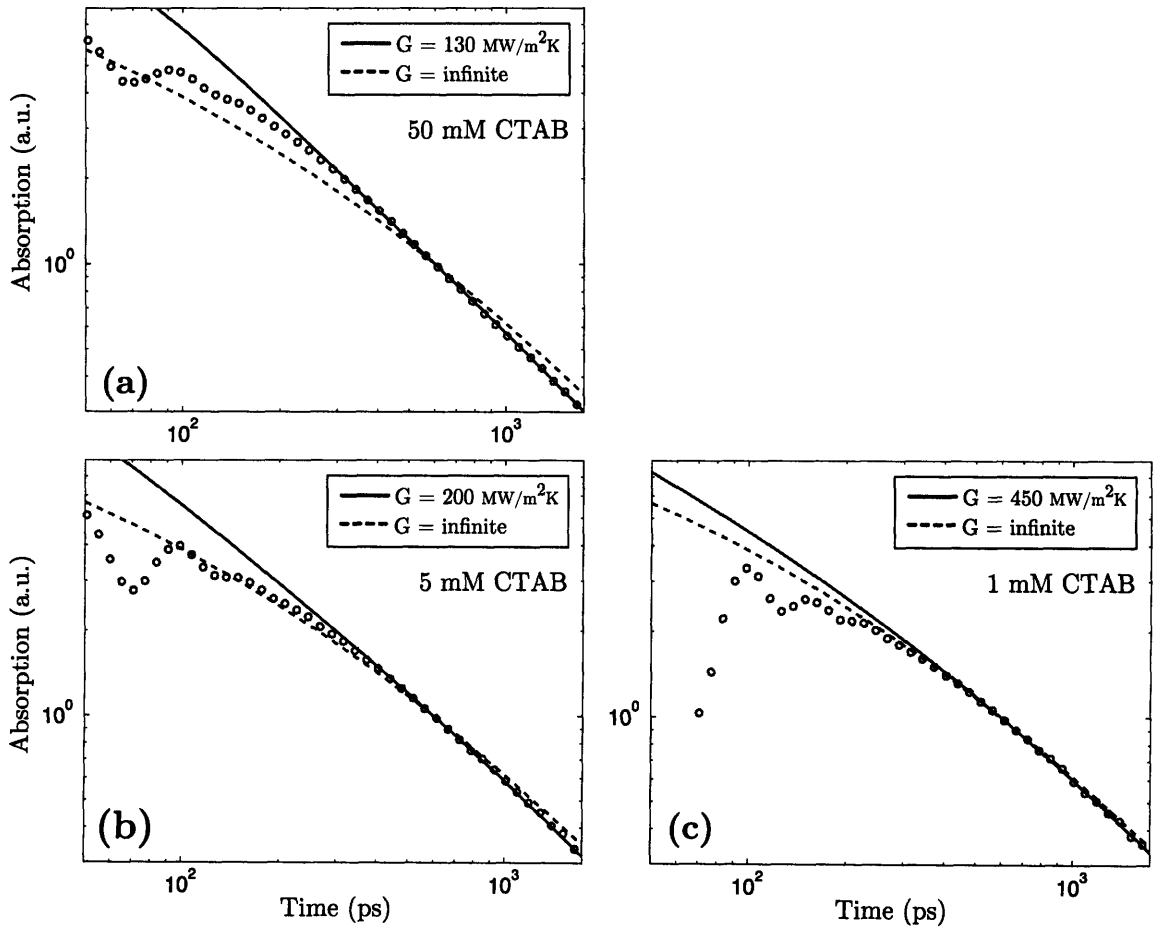

Figure 5-7: Calculated and measured results for the transient cooling in each of the three regimes on log-log plots. In each case the value of the thermal interface conductance, G, that produces the best fit curve after 300 ps is shown, along with the curve obtained assuming infinite thermal conductance for the layer.

We also attempted to fit all of the data using a pure thermal interface conductance (with no thickness or heat capacity) but we were unable to produce good agreement without varying the rod dimensions as a function of CTAB concentration. These results suggested that the rods were aggregating into clusters of 2–4 rods at CTAB concentrations below 10 mM. Dynamic light scattering (DLS) was performed on the suspensions and no such clustering was observed. This indicates that the thermal capacitance of the CTAB layer is necessary to capture the cooling behavior of the Au NRs.

The change in the thermal transport between free concentrations of 1 mM and 10 mM is likely to correspond to a fluid to gel phase transition in the CTAB layer, a well known characteristic of lipid bilayers [95, 96]. Above concentrations of 10 mM, we believe a stable bilayer is formed on the surface of the rod (the gel phase), explaining why increasing CTAB concentration produces no further change in thermal transport. However, below this concentration the lipid layer is in a transition from the fluid phase, and this fluid phase has a higher thermal conductance than the gel phase. For lipid bilayers, the changes in density [95], specific heat [95], and thickness [96, 97] from the fluid phase to the gel phase are sufficiently small that we do not need to vary these parameters in the thermal model. The conclusion that the ligand layer undergoes a phase transition is supported by a shift seen in the longitudinal SPR absorption peak as a function of free CTAB concentration. The peak shift occurs over exactly the same range of CTAB concentration as the change in thermal interface conductance; this result is shown in Fig. 5-8. The frequency of the SPR peak depends strongly on the dielectric constant of the rod and the immediately surrounding medium in addition to the rod size and shape [84], and therefore it is not surprising that a phase change in the CTAB layer would cause the peak to shift.

The implications of this work extend beyond the immediate results relating to our particular Au NR-ligand combination. We have demonstrated that the optical pump-probe technique is a sensitive tool for understanding ligand behavior on gold nanoparticles, and that changes in the ligand layer correlate with the SPR absorption peak. Additionally, we expect the thermal interface conductance of the stable CTAB

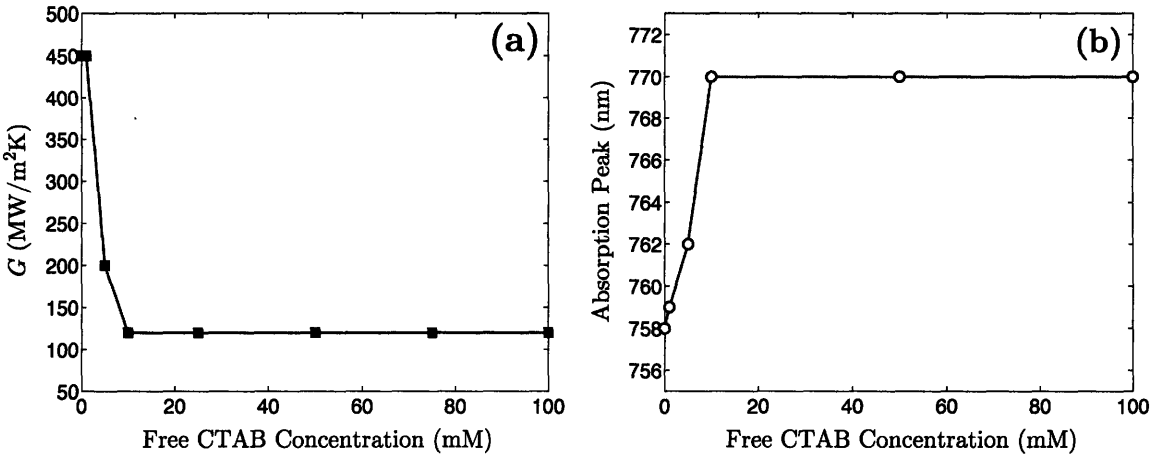

Figure 5-8: (a) Effective thermal interface conductance of the CTAB layer plotted as a function of free CTAB concentration. (b) Surface plasmon resonance peak for solutions of Au NRs over the same range of free CTAB concentrations. The wavelength shift coincides with the change in the thermal interface conductance, indicating a change in the local environment near the gold surface between concentrations of 1 mM and 10 mM.

bilayer of the same order for gold nanoparticles with different geometries, and the fact that the thermal conductance of the ligand layer is a strong function of the concentration of the free ligand near its critical micelle concentration should be applicable to other ligands used to stabilize metallic nanoparticles.

5.3 Bulk Nanofluid Thermal Conductivity Measurements

Now we turn from the behavior of an individual nanoparticle to the effective bulk properties of a solution of nanoparticles. Over the last several years, there has been considerable interest in the bulk thermal behavior of nanofluids. Since the first report on the thermal conductivity and viscosity of such suspensions by Masuda et al. [98], there have been numerous experimental studies on a wide variety of nanofluids comprised of different combinations of solid particles and base fluids. Systems that have been studied include nanoparticles of copper [99], gold [100, 101], and various oxides [102–104] dispersed in base fluids such as water and various organic liquids.

Interest has been fueled primarily by reports of thermal conductivity enhancements significantly greater than predicted by classical models [99, 105]. Compared to models based on the effective medium theory of Maxwell [106], such as the one developed by Hamilton and Crosser [107], nanofluids have been reported to exhibit significantly higher thermal conductivity, anywhere from a few percent higher for solutions of oxide nanoparticles such as Al_2O_3 [102–104], to as much as 40% for Cu-based nanofluids [99].

In addition, it has been observed that in some nanofluid systems, the shear viscosity increases more rapidly than predicted by the Einstein model [108, 109] even at concentrations sufficiently small that the systems are truly dilute [110–112]. Numerous theories have been proposed to account for the enhanced thermal conductivity and shear viscosity, though a consensus has not been reached.

The situation is complicated by the fact that measurements carried out by different research groups often yield conflicting results, and variations in experimental technique, nanofluid synthesis and composition often make direct comparison difficult. For example, in the previous section we showed the strong impact of surfactant on the heat transfer between a particle and its surroundings and on the tendency for the particles to form clusters. Nevertheless, the reports of enhanced thermal conductivity have spawned numerous theories that attempt to account for enhancement over continuum models. Recent reviews [11, 113] have summarized the myriad theoretical efforts and arrive at the conclusion that a clear consensus has yet to be reached. One thing that is clear is that modeling efforts have been far stronger than efforts to resolve the discrepancies between different data sets presented in the literature by various groups. There is clearly a need to resolve these differences and confirm the repeatability of the data obtained by different groups. This can be achieved by reporting the exact details of the nanofluid tested: particle material, base fluid, surfactants used, method of synthesis of nanoparticles, and any possible contamination with other agents. Equally important, the measurement technique must be carefully considered to eliminate sources of systematic error. Reaching a consensus with regard to the experimental data is critically important for an accurate physical model to be developed.

Our focus here is in this direction. In Section 5.3, we describe the synthesis of nanofluids composed of Al_2O_3 particles suspended in $C_{10}H_{22}$ (decane) and isoparaffinic polyalphaolefin (PAO). Then, we present two independent sets of thermal conductivity measurements. One set was obtained using the standard transient hotwire method [71], and the other was obtained with the transient grating (TG) method. The hotwire and TG techniques are sufficiently different that it is unlikely they share common sources of systematic error. As a result, good agreement between the two measurements indicates that the observed enhancement in thermal conductivity can be trusted, and that either method can be a reliable way to measure the thermal conductivity of nanofluids. In Section 5.4, we use the same TG technique to investigate the viscous properties of nanofluids and shed some light on the mechanism behind their enhanced thermal conductivity and shear viscosity.

5.3.1 Sample Preparation

In this chapter we study two nanofluid systems which exhibit enhanced thermal conductivity and shear viscosity: Al_2O_3 (alumina) nanoparticles in $C_{10}H_{22}$ (decane) and isoparaffinic polyalphaolefin (PAO). We chose these nanofluids because hydrocarbon based systems are of potential commercial interest as lubricants with enhanced thermal performance in automotive and other mechanical applications.

The nanofluids were formulated by mixing alumina nanoparticles (Sigma Aldrich) with a mean particle radius of 20 nm with different base fluids: 99.9% $C_{10}H_{22}$ (decane, Alpha Aesar, CAS 124-18-5), and a highly branched isoparaffinic polyalphaolefin (PAO), (Synfluid 4cSt, Chevron Phillips Chemical Company). Figure 5-9 shows an SEM image of the alumina nanoparticles before they are dispersed in the base fluid. The nanofluids were stabilized with 0.25 volume % of sorbitan monolaurate, and the particles were dispersed using an ultrasonic disruptor; a total energy of 5000 J was delivered by a series of 2 s long pulses spaced 5 s apart, with a power density of 2 W/mL. Sonication was performed in an ice bath to maintain a constant temperature in the the suspension.

The thermal conductivity variation of the base fluid due to addition of the surfac-

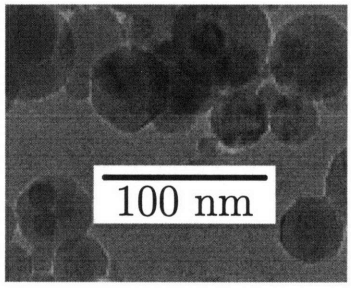

Figure 5-9: SEM image of alumina nanoparticles with a mean particle radius 20 nm.

tants is included during the measurement of the pure base fluid. The nanoparticles are believed to be well dispersed in both PAO and decane due to the fact that the obtained suspensions did not shown any sign of sedimentation over several weeks.

5.3.2 Transient Hotwire System

The transient hot wire method developed by Nagasaka and Nagashima [71] is a well-established technique for measuring the thermal conductivity of liquids, so our description here will be brief. The experimental set up consists of a cylindrical pipe of internal diameter 19 mm and length 190 mm. A thin platinum wire (25 μm) is suspended between two copper electrodes in the center of the pipe. The wire is 150 mm long and is coated with insulation (1.5 μm thick isonel layer) to minimize the leakage of electrical current from the electrodes to the surrounding fluid.

The wire is immersed in the fluid and a constant current is passed through it. The temperature rise of the wire is measured as a function of time, and the thermal conductivity of the nanofluid can be obtained from,

$$k_{nf} = \frac{Q}{4\pi L \frac{dT}{d\ln t}} \tag{5.5}$$

Here k_{nf} is the thermal conductivity of the nanofluid, Q is the total power dissipated in the wire, L is the length of the wire, T is the wire temperature and t is time. The data between 0.1 and 2 s is used to calculate $dT/d(\ln t)$ used in the thermal conductivity calculation. A simulation of a typical temperature rise is plotted in

Fig. 5-10, together with experimental data. As shown in the figure, by using the data between 0.1 and 2 s, the effects associated with the thermal capacitance of the wire at short times and natural convection at long times are avoided.

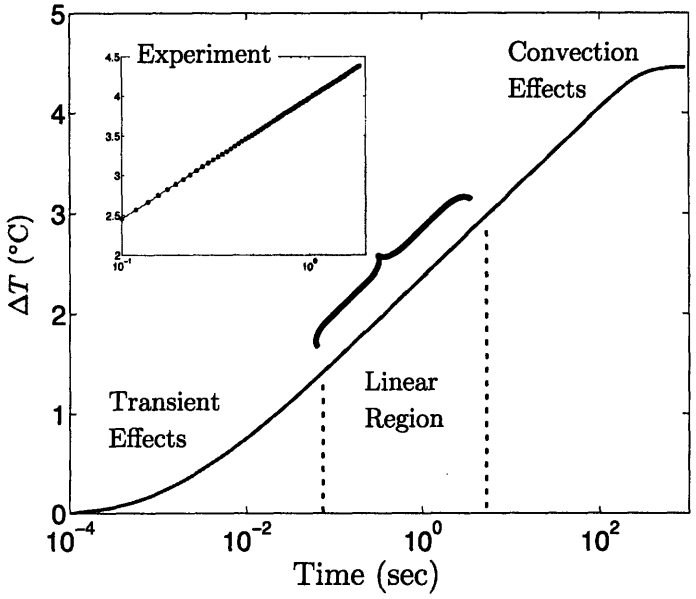

Figure 5-10: Simulation of typical temperature rise measured with the hotwire technique. Inset shows actual data, taken between 0.1 and 2 seconds.

The constant current serves two purposes: it acts as a heat source through electrical dissipation, and it enables the temperature measurement of the wire. In order to measure the temperature rise, the hot wire is incorporated into a Wheatstone bridge which is balanced at the start of the experiment. During the experiment, the change in wire temperature causes a change in wire resistance, leading to a measurable voltage imbalance in the bridge. The temperature coefficient of resistance of the wire is determined by measuring resistance as a function of the temperature of the wire. Subsequently, the temperature rise of the wire is calculated from the change in wire resistance data and using the determined temperature coefficient of resistance. By measuring the slope of the temperature rise versus log of time curve and using Eq. 5.5, the thermal conductivity of the nanofluid is measured.

The system was calibrated by comparing the measured values of thermal conductivity for deionized water, decane and ethylene glycol against literature values.

Our experimental setup allows us to obtain measurements both in a horizontal and vertical configuration to asses whether the stability of the suspension affects our measurement [114]. The literature values of the base fluids were reproduced with an uncertainty of 0.5%. The thermal conductivity for each volume fraction was measured 15 times over a period of 30 minutes after sonication and the average of the 15 data points is reported in this work. The thermal conductivity measurement did not vary appreciably over the 30 min interval and the typical standard deviation involved was 0.2%.

5.3.3 Picosecond Transient Grating System

The principle of the transient grating technique for bulk measurements is as follows. A picosecond light pulse is split into two parts which are crossed in the sample at an angle θ. If the diameter of the pump pulses is sufficiently large and if the distance between interference fringes is small compared to the dimensions of the sample, a one-dimensional, spatially periodic interference pattern will be created in the bulk of the sample [115]. The fringe spacing is given by

$$\Lambda = \frac{\lambda}{2\sin(\theta/2)} \tag{5.6}$$

where λ is the optical wavelength. Optical absorption causes thermal expansion, which launches longitudinal acoustic waves of wavelength Λ into the sample, and also produces a periodic variation in the index of refraction through its temperature dependence, which subsequently decays via thermal diffusion. Both the acoustic response and the decaying thermal grating cause diffraction of a continuous-wave probe beam, which is monitored by an oscilloscope synced to the pump pulses.

As the acoustic waves propagate through the sample, the produce oscillations in the probe signal which can be used to study the behavior of particular phonon modes [116]. This acoustic signal decays rapidly through damping effects, while the thermal grating decays more slowly through thermal diffusion. The addition of nanoparticles modifies the acoustic response of the base fluid by increasing the rate

at which the longitudinal waves decay [117], as we will see in Section 5.4. In our samples, the acoustic response decayed within a few hundred nanoseconds, while the thermal response typically decayed over tens or hundreds of microseconds. Because of this difference in time scales, we are able to focus on the thermal decay without considering acoustic effects, regardless of the presence of nanoparticles.

The thermal response is governed by the 1-D heat equation. Because the pump pulse and acoustic response are much shorter than the thermal response, we can approximate the source term as a spatially periodic impulse function:

$$\frac{\partial T}{\partial t} = \alpha \frac{\partial^2 T}{\partial x^2} + \frac{Q}{\rho c_p} \delta(t) \cos\left(\frac{2\pi}{\Lambda} x\right) \tag{5.7}$$

Here T is the temperature, α is the thermal diffusivity, ρ is the density, c_p the specific heat capacity, and Q is the energy per pulse. The solution, conveniently found with a Laplace transform, is

$$T = \frac{Q}{\rho c_p} \exp(-t/\tau) \cos\left(\frac{2\pi}{\Lambda} x\right) \tag{5.8}$$

where the thermal decay time constant τ is

$$\tau = \frac{\Lambda^2}{4\pi^2 \alpha} \tag{5.9}$$

Our particular setup is shown in Fig. 5-11. The pump laser produces a train of 80 ps FWHM pulses of 1030 nm light. The probe laser is a continuous-wave (CW) diode at 830 nm. A custom made phase grating, designed to maximize diffraction into the ± 1 orders at 800 nm, is used to split both pump and probe beams. Because of the longer wavelength, 30% - 40% of the pump power is lost in the 0th order. A pair of achromatic lenses reduce the diffraction pattern by a factor of two in the bulk of the sample, where the pump beams induce the thermal grating in the liquid.

The grating spacings were calibrated to within 1% accuracy by measuring the acoustic frequency observed in ethylene glycol at room temperature and using the fact that the acoustic velocity near room temperature is given by $v = 1658[\text{m/sec}] -$

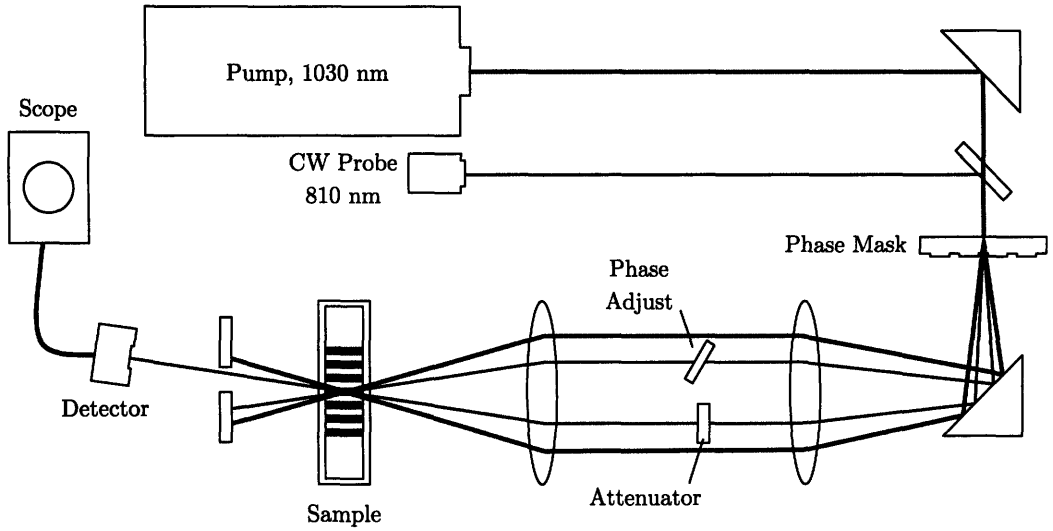

Figure 5-11: Transient grating setup. The pulsed pump beam and a continuous-wave (CW) probe beam are diffracted into two beams each by a custom phase mask. A pair of achromatic lenses reduce the diffraction pattern by a factor of two in the bulk of the sample. The probe beam interacts with the pump-induced grating in the material and diffracts into the detector.

2.1[sec K] $\times$ (T[K] $-$ 298K) [118]. A heterodyne technique is used to maximize the diffracted probe signal and eliminate instrument response and noise from the signal. One arm of the probe beam, the "reference", is attenuated by a factor of 10^{-3} and goes directly into the detector. The other "signal" arm is diffracted by the induced grating into the same path as the reference beam with a diffraction efficiency on the order of 10^{-6}. The amplitude of the resultant field is given by:

$$E^2 = E_r^2 + E_s^2 + 2E_rE_s\cos(\phi) \tag{5.10}$$

where E_r is the field of the reference arm, E_s the signal arm, and ϕ the phase difference between the two beams. The first term in Eq. 5.10 is continuous and therefore affects only the baseline reading on the oscilloscope. The magnitude of E_s is $\sim 10^{-3}$ smaller than E_r and so the homodyne term, E_s^2, is less than $\sim 10^{-6}$ of the total signal. The third term is the heterodyne signal which is directly proportional to the contrast in the index of refraction [73] and decays with a time constant given by Eq. 5.9. Any remaining influence due to the homodyne term as well as instrument response

is removed by making use of the phase angle in the heterodyne term: the signal arm of the probe passes through a glass slide which is rotated to maximize the signal by changing the phase between the two beams. Two measurements are taken: one at $\phi = 0$ and another at $\phi = \pi$. When the second measurement is subtracted from the first, the homodyne term as well as electronic response and other sources of systematic noise are removed while the true signal is doubled.

The liquid samples were held in a cuvette that was 200 μm thick. The grating spacing was typically 2–6 μm, satisfying the criteria for 1-D heat flow. The thin sample holder was chosen to minimize scattering in samples with higher concentrations of suspended particles; the scattering attenuated the signal and reference arms of the probe beam reaching the detector, reducing the overall signal-to-noise ratio. Using known samples, it was determined that if the photodetector were saturated, the measured decay constants were 3–4% faster than the correct value, resulting in spuriously high diffusivity measurements. Therefore, the probe intensity into the photodetector was adjusted to ensure that the detector was not saturated. Samples with lower particle concentrations required lower probe intensity since there was less scattering and more light reached the detector.

A typical result is shown in Fig 5-12, taken from pure PAO plus surfactant. The left figure shows the thermal decay while the right figure shows the rapid acoustic response, which dies away within 300 ns. The slower thermal decay is finished after roughly 60 μs. Figure 5-13 shows data from decane with 0.5% volume fraction of nanoparticles. The data are noisier due to increased scattering from the particles, but they are well fit by the exponential decay from Eq. (5.7).

While in theory a single curve is sufficient to extract the thermal diffusivity, uncertainty can be reduced by repeating the measurement at different grating spacings. This is accomplished by changing the phase mask, which changes the crossing angle of the pump beams in Eq. 5.6. If the measured decay time is plotted against the quantity $\Lambda^2/4\pi^2$, the result should be a straight line with slope α^{-1}. Measurements were made at 8–10 angles ranging from 8.9°–36.2°. A typical set of results, in the case from pure PAO, is shown in Fig. 5-14.

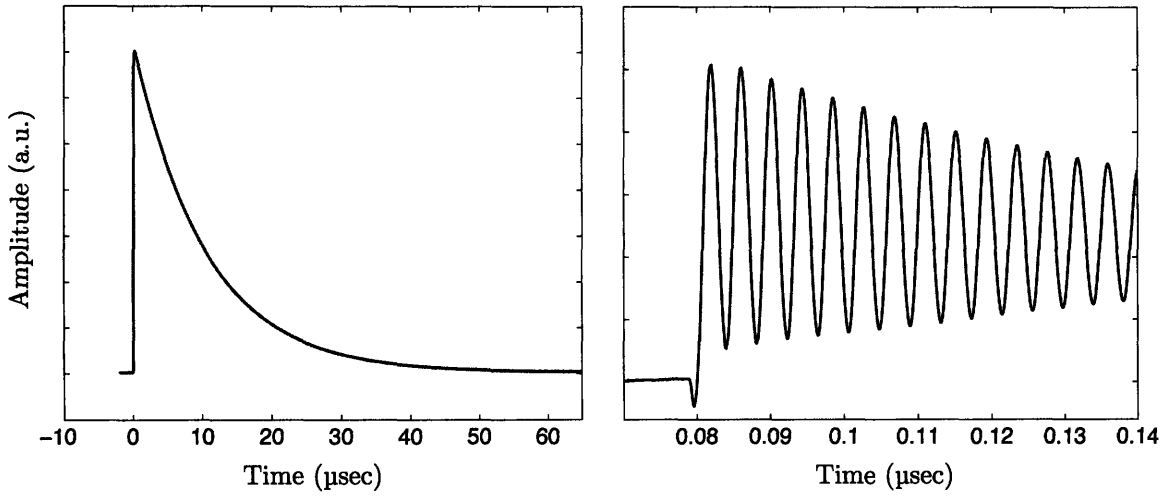

Figure 5-12: Typical result obtained during a TG measurement. The thermal decay is finished after roughly 60 μs (left) while the acoustic response dies away within 300 ns.

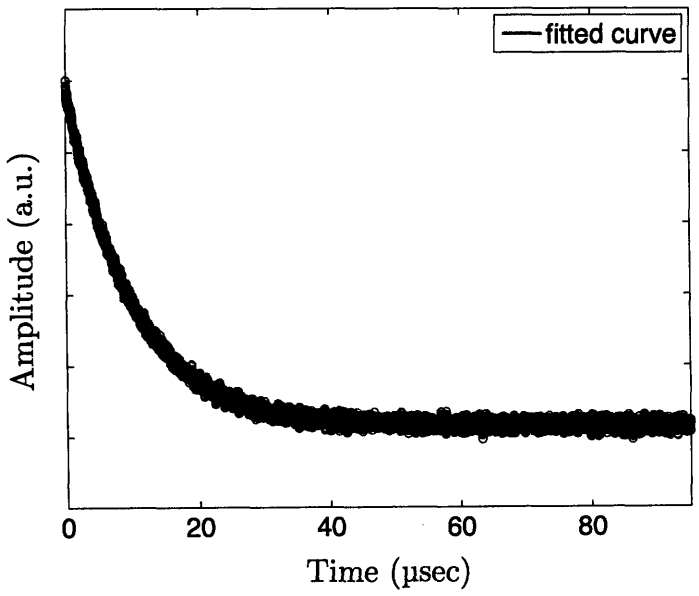

Figure 5-13: Data from decane with 0.5% volume fraction of nanoparticles and the best fit exponential decay.

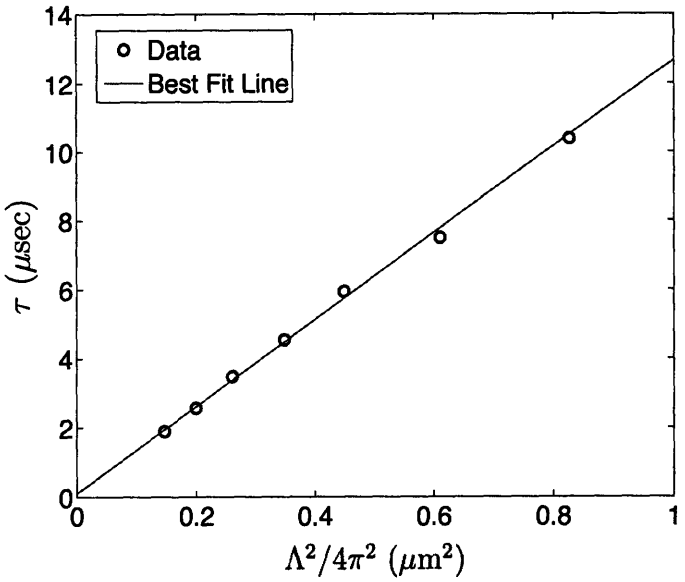

Figure 5-14: Thermal decay time measured at several grating spacings, plotted against the quantity $\Lambda^2/4\pi^2$, where Λ is the grating spacing. The slope of line is the inverse thermal diffusivity.

5.3.4 Results

The hotwire measurement yields the thermal conductivity directly, while the TG measurement gives the thermal diffusivity. To compute the thermal conductivity, the heat capacities and densities of the base fluids and solid particles are needed. The values used are listed in Table 5.1. The conductivity of the nanofluid, k_{nf}, is given by $\alpha(\rho c_p)_{\text{nf}}$ where α is the measured diffusivity and $(\rho c_p)_{\text{nf}}$ is the effective volumetric heat capacity, given by $(\rho c_p)_{\text{nf}} = \phi(\rho c_p)_{\text{particle}} + (1-\phi)(\rho c_p)_{\text{fluid}}$, where ϕ is the volume fraction of particles. As a validation of our systems, the measured values for the pure base fluids from both setups, without surfactant, are also provided in Table 5.1, along with the literature values.

The thermal conductivity of the Al_2O_3 in decane and PAO suspensions was measured in less than a day after dispersing the nanoparticles. All tests were carried out in an ambient temperature of approximately 20°C. Figure 5-15 shows the thermal conductivity enhancement of the Al_2O_3 in decane nanofluid for volume fractions ranging from 0.1% to 1.0%, normalized by the conductivity of the base fluid. The circles in Fig. 5-15 are obtained by means of the transient hot-wire technique, while the

triangles in are obtained by means of the TG technique. Figure 5-16 shows the same information for the PAO nanofluid. The results indicate a good agreement between the two sets of measurements across the range of concentrations tested.

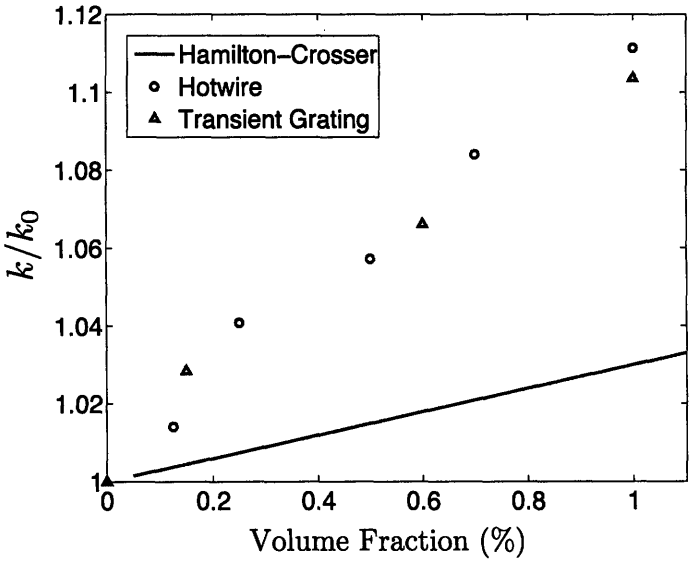

Figure 5-15: Thermal Conductivity measurements for decane, obtained with the hotwire and transient grating. Thermal conductivity over that of the base fluid + surfactant is plotted against the volume fraction of Al_2O_3 particles.

The thermal conductivity ratio predicted by the Hamilton-Crosser theory [107] is given by

$$\frac{k_{nf}}{k_f} = \frac{k_p + 2k_f - 2\phi(k_f - k_p)}{k_p + 2k_f + \phi(k_f - k_p)} \tag{5.11}$$

Here k_f, k_p and k_{nf} are the thermal conductivity of the base fluid, particle and nanofluid respectively and ϕ is the volume fraction of the nanoparticles. The above expression for effective thermal conductivity does not take into account the thermal interface resistance between the particle and the fluid and is applicable only for dilute solutions of spherical particles, a reasonable assumption based on SEM images such as Fig. 5-9. The solid line plotted in Fig. 5-15 and Fig. 5-16 is the thermal conductivity ratio prediction based on Eq.5.11. One can observe that the measured thermal conductivity ratio was higher than that predicted by the Hamilton-Crosser theory for all the volume fractions considered. In all cases the enhancement was linear with concentration. For the PAO nanofluid, the rate of enhancement vs. volume fraction

Table 5.1: Properties of the Base Fluids and Particles

Material	c_p (J/kg·K)	ρ (kg/m^3)	k (lit.) (W/m·K)	k (hotwire) (W/m·K)	k (TG) (W/m·K)
Decane	2210 [63]	727 [63]	0.132 [119]	0.132	0.135
PAO	2132 [120]	817 [121]	0.136 [120]	0.140	0.139
Al_2O_3	775 [63]	3990 [63]	35 [63]		

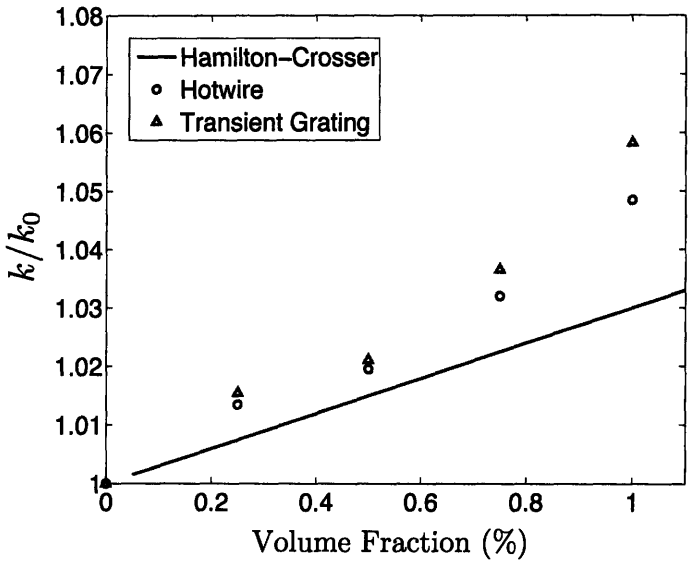

Figure 5-16: Thermal Conductivity measurements for PAO, obtained with the hotwire and transient grating. Thermal conductivity over that of the base fluid + surfactant is plotted against the volume fraction of Al_2O_3 particles.

was 1.6 times greater than the continuum model, while for decane the rate was 3.3 times greater.

The agreement between the two sets of data is good, though there is some discrepancy, especially at 1% volume concentration. We attribute this to statistical error in the TG measurement: at 1% the sample, even though only 200 μm thick, is fairly opaque and the transmitted probe beam is weak. Generally, absorption in the sample limits the TG technique to low concentrations. The generally good agreement indicates that the observed enhancement is both real and reproducible. This provides a firmer foundation for modeling and understanding the physics of transport in nanoparticle suspensions. In the next section, we use the acoustic portion of the TG signal to investigate the viscous properties of the nanofluids and the behavior of the nanoparticles in solution.

5.4 Viscosity and Clustering

We have described in detail the synthesis of suspensions of Al_2O_3 in decane and PAO, and we measured their thermal conductivities two independent techniques. The measured thermal conductivity enhancement in both cases agreed very well; the largest error was around 1% at a 1% volume loading, where low transmissivity through the sample limits the accuracy of the TG measurement. Both nanofluids showed a conductivity enhancement greater than predicted by the classical continuum models, with the PAO nanofluid exhibiting 1.6 times the rate of enhancement vs. volume fraction, and the decane nanofluid 3.3 times the enhancement.

Now we turn to the viscous properties of nanofluids. As we mentioned in the introduction to this chapter, in some nanofluid systems, the shear viscosity increases more rapidly than predicted by the Einstein model [108, 109] even at concentrations sufficiently small that the systems are truly dilute. One proposal for the enhancement in thermal conductivity is that the nanoparticles form clusters, resulting in larger effective particles [122], and it has been suggested that this may also be related to the enhanced shear viscosity as well [110].

Effective medium models for thermal conductivity [107], and the Einstein model for shear viscosity, depend only on the volume fraction of suspended particles; the particle diameter does not appear as an independent variable. However, theories for acoustic attenuation, and the related quantity of longitudinal viscosity, have a dependence on both volume fraction and particle size [123, 124]. Here we present shear and longitudinal viscosity data on the same two nanofluid systems: alumina nanoparticles in decane and PAO. The shear viscosity data exhibit an enhancement over the Einstein model, matching the findings of other authors [110–112], and the longitudinal viscosity data indicate that nanoparticles do not form clusters in these nanofluid systems.

5.4.1 Shear Viscosity

Shear viscosity measurements on our nanofluids were also conducted using a controlled-stress AR-G2 rheometer in the Hatsopoulos Microfluids Laboratory at MIT. The measurements were performed at approximately 22°C and the system accuracy was verified using a low-viscosity calibration oil (Silanol Teminated Polydimethylsiloxane from Gelest, Inc, PA). The viscosity changed less than 4% when tested over a shear rate ranging from 0.33 s^{-1} to 3270 s^{-1}. Results for the normalized viscosity are shown in Fig. 5-17.

In the dilute limit, the Einstein equation [108, 109] predicts that the relative enhancement in the shear viscosity of suspensions of spherical particles is given by $\eta(\phi)/\eta_0 = 1 + 2.5\phi$ where η_0 and $\eta(\phi)$ are the viscosity of the base fluid and the nanofluid respectively. Prasher et al. [110] compiled data for Al_2O_3 nanoparticles in water, ethylene glycol, and polyethylene glycol from their own measurements and those of Wang et al. [112] and Das et al. [111]. The data were well captured for volume fractions up to 8% by $\eta(\phi)/\eta_0 = 1 + 10\phi$; this result is shown in Fig. 5-17 for comparison with our own data.

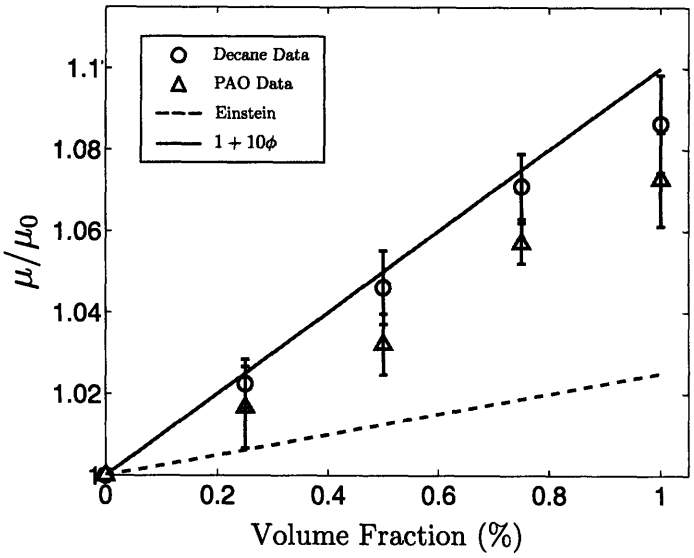

Figure 5-17: Shear viscosity for PAO and decane for volume fractions of Al_2O_3 from 0.25–1%. The results are similar to $\eta(\phi)/\eta_0 = 1 + 10\phi$ as observed by Prasher et al. [110].

5.4.2 Longitudinal Viscosity and Clustering

To study clustering of the nanoparticles in solution, we use the short-time acoustic response from the transient grating data discussed in Section 5-11. Optical absorption in the sample causes rapid thermal expansion, which launches a longitudinal acoustic wave into the sample, and also produces the slowly decaying periodic variation due to the temperature dependence of the index of refraction that we discussed in Section 5.3. Both the variation in strain due to the acoustic wave and the decaying thermal grating cause diffraction of a continuous-wave probe beam, which is monitored by an oscilloscope synced to the pump pulses. As the acoustic wave moves through the sample, it comes in and out of phase with the essentially static thermal grating, producing oscillations in the probe signal which can be used to deduce the elastic and viscous properties of the medium [49, 125].

A typical signal generated during the measurement is show in figure 5-18. This curve is fit with the functional form:

$$A\exp(-t/\tau)\cos(\omega t + \phi) + B\exp(-t/\tau_{th}) \tag{5.12}$$

The first term in Eq. (5.12) captures the decaying acoustic wave of frequency ω and time constant τ, while the second exponential term accounts for thermal decay with a time constant $\tau_{th} >> \tau$. In practice, we find that omitting the the second exponential term produces no change in the fit values for ω and τ.

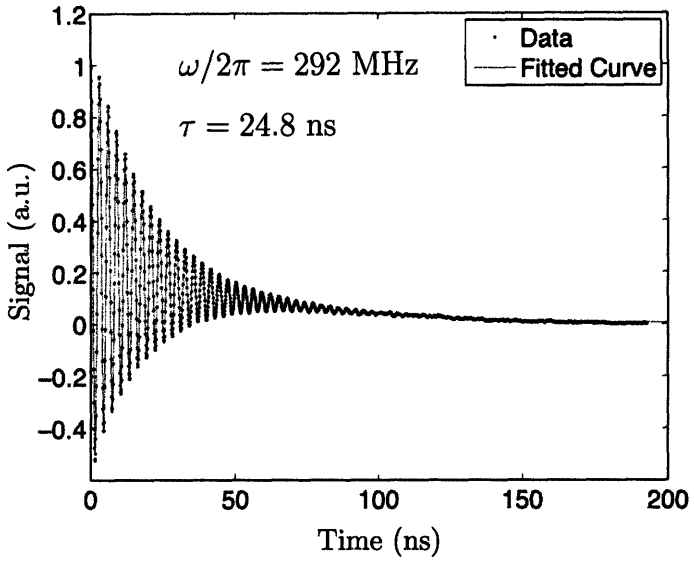

Figure 5-18: Typical signal data (in this case from PAO + surfactant) obtained from the excitation of one wave-vector and the best fit curve.

Multiple wave-vectors were be excited by varying the crossing angle in Eq. (5.6 from 8.9°–36.2°, creating acoustic waves with frequencies from 200–600 MHz. When the acoustic time scale is sufficiently fast that thermal effects can be neglected, and provided the fluid is Newtonian over the frequency range studied, the acoustic decay time τ is related to the viscous properties of the medium by [83, 125] :

$$\tau^{-1} = \frac{1}{2}k^2\nu_L \tag{5.13}$$

where k is the wave-vector, $\nu_L = (\frac{4}{3}\eta + \kappa)$ is referred to as the longitudinal viscosity, η is the shear viscosity and κ is the bulk viscosity. Figure 5-19 shows a typical plot of τ^{-1} vs. $1/2k^2$, in this case for decane with a 0.5% volume fraction of alumina.

When particles are present, the acoustic decay rate includes contributions from the base fluid and the particles: $\tau^{-1} = \frac{1}{2}k^2\nu_{L,0} + \tau_{part}^{-1}$. The first term on the right hand

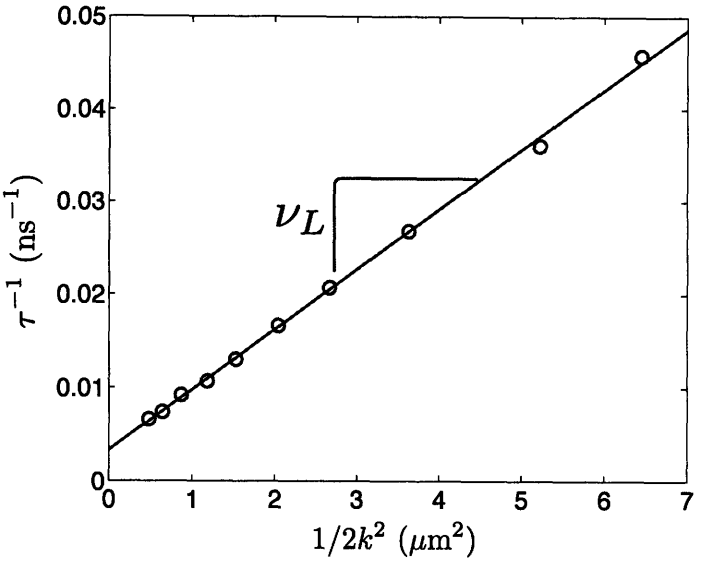

Figure 5-19: Damping rate τ for decane with 0.5% alumina at 10 wave-vectors plotted against $1/2k^2$. The slope of the line is the effective longitudinal viscosity.

side accounts for the longitudinal viscosity of the base fluid and is found by measuring the base fluid alone. The second term accounts for the additional attenuation due to the particles. In our case, the acoustic decay time is sufficiently fast that thermal decay can be neglected for time-scales on the order of 100 ns [125]. The particle size (~40 nm) is also much smaller than the acoustic wavelength so we use a continuum approach developed by Harker and Temple (H-T) [123]. In this model, the hydrodynamic wave equations are solved using momentum balance and continuity of the two interacting phases. The decay rate due to particles is given by $\tau_{part}^{-1} = c_0 \times \mathrm{Im}\{q\}$ where c_0 is the sound speed and q is the complex wave-vector given by

$$q^2 = \omega^2 \left[(1-\phi)\beta\right] \times \frac{\rho_f \left[\rho_s(1-\phi+\phi S) + \rho_f S(1-\phi)\right]}{\rho_s(1-\phi)^2 + \rho_f \left[S + \phi(1-\phi)\right]} \tag{5.14}$$

Here ϕ is the volume fraction, ω is the angular frequency of the wave, β is the compressibility of the fluid, ρ_s and ρ_f are the densities of the solid and fluid, respectively, and S is:

$$\frac{1}{2}\left(\frac{1+2\phi}{1-\phi} + \frac{9\delta}{4a}\right) + i\frac{9}{4}\left(\frac{\delta}{a} + \frac{\delta^2}{a^2}\right) \tag{5.15}$$

where a is the particle radius, $\delta = \sqrt{2\eta_0/\omega\rho_f}$ is the viscous penetration depth and η_0

Table 5.2: Measured Properties of the Base Fluids

Fluid	β $(\text{Pa}^{-1})\times 10^{-9}$	η_0 $(\text{Pa·s})\times 10^{-3}$	$\nu_{L,0}$ $(\text{Pa·s})\times 10^{-3}$
Decane + Surf.	0.41	0.85	4.10
PAO + Surf.	0.74	30.0	32.3

is the shear viscosity of the base fluid. The compressibility of the base fluid is found through $\beta^{-1} = c_0^2\rho$ [83], where the isentropic sound speed, c_0, is found by plotting the wave-vector against frequency and taking the slope of the resulting line. The measured compressibility, longitudinal and shear viscosities of the base-fluids plus surfactant are listed in Table 5.2.

The total decay rate was computed over the range of wave-vectors for our data at each concentration point. The particle diameter, $2a$, was taken as 40 nm determined from SEM images. For these frequencies, the solution damping rate exhibited a Newtonian $1/2k^2$ dependence and the slope was taken as the effective bulk viscosity of the suspension. The model results are for both nanofluids are shown in Fig. 5-20, along with the measured bulk viscosities.

Using the measured shear viscosity, the H-T model matches the decane longitudinal viscosity data but under-predicts attenuation for the PAO suspensions. As we discuss shortly, this discrepancy could be due to clustering or to a reduction in the shear viscosity of PAO at high frequencies. We suspect the latter case because of measurements on PAO without particles. For the base fluid, the bulk viscosity κ can be directly deduced from the measured longitudinal and shear viscosities: $\kappa = \nu_{L,0} - \frac{4}{3}\eta_0$. In our experiments, $\nu_{L,0}$ was measured at high frequency while η_0 was measured for shear rates from 4 s^{-1} to 700 s^{-1}. For pure decane, this yields $\kappa = 2.54 \times 10^{-3}$ Pa·s, in good agreement with a literature value [126]. However, for pure PAO, the same operation yields a negative value for bulk viscosity, indicating that the steady shear viscosity must be significantly higher than the shear viscosity at 200–600 MHz. Compared with decane, which is composed of a single hydrocarbon, PAO is a complex mixture of many long-chain hydrocarbons and thus can be expected to have more

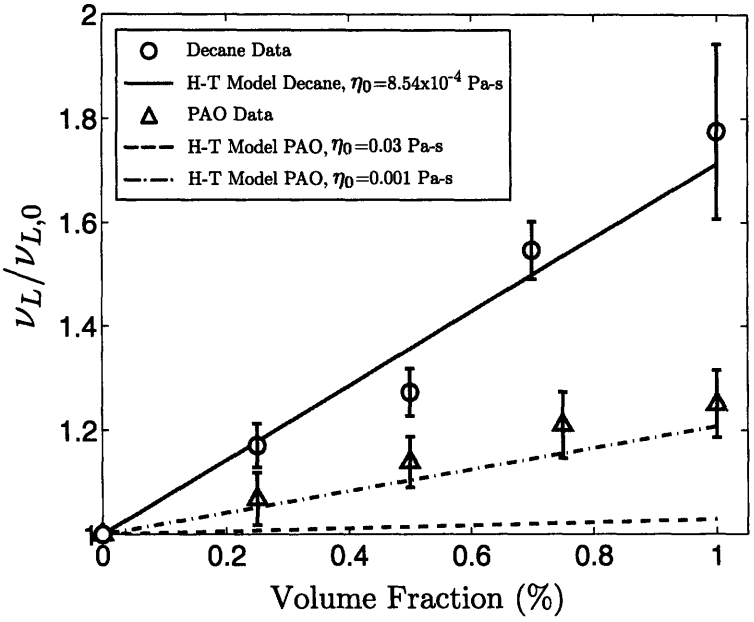

Figure 5-20: Effective bulk viscosity for volume fractions from 0.25%–1.0%. Using a particle diameter of 40 nm and the measured shear viscosity, the Harker-Temple model matches well for the decane system, but under-predicts for the PAO system when the value of shear viscosity measured at low shear rates, $\eta_0 = 0.03$ Pa·s is used. The theory matches better if a much lower value for the shear viscosity is assumed to be relevant over the frequency range of the experiment.

complex visco-elastic behavior. This idea is further supported by noting that if a lower value of shear viscosity is inserted into the H-T model, the result more closely matches the data. The predicted result for PAO using a shear viscosity η_0 of 0.001 Pa·s is shown in Fig. 5-20 for reference.

By varying the particle radius in Eq. (5.14), we can look at the longitudinal viscosity results in another way and deduce the size of the dispersed particles in suspension. Figure 5-21 shows the rate of increase of normalized longitudinal viscosity with volume % particles, now plotted as a function of particle diameter. For decane, the predicted increase is close to the measured increase using the SEM-observed diameter of ~40 nm. Even more interesting is the fact the function has a strong maximum close to this value, implying that the measured increase in longitudinal viscosity constrains the particle diameter to be in the neighborhood of 40 nm. As in Fig. 5-20, the fit of the model for the PAO nanofluid model is poor using the measured zero-shear rate viscosity. Again, if a much lower value of η_0 is used then the agreement improves; the result for η_0 of 0.001 Pa·s is shown in Fig. 5-21 for reference.

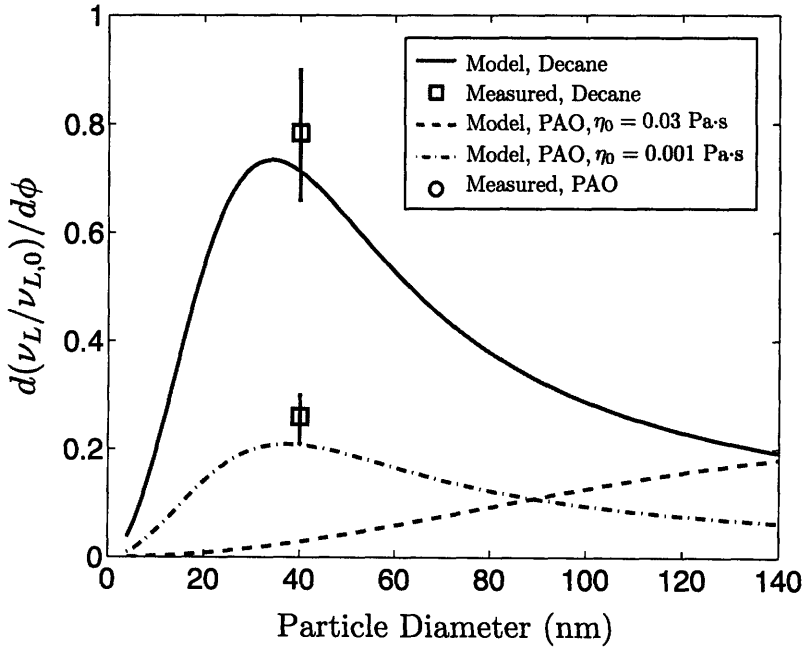

Figure 5-21: Rate of increase of normalized longitudinal viscosity with volume % particles, plotted as a function of particle diameter. The measured longitudinal viscosity enhancement for each fluid is indicated at 40 nm, the value observed via SEM.

For the decane-based nanofluid, Fig. 5-21 implies that the nanoparticles are not clustering. In the case of PAO, the conclusion is not as clear. Figure 5-21 shows that either a particle size on the order of 140 nm, or a greatly decreased shear viscosity of the base fluid at high frequency could reproduce the observed result. However, as we discussed above, the measured values of η_0 and $\nu_{L,0}$ would imply a bulk viscosity $\kappa < 0$ if the fluid were simply a Newtonian fluid with constant viscosity. This implies that there must be some reduction in shear viscosity over the measured DC value; we do not know exactly what the reduction is, so it is not possible to infer with certainty the effective particle size from the model.

5.4.3 Conclusion

To summarize, we have used an optical transient grating technique to investigate the thermal and viscous properties of nanofluids. We found that suspensions of alumina nanoparticles in decane and in PAO exhibit both enhanced thermal conductivity and shear viscosity over that predicted by classical continuum models. We have shown this enhancement to be real and reproducible. In Section 5.3, we compared thermal conductivity measurements from two dissimilar techniques and found good agreement. In this section, we presented shear viscosity data on two nanofluid systems that matched similar findings in the literature.

The measurements of longitudinal viscosity presented in this section for decane-based nanofluids yield self-consistent data for non-clustered particles dispersed in a Newtonian solvent of constant viscosity. For the PAO-based nanofluid the response is more complex and further study of the frequency-dependent viscous response in the oligomeric suspending oil is still required. Nonetheless, the results imply that clustering may not be responsible for the failure of the continuum models to describe nanofluid behavior, and alternative possibilities need to be investigated.

5.5 Summary

In this chapter, we presented experimental studies on nanofluids from two perspectives: the heat transfer between an individual nanoparticle and its surroundings, and the effective bulk thermal and viscous properties of the suspensions. Transmission pump-probe measurements on gold nanorods in suspension demonstrated the critical role played by surfactants in the thermal transport between a nanoparticle and the surrounding fluid, a factor often neglected in the study of nanofluids. Then, the use of an optical transient grating technique to explore the bulk thermal and viscous properties of nanofluids was discussed. Thermal conductivity measurements show that the observed thermal conductivity enhancement of nanofluids is repeatable and is not a function of the measurement technique, while acoustic attenuation measurements indicate that the nanoparticles do not form clusters in solution in two nanofluid systems which exhibit enhanced thermal conductivity and shear viscosity.

Finally, we would like to touch briefly on the possibility of applying the measurement technique discussed in Section 4.1 to the study of nanofluids. In some ways this would seem a natural direction to follow, since that method works on small liquid volumes where natural convection is not an issue, and because unlike the transient grating approach, it is a reflection measurement and therefore could be used to study high volume-fraction suspensions.

Some preliminary measurements on suspensions of 2% alumina in decane were done, and we observed a huge variation in the results between different locations on the glass slide, often as much as 30–40%. After taking more than 20 measurements, the average value did begin to converge to the value found via hotwire, although many more measurements would be needed to approach the precision necessary for confident characterization of a nanofluid. The scatter in the data is not surprising when one considers that the technique is only sensitive to the first 100–300 nm of fluid, and that the nanoparticles are almost certainly behaving differently at the Al-liquid interface than in the bulk. For example, microscopic scratches and other imperfections in the Al layer could trap the particles and change the measured thermal conductivity.

Further analysis, especially a careful consideration of the behavior at the interface, is needed before the technique can used for the study of nanofluids.

Chapter 6

Summary and Outlook

6.1 Summary

Nanoscale thermal transport is critical to current and emerging technologies ranging from microelectronics and solid-state energy conversion to novel cancer therapies. The pump-probe optical technique is a powerful tool for studying a wide variety of transport phenomena, and this thesis makes several contributions toward improving and extending its use for the characterization of thermal properties from the nanoscale upward.

Experimentally, the design and implementation of a pump-probe system is described in detail in Chapter 2. Our system incorporates many of the best aspects of systems built by others, notably Paddock and Eesley [13], Capinski and Maris [15], and Cahill [19, 50], while adding some new features such as a frequency-doubled pump beam, an expanded probe beam and a coaxial geometry, which reduce errors associated with optical noise, beam divergence, and spot shape and alignment, respectively.

From a theoretical point view, a mathematical description of the measurement process is given using the language of linear systems theory, encompassing the work on pulse accumulation by Capinski et. al. [15] and its extension to radial isotropic heat conduction through multilayer structures by Cahill [19], in a clear, consistent way. This approach enables us to explore the relationship between pulse accumulation and radial conduction effects and clearly show how pulse accumulation essentially allows

two length scales to be probed simultaneously. In addition, our analytical solution for radial heat transfer through multilayer structures includes anisotropic thermal properties without any additional computational expense over the isotropic solution given by Cahill [19].

Combined, Chapter 2 and Chapter 3 provide a cohesive story of how to use the pump-probe technique for thermal measurement, synthesizing the work of many previous authors. Many of the nitty-gritty details, which are so important to a successful measurement but are often left out of published material, have been included. Although these two chapters comprise less than half of this thesis, they represent more than 90% of the time invested, and packaging all of the experimental and theoretical details in one place is a valuable contribution in itself.

In Chapter 4, new applications of the technique are described. The first is a new approach for measuring the thermal conductivity of liquids which has unique advantages over existing methods, notably the ability to measure liquid films as thin as a few hundred nanometers, with no dependence on the optical properties of the liquid itself. The second major application is the measurement of both cross-plane and in-plane thermal properties through variation of the spot size and frequency of the pump-probe measurement. The technique is successfully demonstrated on highly ordered pyrolytic graphite, and its limitations and application to superlattice structures is discussed. The measurement of the in-plane thermal conductivity of thin films has traditionally been an experimental challenge, and this approach has the potential to simplify the problem in appropriate situations.

Finally, optical techniques for the study of nanofluids are discussed in Chapter 5. Transmission pump-probe measurements on gold nanorods in suspension are presented which demonstrate the critical role played by surfactants in the thermal transport between a nanoparticle and the surrounding fluid, a factor often neglected in the study of nanofluids. Then, the use of an optical transient grating technique to explore the bulk thermal and viscous properties of nanofluids is discussed. Thermal conductivity measurements show that the observed thermal conductivity enhancement of nanofluids is repeatable and is not a function of the measurement technique,

while acoustic attenuation measurements indicate that the nanoparticles do not form clusters in solution in two nanofluid systems which exhibit enhanced thermal conductivity and shear viscosity. Taken as a whole, Chapter 5 demonstrates the potential of optical techniques for the study of nanofluids and provides new experimental results from the nanoscale to the macroscale.

6.2 Outlook and Conclusion

While this thesis discusses several new applications of the pump-probe technique for thermal measurement and also some interesting new results, particularly on nanofluids, the work presented here barely scratches the surface of the possibilities in the field of nanoscale energy transport and conversion. For example, the first 100 ps after optical excitation are rich with interesting physics. We briefly mentioned some of these processes in Chapter 1, including electron-phonon non-equilibrium, acoustic attenuation of specific phonon modes, and ballistic electron and phonon transport, but for the most part we ignored these processes and focused on the diffusion regime.

Some steps are already being taken in our laboratory to look more closely at times before a diffusion picture is valid. By replacing the heat diffusion equation with the Boltzmann transport equation (BTE), it may be possible to observe ballistic phonon transport during the first 100 ps in crystalline materials such as silicon at room temperature [127], and the behavior would become more obvious at lower temperatures. Such measurements could lead to direct experimental observation of heat carrier relaxation times. Another possibility along similar lines is the optical excitation of thermoelectric materials such SiGe nanocomposites, which could lead to measurements of electron transport and grain-boundary scattering.

Similarly, the work on liquid measurement presented Section 4.1 could be extended in several directions. The fact that the liquid layer is only required to be a few hundred nanometers thick makes it possible to apply an enormous electric field across the liquid volume with only a modest applied voltage. By using the Al transducer as one electrode, thermal transport parallel to the electric field could be observed. The

behavior of nanoparticles and emulsions under these conditions would lead to better understanding of their dynamics in suspension. Another potential area of sudy comes from the fact that thermal transport across the Al-liquid interface depends on the interface conditions. This fact could be exploited to study the performance of thermal interface materials which are widely used to make thermal contact between microelectronic structures and heat sinks. The Al layer could be coated with a few nanometers of a second material such as Si or SiO_2 to mimic the surface of a microelectronic device, and then a thermal interface material could be applied and the sample pressed against a third material such as a polished copper plate. This arrangement would be a powerful method for evaluating thermal interface materials.

These are just a few out of many possibilities. Ultrafast phenomena and nanoscale transport will continue to become increasingly relevant as technology pushes the boundaries of real-world applications ever smaller and faster, and the pump-probe technique will be an essential tool for their characterization.

Appendix A

Details on Signal Analysis

A.1 The Effect of Higher Harmonics

A square wave $y(t)$, in this case with an arbitrary phase of zero, can be represented as the sum of its harmonic components:

$$y(t) = \sum_{n=1,3,5,\ldots}^{\infty} (-1)^{\frac{n-1}{2}} \frac{4}{n\pi} \cos(n\omega_0 t) \tag{A.1}$$

As an example, the sum of the first three components is shown in Fig. A-1.

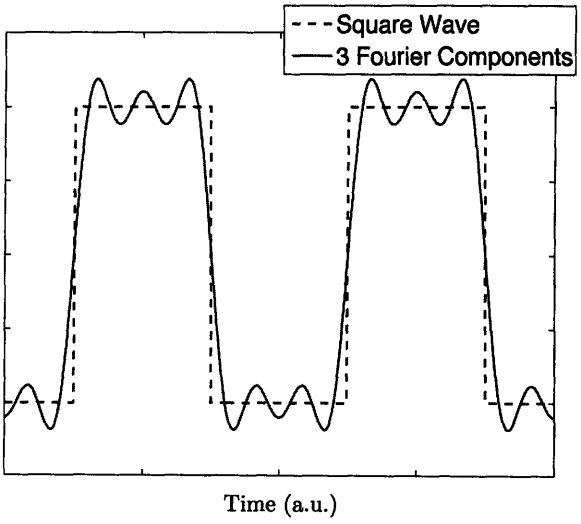

Figure A-1: A square wave and the first three harmonic components

Figure A-2 (a.) shows the square wave in frequency space. The square wave is sampled by the laser pulse train with strength Q and frequency w_s. Applying the sampling theorem (see Section A.3) to the square wave signal gives the result shown in Fig. A-2 (b.), producing a series of shifted copies of the original spectrum, separated by the sampling frequency ω_s.

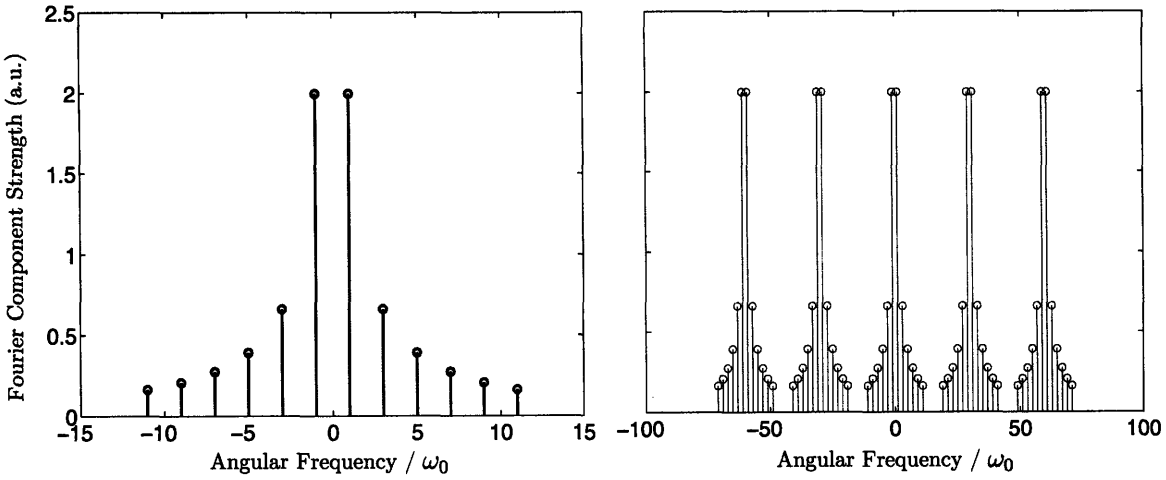

Figure A-2: (a.) Frequency components of a square wave with frequency ω_0. (b.) Frequency components of a pulsed square wave with pulsing frequency ω_s. The result is a series of copies of the original spectrum, separated by ω_s.

We can repeat the frequency-domain analysis of Section 3.1.3 using the square wave signal instead of a pure sinusoid. The pump beam input is given by

$$Q(\omega) = \frac{2\pi Q}{T} \sum_{n=-\infty}^{\infty} \sum_{k=-\infty}^{\infty} \frac{1}{n} \delta(\omega - n\omega_0 - k\omega_s) \tag{A.2}$$

for odd values of n. If we carry this through the analysis, we get an expression similar to Eq. (3.27):

$$Z(\omega_0) = \frac{\beta Q Q_{\text{probe}}}{T^2} \sum_{l=-\infty}^{\infty} \sum_{n=-\infty}^{\infty} \sum_{k=-\infty}^{\infty} \frac{1}{n} H(n\omega_0 + k\omega_s) \delta\left((1-n)\omega_0 - (k+l)\omega_s\right) e^{-jl\omega_s\tau} \tag{A.3}$$

The only non-zero terms meet the condition:

$$(k+l) = (1-n)\frac{\omega_0}{\omega_s} \tag{A.4}$$

Since l, k and n are all integers, this condition can only be satisfied if ω_s is very close to a multiple of ω_0 (within the lock-in pass band), and even then, if $\omega_s \gg \omega_0$, these higher harmonics are are reduced by a factor of $1/n$ and so can be be neglected. Thus the response to a square wave input at ω_0 is approximately equal to the response to a pure sinusoid at that frequency, and Eq. (3.27) is valid.

A.2 Proof of Equation 3.14

We wish to show that

$$\sum_{n=-\infty}^{\infty} e^{i\omega_0(nT+T_0+\tau)} e^{-i\omega(nT+T_0+\tau)} = e^{i(\omega_0-\omega)(T_0+\tau)} \frac{2\pi}{T} \sum_{n=-\infty}^{\infty} \delta(\omega_0 - \omega + \frac{2\pi n}{T}) \tag{A.5}$$

which requires that

$$\sum_{n=-\infty}^{\infty} e^{i(\omega_0-\omega)nT} = \frac{2\pi}{T} \sum_{n=-\infty}^{\infty} \delta(\omega_0 - \omega + \frac{2\pi n}{T}) \tag{A.6}$$

To prove this, we make use of two Fourier transform pairs [128]:

$$\mathcal{F}\left\{ \sum_{k=-\infty}^{\infty} e^{ik\alpha t} \right\} = 2\pi \sum_{k=-\infty}^{\infty} \delta(\omega - k\alpha) \tag{A.7}$$

$$\mathcal{F}\left\{ \sum_{k=-\infty}^{\infty} \delta(t - k\beta) \right\} = \frac{2\pi}{\beta} \sum_{k=-\infty}^{\infty} \delta(\omega - k\frac{2\pi}{\beta}) \tag{A.8}$$

where α and β are constants. Now we make the substitution $\alpha = 2\pi/\beta$ to see that

$$\sum_{k=-\infty}^{\infty} e^{ik\alpha t} = \frac{2\pi}{\alpha} \sum_{k=-\infty}^{\infty} \delta(t - \frac{2\pi k}{\alpha}) \tag{A.9}$$

We substitute the following variables:

$$\begin{aligned} k &\rightarrow n \\ t &\rightarrow \omega_0 - \omega \\ \alpha &\rightarrow T \end{aligned}$$

This gives

$$\sum_{n=-\infty}^{\infty} e^{i(\omega_0-\omega)nT} = \frac{2\pi}{T} \sum_{n=-\infty}^{\infty} \delta(\omega_0 - \omega + \frac{2\pi n}{T})$$

which is exactly Eq. (A.6).

A.3 The Sampling Theorem

The sampling theorem is a useful tool for understanding the frequency spectrum of a signal that is "sampled" at discrete times with a very short pulse. The theory is well-covered in reference [57]; we repeat it here for convenience. Given an original signal, $x(t)$, and a sampling signal $p(t)$, we can write the sampled signal as

$$x_p(t) = x(t)p(t) \tag{A.10}$$

where

$$p(t) = \sum_{n=-\infty}^{\infty} \delta(t - nT - T_0)$$

Here $p(t)$ is a series of unit impulses, T, is the sampling period and T_0 is an arbitrary delay time.

Now we take the Fourier transform of Eq. (A.10). Since multiplication in the time domain is equivalent to convolution in the frequency domain,

$$X_p(\omega) = \mathcal{F}\{x_p\} = \frac{1}{2\pi} \int_{-\infty}^{\infty} X(\theta)P(\omega - \theta)\, d\theta \tag{A.11}$$

where

$$\begin{aligned} X(\omega) &= \mathcal{F}\{x\} \\ P(\omega) &= \left[\frac{2\pi}{T}\sum_{k=-\infty}^{\infty}\delta(\omega - k\frac{2\pi}{T})\right]e^{-i\omega T_0} \end{aligned}$$

Therefore,

$$\begin{aligned} X_p(\omega) &= \frac{1}{T}\int_{-\infty}^{\infty} X(\theta)e^{-i(\omega-\theta)T_0}\sum_{k=-\infty}^{\infty}\delta(\omega-\theta-k\frac{2\pi}{T})\,d\theta \\ &= \frac{1}{T}\sum_{k=-\infty}^{\infty} X(\omega - k\frac{2\pi}{T})e^{-ik2\pi T_0/T} \end{aligned} \tag{A.12}$$

A.4 Equivalence of the Impulse and Frequency Response Solutions

Although we derived the impulse-response representation, Eq. (3.17), and the frequency-response representation, Eq. (3.27), independently, we show here that one can be transformed directly into the other.

Begin with the impulse-response expression of the response, Eq. (3.17):

$$Z(\omega_0) = \frac{\beta Q Q_{\text{probe}}}{T}\sum_{q=0}^{\infty} e^{-i\omega_0(qT+\tau)}h(qT+\tau) \tag{A.13}$$

Since $\int_{-\infty}^{\infty}\delta(x-x_0)f(x)\,dx = f(x_0)$, we can write this as

$$Z(\omega_0) = \frac{\beta Q Q_{\text{probe}}}{T}\int_{-\infty}^{\infty} h(t)\sum_{q=-\infty}^{\infty}\delta(t-qT-\tau)e^{-i\omega_0 t}\,dt \tag{A.14}$$

The definition of the Fourier transform is

$$X(\omega_0) = \int_{-\infty}^{\infty} x(t)e^{-i\omega_0 t}dt$$

so Eq. (A.14) becomes

$$\begin{aligned}
Z(\omega_0) &= \frac{\beta Q Q_{\text{probe}}}{T}\mathcal{F}\left\{h(t)\sum_{q=-\infty}^{\infty}\delta(t-qT-\tau)\right\} \\
&= \frac{\beta Q Q_{\text{probe}}}{T}H(\omega_0) * \mathcal{F}\left\{\sum_{q=-\infty}^{\infty}\delta(t-qT-\tau)\right\} \\
&= \frac{2\pi\beta Q Q_{\text{probe}}}{T^2}H(\omega_0) * \left[e^{-i\omega_0\tau}\sum_{k=-\infty}^{\infty}\delta(\omega_0-k\omega_s)\right] \\
&= \frac{\beta Q Q_{\text{probe}}}{T^2}\left[\int_{-\infty}^{\infty}H(\omega_0-\theta)e^{-i\theta\tau}\sum_{k=-\infty}^{\infty}\delta(\theta-k\omega_s)\,d\theta\right] \\
&= \frac{\beta Q Q_{\text{probe}}}{T^2}\sum_{k=-\infty}^{\infty}H(\omega_0-k\omega_s)e^{-ik\omega_s\tau} \\
&= \frac{\beta Q Q_{\text{probe}}}{T^2}\sum_{k=-\infty}^{\infty}H(\omega_0+k\omega_s)e^{ik\omega_s\tau}
\end{aligned}$$

This result is the same as Eq. (3.27).

A.5 Interpretation of the Real and Imaginary Parts

At the end of Section 3.1.3, we mentioned that the in-phase and out-of-phase components of the lock-in signal, X and Y, are given by

$$X = \text{Re}\{Z(\omega_0)\} \tag{A.15}$$

$$Y = \text{Im}\{Z(\omega_0)\} \tag{A.16}$$

Here we present the proof.

For any complex number Z,

$$\begin{aligned}
\text{Re}\{Z\} &= \frac{1}{2}[Z+Z^*] \\
\text{Im}\{Z\} &= \frac{1}{2i}[Z-Z^*]
\end{aligned} \tag{A.17}$$

Also, for any real signal $x(t)$, the Fourier transform has conjugate symmetry [57]:

$$X(-i\omega) = X^*(i\omega) \quad [x(t) \text{ real}] \tag{A.18}$$

Finally, it is generally true for two complex numbers Z_1 and Z_2

$$(Z_1 Z_2)^* = Z_1^* Z_2^* \tag{A.19}$$

In our case, $h(t)$ is the thermal response of a physical system and is therefore real, so (A.18) holds for $H(\omega)$. So, using (A.18) and (A.19) along with the fact that k runs from $-\infty$ to $+\infty$, we can write

$$\begin{aligned} Z(\omega_0) &= \frac{\beta Q Q_{\text{probe}}}{T^2} \sum_{k=-\infty}^{\infty} H(\omega_0 + k\omega_s) e^{ik\omega_s \tau} \\ Z^*(\omega_0) &= \frac{\beta Q Q_{\text{probe}}}{T^2} \sum_{k=-\infty}^{\infty} H(-\omega_0 + k\omega_s) e^{ik\omega_s \tau} \end{aligned}$$

Then, using equations (A.17),

$$\begin{aligned} \text{Re}\{Z(\omega_0)\} &= \frac{1}{2} \frac{\beta Q Q_{\text{probe}}}{T^2} \left[\sum_{k=-\infty}^{\infty} H(\omega_0 + k\omega_s) e^{ik\omega_s \tau} + \sum_{k=-\infty}^{\infty} H(-\omega_0 + k\omega_s) e^{ik\omega_s \tau} \right] \\ \text{Im}\{Z(\omega_0)\} &= \frac{-i}{2} \frac{\beta Q Q_{\text{probe}}}{T^2} \left[\sum_{k=-\infty}^{\infty} H(\omega_0 + k\omega_s) e^{ik\omega_s \tau} - \sum_{k=-\infty}^{\infty} H(-\omega_0 + k\omega_s) e^{ik\omega_s \tau} \right] \end{aligned}$$

The real part will correspond to the "in phase" signal and the imaginary part the "out of phase" signal. To show this, recall that the system response to a complex input is given by

$$z(t) = Z(\omega_0) e^{i\omega_0 t} \tag{A.20}$$

Expanding,

$$\begin{aligned} z(t) &= \Big[\mathrm{Re}\{Z(\omega_0)\} + i\mathrm{Im}\{Z(i\omega_0)\}\Big] e^{i\omega_0 t} \\ &= \Big[\mathrm{Re}\{Z(\omega_0)\}\cos(\omega_0 t) - \mathrm{Im}\{Z(\omega_0)\}\sin(\omega_0 t)\Big] \\ &\quad + \; i\Big[\mathrm{Re}\{Z(\omega_0)\}\sin(\omega_0 t) + \mathrm{Im}\{Z(\omega_0)\}\cos(\omega_0 t)\Big] \end{aligned}$$

The real part of this expression is the physical signal that is measured, and is given by

$$\mathrm{Re}\{z(t)\} = \mathrm{Re}\{Z(\omega_0)\}\cos(\omega_0 t) - \mathrm{Im}\{Z(\omega_0)\}\sin(\omega_0 t) \qquad \text{(A.21)}$$

It is comprised of a cosine ("in phase") wave with an amplitude given by $\mathrm{Re}\{Z(\omega_0)\}$, and a sine ("out of phase") wave with an amplitude given by $\mathrm{Im}\{Z(\omega_0)\}$, which correspond to the X and Y outputs of the lock-in amplifier, respectively. Thus, when referring to the lock-in signal, the terms "in phase" and "real part", and "out-of-phase" and "imaginary part", may be used interchangeably.

Bibliography

[1] Gang Chen. *Nanoscale Energy Transport and Conversion.* Oxford University Press, New York, 2005.

[2] David G. Cahill, Wayne K. Ford, Kenneth E. Goodson, Gerald D. Mahan, Arun Majumdar, Humphrey J. Maris, Roberto Merlin, and Simon R. Phillpot. Nanoscale thermal transport. *Journal of Applied Physics*, 93(2):793–818, 2003.

[3] Kenneth E. Goodson and Y. Sungtaek Ju. Heat conduction in novel electronic films. *Annual Review of Materials Science*, 29(1):261–293, 1999.

[4] Gang Chen. Heat transfer in micro- and nanoscale photonic devices. *Annual Review of Heat Transfer*, 7:69, 1996.

[5] David G. Cahill, Kenneth Goodson, and Arunava Majumdar. Thermometry and thermal transport in micro/nanoscale solid-state devices and structures. *Journal of Heat Transfer*, 124(2):223–241, 2002.

[6] H. J. Goldsmid. *Thermoelectric Refrigeration.* Plenum Press, New York, 1964.

[7] G. Chen. Thermal conductivity and ballistic-phonon transport in the cross-plane direction of superlattices. *Phys. Rev. B*, 57(23):14958–14973, Jun 1998.

[8] T. C. Harman, P. J. Taylor, M. P. Walsh, and B. E. LaForge. Quantum dot superlattice thermoelectric materials and devices. *Science*, 297(5590):2229–2232, 2002.

[9] Ronggui Yang and Gang Chen. Thermal conductivity modeling of periodic two-dimensional nanocomposites. *Phys. Rev. B*, 69(19):195316, May 2004.

[10] S. D. Brorson, A. Kazeroonian, J. S. Moodera, D. W. Face, T. K. Cheng, E. P. Ippen, M. S. Dresselhaus, and G. Dresselhaus. Femtosecond room-temperature measurement of the electron-phonon coupling constant γ in metallic superconductors. *Phys. Rev. Lett.*, 64(18):2172–2175, Apr 1990.

[11] Jeffrey A Eastman, S. R. Phillpot, S. U. S. Choi, and P. Keblinski. Thermal transport in nanofluids. *Annual Review of Materials Research*, 34(1):219–246, 2004.

[12] C. Dames and G. Chen. Theoretical phonon thermal conductivity of si/ge superlattice nanowires. *Journal of Applied Physics*, 95(2):682–693, 2004.

[13] Carolyn A. Paddock and Gary L. Eesley. Transient thermoreflectance from thin metal films. *Journal of Applied Physics*, 60(1):285–290, 1986.

[14] Bruce M. Clemens, Gary L. Eesley, and Carolyn A. Paddock. Time-resolved thermal transport in compositionally modulated metal films. *Phys. Rev. B*, 37(3):1085–1096, Jan 1988.

[15] William S. Capinski and Humphrey J. Maris. Improved apparatus for picosecond pump-and-probe optical measurements. *Review of Scientific Instruments*, 67(8):2720–2726, 1996.

[16] R. J. Stoner and H. J. Maris. Kapitza conductance and heat flow between solids at temperatures from 50 to 300 k. *Phys. Rev. B*, 48(22):16373–16387, Dec 1993.

[17] W. S. Capinski, H. J. Maris, T. Ruf, M. Cardona, K. Ploog, and D. S. Katzer. Thermal-conductivity measurements of gaas/alas superlattices using a picosecond optical pump-and-probe technique. *Phys. Rev. B*, 59(12):8105–8113, Mar 1999.

[18] Pamela M. Norris, Andrew P. Caffrey, Robert J. Stevens, J. Michael Klopf, Jr. James T. McLeskey, and Andrew N. Smith. Femtosecond pump–probe nondestructive examination of materials (invited). volume 74, pages 400–406. AIP, 2003.

[19] David G. Cahill. Analysis of heat flow in layered structures for time-domain thermoreflectance. *Review of Scientific Instruments*, 75(12):5119–5122, 2004.

[20] Ruxandra M. Costescu, Marcel A. Wall, and David G. Cahill. Thermal conductance of epitaxial interfaces. *Phys. Rev. B*, 67(5):054302, Feb 2003.

[21] H.-K. Lyeo and D. G. Cahill, D. G. Thermal conductance of interfaces between highly dissimilar materials. *Physical Review B (Condensed Matter and Materials Physics)*, 73(14):144301–+, April 2006.

[22] Bryan C. Gundrum, David G. Cahill, and Robert S. Averback. Thermal conductance of metal-metal interfaces. *Physical Review B (Condensed Matter and Materials Physics)*, 72(24):245426, 2005.

[23] David G. Cahill and Fumiya Watanabe. Thermal conductivity of isotopically pure and ge-doped si epitaxial layers from 300 to 550 k. *Physical Review B (Condensed Matter and Materials Physics)*, 70(23):235322, 2004.

[24] T. Q. Qiu and C. L. Tien. Short-pulse laser heating on metals. *International Journal of Heat and Mass Transfer*, 35(3):719–726, 1992.

[25] Guray Tas and Humphrey J. Maris. Electron diffusion in metals studied by picosecond ultrasonics. *Phys. Rev. B*, 49(21):15046–15054, Jun 1994.

[26] T. C. Zhu, H. J. Maris, and J. Tauc. Attenuation of longitudinal-acoustic phonons in amorphous sio_2 at frequencies up to 440 ghz. *Phys. Rev. B*, 44(9):4281–4289, Sep 1991.

[27] H. N. Lin, R. J. Stoner, H. J. Maris, and J. Tauc. Phonon attenuation and velocity measurements in transparent materials by picosecond acoustic interferometry. *Journal of Applied Physics*, 69(7):3816–3822, 1991.

[28] C. Thomsen, H. T. Grahn, H. J. Maris, and J. Tauc. Picosecond interferometric technique for study of phonons in the brillouin frequency range. *Optics Communications*, 60(1-2):55–58, 1986.

[29] Jean Baptiste Joseph Fourier. *The Analytical Theory of Heat.* The University Press, Cambridge, UK, 1878.

[30] J. Hohlfeld, S. S. Wellershoff, J. Gdde, U. Conrad, V. Jhnke, and E. Matthias. Electron and lattice dynamics following optical excitation of metals. *Chemical Physics*, 251(1-3):237–258, 2000.

[31] R. W. Schoenlein, W. Z. Lin, J. G. Fujimoto, and G. L. Eesley. Femtosecond studies of nonequilibrium electronic processes in metals. *Phys. Rev. Lett.*, 58(16):1680–1683, Apr 1987.

[32] S. D. Brorson, J. G. Fujimoto, and E. P. Ippen. Femtosecond electronic heat-transport dynamics in thin gold films. *Phys. Rev. Lett.*, 59(17):1962–1965, Oct 1987.

[33] N.W. Ashcroft and D. Mermin. *Solid State Physics.* Holt Rhinehart, New York, 1976.

[34] S.I. Anisimov, B.L. Kapeliovich, and T.L. Perel'man. *Sov. Phys. JETP*, 39:375, 1974.

[35] John L. Hostetler, Andrew N. Smith, Daniel M. Czajkowsky, and Pamela M. Norris. Measurement of the electron-phonon coupling factor dependence on film thickness and grain size in au, cr, and al. *Applied Optics*, 38(16):3614–3620, 1999.

[36] J. G. Fujimoto, J. M. Liu, E. P. Ippen, and N. Bloembergen. Femtosecond laser interaction with metallic tungsten and nonequilibrium electron and lattice temperatures. *Phys. Rev. Lett.*, 53(19):1837–1840, Nov 1984.

[37] H. E. Elsayed-Ali, T. B. Norris, M. A. Pessot, and G. A. Mourou. Time-resolved observation of electron-phonon relaxation in copper. *Phys. Rev. Lett.*, 58(12):1212–1215, Mar 1987.

[38] R. Rosei and D. W. Lynch. Thermomodulation spectra of al, au, and cu. *Phys. Rev. B*, 5(10):3883–3894, May 1972.

[39] M.G. Burzo, P.L. Komarov, and P.E. Raad. Minimizing the uncertainties associated with the measurement of thermal properties by the transient thermoreflectance method. *Components and Packaging Technologies, IEEE Transactions on [see also Components, Packaging and Manufacturing Technology, Part A: Packaging Technologies, IEEE Transactions on]*, 28(1):39–44, March 2005.

[40] E. T. Swartz and R. O. Pohl. Thermal boundary resistance. *Rev. Mod. Phys.*, 61(3):605–668, Jul 1989.

[41] E. T. Swartz and R. O. Pohl. Thermal resistance at interfaces. *Applied Physics Letters*, 51(26):2200–2202, 1987.

[42] W.A. Little. The transport of heat between dissimilar solids at low temperatures. *Canadian Journal of Physics*, 37:334–349, 1959.

[43] Gang Chen. *Nanoscale Energy Transport and Conversion.* Oxford University Press, New York, pp. 180–185, 2005.

[44] Zhenbin Ge, David G. Cahill, and Paul V. Braun. Thermal conductance of hydrophilic and hydrophobic interfaces. *Physical Review Letters*, 96(18):186101, 2006.

[45] Z. Ge, D.G. Cahill, and P.V. Braun. Aupd metal nanoparticles as probes of nanoscale thermal transport in aqueous solution. *Journal of Physical Chemistry B*, 108(49):18870–18875, 2004.

[46] A. Henry and G. Chen. Spectral phonon transport properties of silicon based on molecular dynamics simulations and lattice dynamics. *Journal of Computational and Theoretical Nanoscience*, 5(12):141–152, 2008.

[47] David Song and Gang Chen. Thermal conductivity of periodic microporous silicon films. *Applied Physics Letters*, 84(5):687–689, 2004.

[48] S. Das, S. Choi, and H. Patel. Heat transfer in nanofluids–a review. *Heat Transfer Engineering*, 27(10):3–19, 2006.

[49] John A. Rogers, Alex A. Maznev, Matthew J. Banet, and Keith A. Nelson. Optical generation and characterization of acoustic waves in thin films: Fundamentals and applications. *Annual Review of Materials Science*, 30(1):117–157, 2000.

[50] K. E. O'Hara, Xiaoyuan Hu, and David G. Cahill. Characterization of nanostructured metal films by picosecond acoustics and interferometry. *Journal of Applied Physics*, 90(9):4852–4858, 2001.

[51] Ryuji Morita, Masakatsu Hirasawa, Naoki Karasawa, Satoru Kusaka, Naoya Nakagawa, Keisaku Yamane, Liming Li, Akira Suguro, and Mikio Yamashita. Sub-5 fs optical pulse characterization. *Measurement Science and Technology*, 13(11):1710–1720, 2002.

[52] Eugene Hecht. *Optics.* Addison Wesley Publishing Company, New York, 1997.

[53] Stanford Research Systems, Sunnyvale, California. *User's Manual: Model SR844 RF Lock-In Amplifier*, revision 2.6 edition, October 2003.

[54] Masood Ghotbi and M. Ebrahim-Zadeh. Optical second harmonic generation properties of BiB_3O_6. *Opt. Express*, 12(24):6002–6019, 2004.

[55] E. Gramsch. Noise characteristics of avalanche photodiode arrays of the bevel-edge type. *Electron Devices, IEEE Transactions on*, 45(7):1587–1594, Jul 1998.

[56] Per Bak, Chao Tang, and Kurt Wiesenfeld. Self-organized criticality: An explanation of the 1/f noise. *Phys. Rev. Lett.*, 59(4):381–384, Jul 1987.

[57] Alan V. Oppenheim and Alan S. Willsky with S. Hamid. *Signals and Systems.* Prentice Hall, 2nd edition, 1996.

[58] H. S. Carslaw and J. C. Jaeger. *Conduction of Heat in Solids.* Oxford University Press, New York, 1959, pp. 109–112.

[59] A. Feldman. Algorithm for solutions of the thermal diffusion equation in a stratified medium with a modulated heating source. *High Temperatures - High Pressures*, 31(3):293–298, 1999.

[60] Jung Hun Kim, Albert Feldman, and Donald Novotny. Application of the three omega thermal conductivity measurement method to a film on a substrate of finite thickness. *Journal of Applied Physics*, 86(7):3959–3963, 1999.

[61] H. S. Carslaw and J. C. Jaeger. *Conduction of Heat in Solids.* Oxford University Press, New York, 1959,.

[62] David G. Cahill, S.-M. Lee, and Torbjorn I. Selinder. Thermal conductivity of κ-Al_2O_3 and α -Al_2O_3 wear-resistant coatings. *Journal of Applied Physics*, 83(11):5783–5786, 1998.

[63] David R. Lide, editor. *CRC Handbook of Chemistry and Physics, CRC Handbook of Chemistry and Physics, Internet Version 2007.* Taylor and Francis, Boca Raton, FL, 87 edition, 2007.

[64] C. Thomsen, H. T. Grahn, H. J. Maris, and J. Tauc. Surface generation and detection of phonons by picosecond light pulses. *Phys. Rev. B*, 34(6):4129–4138, Sep 1986.

[65] O. B. Wright. Thickness and sound velocity measurement in thin transparent films with laser picosecond acoustics. *Journal of Applied Physics*, 71(4):1617–1629, 1992.

[66] Tsuneyuki Yamane, Naoto Nagai, Shin ichiro Katayama, and Minoru Todoki. Measurement of thermal conductivity of silicon dioxide thin films using a 3 omega method. *Journal of Applied Physics*, 91(12):9772–9776, 2002.

[67] Edward D. Palik., editor. *Handbook of optical constants of solids III.* Academic Press, San Diego, CA, 1998.

[68] L. I. Maissel and R. Glang, editors. *Handbook of Thin Film Technology.* McGraw-Hill, Inc., New York, 1970, Chapter 8.

[69] B. Rethfeld, A. Kaiser, M. Vicanek, and G. Simon. Femtosecond laser-induced heating of electron gas in aluminium. *Applied Physics A: Materials Science & Processing*, 69(7):S109–S112, 1999.

[70] David G. Cahill, Henry E. Fischer, Tom Klitsner, E. T. Swartz, and R. O. Pohl. Thermal conductivity of thin films: Measurements and understanding. *Journal of Vacuum Science & Technology A: Vacuum, Surfaces, and Films*, 7(3):1259–1266, 1989.

[71] Y Nagasaka and A Nagashima. Absolute measurement of the thermal conductivity of electrically conducting liquids by the transient hot-wire method. *Journal of Physics E: Scientific Instruments*, 14(12):1435–1440, 1981.

[72] H. Eichler. Laser-induced grating phenomena. *Optica Acta*, 24:631–642, June 1977.

[73] H. Eichler, G. Salje, and H. Stahl. Thermal diffusion measurements using spatially periodic temperature distributions induced by laser light. *Journal of Applied Physics*, 44(12):5383–5388, 1973.

[74] R. Nicklow, N. Wakabayashi, and H. G. Smith. Lattice dynamics of pyrolytic graphite. *Phys. Rev. B*, 5(12):4951–4962, Jun 1972.

[75] B. Yang, W. L. Liu, J. L. Liu, K. L. Wang, and G. Chen. Measurements of anisotropic thermoelectric properties in superlattices. *Applied Physics Letters*, 81(19):3588–3590, 2002.

[76] G. Chen, Volz S. G., T. Borca-Tasciuc, T. Zeng, D. Song, K.L. Wang, and M.S. Dresselhaus. Phonon engineering in superlattices. In *MRS Fall Meeting*, volume 545, pages 357–368, Boston, Massachusetts, USA, 1998.

[77] S.-M. Lee, David G. Cahill, and Rama Venkatasubramanian. Thermal conductivity of si–ge superlattices. *Applied Physics Letters*, 70(22):2957–2959, 1997.

[78] Theodorian et. al. Borca-Tasciuc. Thermal conductivity of symmetrically strained si/ge superlattices. *Superlattices and Microstructures*, 28(3):199–206, 2000.

[79] W. Z. Wang, B. Q. Zeng, J. Yang, B. Poudel, J. Y. Huang, M. J. Naughton, and Z. F. Ren. Aligned ultralong zno nanobelts and their enhanced field emission. *Advanced Materials*, 18(24):3275–3278, October 2006.

[80] Zhong Lin Wang. Zinc oxide nanostructures: growth, properties and applications. *Journal of Physics: Condensed Matter*, 16(25), 2004.

[81] G. G. Gadzhiev. The thermal and elastic properties of zinc oxide-based ceramics at high temperatures. *High Temperature*, 41(6):778–782, November 2004.

[82] Tayo Olorunyolemi, Amikam Birnboim, Yuval Carmel, Otto Carl Wilson, Isabel Knowlton Lloyd, Stephen Smith, and Rob Campbell. Thermal conductivity of zinc oxide: From green to sintered state. *Journal of the American Ceramic Society*, 85(5):1249–1253, 2002.

[83] J. D. Walecka A. L. Fetter. *Theoretical Mechanics of Particles and Continua.* McGraw-Hill, Inc., New York, 1980.

[84] S. Link and M.A. El-Sayed. Shape and size dependence of radiative, nonradiative and photothermal properties of gold nanocrystals. *International Reviews in Physical Chemistry*, 19(3):409–453, July 2000.

[85] X. Huang, I.H. El-Sayed, W. Qian, and M.A. El-Sayed. Cancer cell imaging and photothermal therapy in the near-infrared region by using gold nanorods. *Journal of the American Chemical Society*, 128(6):2115–2120, 2006.

[86] N.R. Jana, L. Gearheart, and C.J. Murphy. Wet chemical synthesis of high aspect ratio cylindrical gold nanorods. *Journal of Physical Chemistry B*, 105(19):4065–4067, 2001.

[87] C.J. Murphy, T.K. Sau, A.M. Gole, C.J. Orendorff, J. Gao, L. Gou, S.E. Hunyadi, and T. Li. Anisotropic metal nanoparticles: Synthesis, assembly, and optical applications. *Journal of Physical Chemistry B*, 109(29):13857–13870, 2005.

[88] Mohamed A. Bahri, Maryse Hoebeke, Angeliki Grammenos, Lisiane Delanaye, Nicolas Vandewalle, and Alain Seret. Investigation of sds, dtab and ctab micelle microviscosities by electron spin resonance. *Colloids and Surfaces A: Physicochemical and Engineering Aspects*, 290(1-3):206–212, 2006.

[89] A. M. Tedeschi, L. Franco, M. Ruzzi, L. Paduano, C. Corvaja, and G. D'Errico. Micellar aggregation of alkyltrimethylammonium bromide surfactants studied by electron paramagnetic resonance of an anionic nitroxide. *Phys. Chem. Chem. Phys.*, 5:4204–4209, 2003.

[90] Jorge PÈrez-Juste, Isabel Pastoriza-Santos, Luis M. Liz-Marzn, and Paul Mulvaney. Gold nanorods: Synthesis, characterization and applications. *Coordination Chemistry Reviews*, 249(17-18):1870–1901, 2005.

[91] B. Nikoobakht and M.A. El-Sayed. Evidence for bilayer assembly of cationic surfactants on the surface of gold nanorods. *Langmuir*, 17(20):6368–6374, 2001.

[92] Nikhil R. Jana, Latha A. Gearheart, Sherine O. Obare, Christopher J. Johnson, Karen J. Edler, Stephen Mann, and Catherine J. Murphy. Liquid crystalline assemblies of ordered gold nanorods. *Journal of Materials Chemistry*, 12:2909 – 2912, 2002.

[93] S. Park, M. Pelton, M. Liu, P. Guyot-Sionnest, and N.F. Scherer. Ultrafast resonant dynamics of surface plasmons in gold nanorods. *Journal of Physical Chemistry C*, 111(1):116–123, 2007.

[94] Gregory V. Hartland. Measurements of the material properties of metal nanoparticles by time-resolved spectroscopy. *Phys. Chem. Chem. Phys.*, 6:5263 – 5274, 2004.

[95] Stephanie Tristram-Nagle and John F. Nagle. Lipid bilayers: thermodynamics, structure, fluctuations, and interactions. *Chemistry and Physics of Lipids*, 127(1):3–14, 2004.

[96] Anne Feng Xie, Ryo Yamada, Andrew A. Gewirth, and Steve Granick. Materials science of the gel to fluid phase transition in a supported phospholipid bilayer. *Phys. Rev. Lett.*, 89(24):246103, Nov 2002.

[97] S J Johnson, T M Bayerl, D C McDermott, G W Adam, A R Rennie, R K Thomas, and E Sackmann. Structure of an adsorbed dimyristoylphosphatidylcholine bilayer measured with specular reflection of neutrons. *Biophys. J.*, 59(2):289–294, 1991.

[98] H. Masuda, A. Ebata, K. Teramae, and N. Hishinuma. Alteration of thermal conductivity and viscosity of liquid by dispersing ultra-fine particles (dispersion of al2o3, sio2, and tio2 ultrafine particles. 4:227–233, 1990.

[99] J. A. Eastman, S. U. S. Choi, S. Li, W. Yu, and L. J. Thompson. Anomalously increased effective thermal conductivities of ethylene glycol-based nanofluids containing copper nanoparticles. *Applied Physics Letters*, 78(6):718–720, 2001.

[100] Hrishikesh E. Patel, Sarit K. Das, T. Sundararajan, A. Sreekumaran Nair, Beena George, and T. Pradeep. Thermal conductivities of naked and monolayer protected metal nanoparticle based nanofluids: Manifestation of anomalous enhancement and chemical effects. *Applied Physics Letters*, 83(14):2931–2933, 2003.

[101] Shawn A. Putnam, David G. Cahill, Paul V. Braun, Zhenbin Ge, and Robert G. Shimmin. Thermal conductivity of nanoparticle suspensions. *Journal of Applied Physics*, 99(8):084308, 2006.

[102] S. Lee, S.U.S Choi, S. Li, and J.A. Eastman. Measuring thermal conductivity of fluids containing oxide nanoparticles. *J. Heat Trans.*, 121:280–289, 1999.

[103] Sarit Kumar Das, Nandy Putra, Peter Thiesen, and Wilfried Roetzel. Temperature dependence of thermal conductivity enhancement for nanofluids. *Journal of Heat Transfer*, 125(4):567–574, 2003.

[104] Huaqing Xie, Jinchang Wang, Tonggeng Xi, Yan Liu, Fei Ai, and Qingren Wu. Thermal conductivity enhancement of suspensions containing nanosized alumina particles. *Journal of Applied Physics*, 91(7):4568–4572, 2002.

[105] S. U. S. Choi, Z. G. Zhang, W. Yu, F. E. Lockwood, and E. A. Grulke. Anomalous thermal conductivity enhancement in nanotube suspensions. *Applied Physics Letters*, 79(14):2252–2254, 2001.

[106] J. C. Maxwell. *A Treatise on Electricity and Magnetism.* Oxford University Press, Cambridge, UK, 1904.

[107] R. L. Hamilton and O. K. Crosser. Thermal conductivity of heterogeneous two-component systems. *Industrial & Engineering Chemistry Fundamentals*, 1(3):187–191, 1962.

[108] A. Einstein. *Ann. Physik*, 19:289, 1906.

[109] A. Einstein. *Ann. Physik*, 34:591, 1911.

[110] Ravi Prasher, David Song, Jinlin Wang, and Patrick Phelan. Measurements of nanofluid viscosity and its implications for thermal applications. *Applied Physics Letters*, 89(13):133108, 2006.

[111] Sarit K. Das, Nandy Putra, and Wilfried Roetzel. Pool boiling characteristics of nano-fluids. *International Journal of Heat and Mass Transfer*, 46(5):851–862, 2003.

[112] Choi SUS Wang XW, Xu XF. Thermal conductivity of nanoparticle-fluid mixture. *Journal Of Thermophysics And Heat Transfer*, 13(4):474–480, 1999.

[113] Pawel Keblinski, Jeffrey A. Eastman, and David G. Cahill. Nanofluids for thermal transport. *Materials Today*, 8(6):36–44, 2005.

[114] M. Chiesa, A. J. Simonsen, J. Garg, and G. Chen. The importance of suspension stability for the hot-wire measurements of thermal conductivity of colloidal suspensions. In *Paper to be presented at 16th Australasian Fluid Mechanics Conference*, December 2007.

[115] O. W. Käding, H. Skurk, A. A. Maznev, and E. Matthias. Transient thermal gratings at surfaces for thermal characterization of bulk materials and thin films. *Applied Physics A: Materials Science & Processing*, 61(3):253–261, 1995.

[116] Keith A. Nelson and M. D. Fayer. Laser induced phonons: A probe of intermolecular interactions in molecular solids. *The Journal of Chemical Physics*, 72(9):5202–5218, 1980.

[117] RE Challis, JS Tebbutt, and AK Holmes. Equivalence between three scattering formulations for ultrasonic wave propagation in particulate mixtures. *Journal of Physics D, Applied Physics(UK)*, 31(24):3481–3497, 1998.

[118] Scott Silence. *Time-resolved light scattering studies of structural rearrangements in disordered condensed phase systems.* PhD thesis, Massachusetts Institute of Technology, 1991.

[119] M. J. Assael, E. Charitidou, C. A. Nieto de Castro, and W. A. Wakeham. The thermal conductivity of n-hexane, n-heptane, and n-decane by the transient hot-wire method. *International Journal of Thermophysics*, 8(6):663–670, December 2004.

[120] A. J. Ghajar, W.C. Tang, and J. E. Beam. Comparison of hydraulic and thermal performance of pao and coolanol 25r liquid coolants. In *6th AIAA Joint Thermophysics and Heat Transfer Conference*, Colorado Springs, CO, June 1994.

[121] Chevron Phillips Chemical Company LP. Synfluid pao 4 cst (data sheet), Febrauary 2008.

[122] R. Prasher, P.E. Phelan, and P. Bhattacharya. Effect of aggregation kinetics on the thermal conductivity of nanoscale colloidal solutions (nanofluid). *Nano Letters*, 6(7):1529–1534, 2006.

[123] A H Harker and J A G Temple. Velocity and attenuation of ultrasound in suspensions of particles in fluids. *Journal of Physics D: Applied Physics*, 21(11):1576–1588, 1988.

[124] RE Challis, MJW Povey, ML Mather, and AK Holmes. Ultrasound techniques for characterizing colloidal dispersions. *Reports on Progress in Physics*, 68(7):1541–1637, 2005.

[125] Yongwu Yang and Keith A. Nelson. Impulsive stimulated light scattering from glass-forming liquids. i. generalized hydrodynamics approach. *The Journal of Chemical Physics*, 103(18):7722–7731, 1995.

[126] Mark G. Sceats and Judith M. Dawes. On the viscoelastic properties of n-alkane liquids. *The Journal of Chemical Physics*, 83(3):1298–1304, 1985.

[127] R.G. Yang, X.Y. Chen, A. Schmidt, and G. Chen. Pump-probe experimental study of phonon reflectivity at an interface and phonon relaxation time (nano2005-87064). In *ASME 4th Integrated Nanosystems - Design, Synthesis, and Applications*, UC-Berkeley, September 14–15 2005.

[128] Alan V. Oppenheim and Alan S. Willsky with S. Hamid. *Signals and Systems.* Prentice Hall, 2nd edition, 1996, p. 329.